Titre: Title:	Surface Plasmon Resonance Sensor Interogation with Cladding Modes Excited by Tilted Fiber Bragg Grating
Auteur: Author:	Mohamad Diaa Baiad
Date:	2014
Type:	Mémoire ou thèse / Dissertation or Thesis
Référence: Citation:	Baiad, M. D. (2014). Surface Plasmon Resonance Sensor Interogation with Cladding Modes Excited by Tilted Fiber Bragg Grating [Thèse de doctorat, École Polytechnique de Montréal]. PolyPublie. https://publications.polymtl.ca/1590/

UNIVERSITÉ DE MONTRÉAL

SURFACE PLASMON RESONANCE SENSOR INTERROGATION WITH CLADDING MODES EXCITED BY TILTED FIBER BRAGG GRATING

MOHAMAD DIAA BAIAD

DÉPARTEMENT DE GÉNIE ÉLECTRIQUE

ÉCOLE POLYTECHNIQUE DE MONTRÉAL

THÈSE PRÉSENTÉE EN VUE DE L'OBTENTION

DU DIPLÔME DE PHILOSOPHIAE DOCTOR

(GÉNIE ÉLECTRIQUE)

DÉCEMBRE 2014

UNIVERSITÉ DE MONTRÉAL

ÉCOLE POLYTECHNIQUE DE MONTRÉAL

Cette thèse intitulée :

SURFACE PLASMON RESONANCE SENSOR INTERROGATION WITH CLADDING MODES EXCITED BY TILTED FIBER BRAGG GRATING

présentée par : BAIAD Mohamad Diaa

en vue de l'obtention du diplôme de : Philosophiae Doctor

a été dûment acceptée par le jury d'examen constitué de :

M. LESAGE Frédéric, Ph. D., président

M. KASHYAP Raman, Ph. D., membre et directeur de recherche

M. LAURIN Jean-Jacques, Ph. D., membre

M. VO-VAN Truong, Ph. D., membre

DEDICATION

dedicated to my family,

for all of the love, support, and encouragement

in memory of

my grandfather Jamal Habes

ACKNOWLEDGEMENTS

I would like to use these few lines to express my gratitude to my supervisor, colleagues and friends who supported me on this thesis.

First of all I'd like to thank my supervisor and research director Prof. Raman Kashyap who warmly welcomed me in his research team. He was really what I would call a great supervisor. Giving his time to define and refine my project, sharing his ideas and listening to mine. Prof. Kashyap has always believed in my potential, supported me throughout this project from the beginning, which was really touching.

I would like to especially acknowledge Prof. Caroline Boudoux who I have worked and collaborated with. She has been a constant support during the later years of my PhD. Special thanks for the invaluable help.

Furthermore, I would like to express my upmost appreciation to the following colleagues for their help and support: Mathieu Gagné, Victor Lambin Iezzi, Jérôme Lapointe, Ameneh Bostani, Elton Soares de Lima Filho, and Sébastien Loranger. When I started, it was a hard job to get to know so many new colleagues, now it will be quite hard to think about leaving such kind people. Also in particular thanks to my colleague and friend Mamoun Wahbeh for supporting me during my PhD and my personal life. I will never forget how much he did for me!

RÉSUMÉ

Le but de ce projet est de developer de nouvelles configurations de capteurs à résonance de plasmons de surface basés sur les réseaux de Bragg. Il se concentre sur l'étude de quatre configurations novatrices de capteurs à résonances de plasmons et de leur application en mesure d'indice de réfraction environnant.

Premièrement, une nouvelle approche de mesure d'indice de réfraction utilisant un coupleur à double gaine et un réseau de Bragg pour capturer les modes de gaine en réflexion est démontrée. Le spectre optique ainsi que la puissance des modes de gaines sont obtenus à travers l'utilisation d'un coupleur à fibre à double gaine conçu sur mesure et connecté à un réseau de Bragg à haute réflectivité écrit dans une fibre photosensible standard légèrement inclinée et gravée de façon à la coupler au diamètre intérieur de la fibre à double gaine. Ce dispositif est capable de capturer les modes de gaines autant d'ordres inférieurs que supérieurs en réflexion de manière simple et efficace. Il devient alors possible de déterminer l'indice de réfraction environnant avec une extrême sensibilité à partir d'une perte de puissance mesurée de ≈ 91% de la puissance initiale permettant d'obtenir une résolution de 1.4333×10^{-5} unités d'indice de réfraction (UIR) entre 1.37 et 1.45. Le dispositif permet donc une large bande d'opération entre 1.30 et 1.45 UIR qui offre la possibilité de discriminer chacun des modes de gaine capturés. L'approche proposée peut être adaptée à plusieurs autres types de capteurs de courbure, température, indice de réfraction et d'onde évanescente.

Deuxièmement, une nouvelle approche de capteur à résonance de plasmons de surface à fibre utilisant la configuration de coupleur à double gaine décrite précédemment ainsi qu'un réseau de Bragg incliné et recouvert d'or est démontrée. Cette nouvelle approche d'interrogation basée sur le spectre de réflexion offre une amélioration de la bande d'opération du dispositif en comparaison aux techniques préexistantes. Le dispositif permet la détection de résonances de plasmons de surfaces dans le spectre de réflexion et de transmission, permettant aisément une comparaison avec les techniques standards préexistantes qui utilisent le spectre de transmission. Le capteur possède aussi une large bande d'opération allant de 1.335 à 1.432 UIR et une sensibilité de 510.5 nm/UIR. Le capteur démontre une forte dépendance à l'état de polarisation du mode de cœur qui peut être utilisé pour activer ou désactiver la résonance plasmonique.

La troisième approche est un capteur à plusieurs canaux en série excités à l'aide de réseaux de Bragg inclinés inscrits dans une fibre avec une déposition d'or et de chrome. Les canaux sont inscrits dans une seule fibre optique et chacun possède une bande de longueur d'onde d'opération différente, une inclinaison du réseau de Bragg différente, et donc un intervalle d'indice de réfraction qui lui est propre. Ce système, agissant comme un multiplexeur dans un une seule fibre optique ayant un certain nombre de réseaux de Bragg inclinés, est démontré pour la première fois. La polarisation de chaque canal, qui est basé sur l'orientation de l'inclinaison de chaque réseau de Bragg incliné, peut être utilisé pour activer ou désactiver chaque capteur plasmonique. Cette approche offre une bande d'opération de 1.40 à 1.44 UIR et une sensibilité d'environ 500 nm/UIR.

La quatrième approche fait appel à la déposition d'une couche de silicium et est aussi une configuration à multiples canaux étant chacun associés à un type de fibre différent. L'utilisation couche diélectrique à indice de réfraction élevée de silicium est démontrée et caractérisée pour la première fois pour un tel dispositif. Chaque canal démontre un intervalle d'opération unique. La couche de silicium est utilisée pour ajuster la bande d'opération d'indice de réfraction à une valeur plus basse. Ce système permet une opération allant de 1.30 à 1.435 UIR, ce qui est le plus large intervalle démontré à ce jour pour un tel dispositif. L'ajout d'une couche de silicium améliore la sensibilité du capteur à ~700 nm/UIR and démontre une plus forte dépendance en polarisation. La flexibilité et la facilité d'utilisation de l'approche proposée peut être adaptée à plusieurs configurations de capteurs plasmoniques.

Les réseaux de Bragg proposés au cours de ce projet ont été écrits à l'aide de différentes techniques. Une nouvelle source laser pulsée de 224 nm offrant une puissance maximale de 280 mW a été utilisée pour la fabrication de réseaux de Bragg conjointement à l'utilisation d'un montage de balayage de masque de phase. Les réseaux de Bragg inclinées ont été obtenus à l'aide d'une source laser pulsée analogue de 213 nm utilisée dans un second montage de balayage de masque de phase. Le laser de 213 nm produit des impulsions de 7 ns avec une énergie de 10 μJ à un taux de repetitions allant de 0.1 à 30 kHz et avec une puissance moyenne maximale de 130 mW. En utilisant un interféromètre, la longueur d'onde de Bragg peut être choisie indépendamment de la longueur d'onde du laser UV en changeant l'angle des miroirs de l'interféromètre. Pour fabriquer des réseaux de Bragg inclinés, la monture de la fibre optique est tournée relativement à l'axe d'orientation de la fibre.

Les configurations proposées visent à améliorer les performances des capteurs à résonance de plasmons de surface des points de vue de la miniaturisation, de la sensibilité et du multiplexage, des ajouts significatifs à la technologie actuelle des capteurs plasmoniques utilisant des réseaux de Bragg inclinés.

ABSTRACT

The objective of this Thesis is to develop novel schemes in surface Plasmon resonance (SPR) sensing with Bragg gratings. The thesis focuses on research studies on the sensing characteristics of four novel configurations of SPR and surrounding refractive indices (SRI) sensors.

Firstly, a novel SRI measurement scheme has been demonstrated using a double-clad fiber coupler (DCFC) and a fiber Bragg grating (FBG) to capture cladding modes in reflection. The optical spectra and power in the cladding modes are obtained through the use of a specially designed DCFC spliced to a highly reflective FBG written into slightly cladding-etched standard photosensitive single mode fiber to match the diameter to the inner cladding of the DCFC. The device is capable of capturing low and high order backward propagating cladding modes simply and efficiently. The device is capable of measuring the SRI with an extremely high sensitivity with a total power drop by ≈ 91% of its initial value and a resolution of 1.433×10^{-5} RIU between 1.37 and 1.45 RIU. The device provides a large SRI operating range from 1.30 to 1.45 RIU with sufficient discrimination for all individual captured cladding modes. The proposed scheme can be adapted to many different types of bend, temperature, refractive index and other evanescent wave based sensors.

Secondly, a novel optical fiber SPR sensor scheme is demonstrated using reflected guided cladding modes captured by the above mentioned DCFC, and excited in a gold-coated fiber with a tilted Bragg grating (TFBG). This new interrogation approach which is based on the reflection spectrum provides an improvement in the operating range of the device over previous techniques. The device allows detection of SPR in the reflected spectrum and also in the transmitted spectrum as well, making it far easier in comparison with previous standard techniques which use the transmission spectrum. The sensor has a large operating range from 1.335 to 1.432 RIU, and a sensitivity of 510.5 nm/RIU. The device shows strong dependence on the polarization state of the guided core mode which can be used to turn the SPR on or off.

The third scheme is an in-line, multichannel SPR sensor scheme excited with a TFBG inside a chromium and gold-coated fiber. The channels are imprinted in one single optical fiber and each has a different operating wavelength, different TFBG tilt angle, and hence different refractive index operating range. This system, as a multiplexer in a single optical fiber for a number of TFBG-SPR sensors, is demonstrated for the first time. The polarization state of each channel

based on the TFBG orientation can be used to switch each SPR sensor on or off as required. This scheme provides an operating range from 1.40 to 1.44 RIU, and a sensitivity of around 500 nm/RIU.

The fourth scheme is a silicon-coated multi-channel SPR sensor scheme excited with a TFBG where different types of fibers have been used and each represents a single separate channel. The high-index dielectric layer silicon coating is demonstrated and characterized for the first time in such am SPR-TFBG sensor. Each channel shows a unique refractive index operating range. The silicon layer is used to tune the SPR refractive index operating range to lower values. This system provides a refractive index operating range from 1.30 to 1.435 RIU, which to our knowledge, is the largest reported so far of such SPR-TFBG sensors. Adding the silicon layer improves the sensor sensitivity to ~700 nm/RIU and shows stronger polarization dependence. The flexibility and the improved ease of use of the proposed scheme can be adapted to many SPR-TFBG based sensors applications.

The FBGs and the TFBGs proposed in this project have been written by different techniques. A new high-repetition rate 224 nm laser source was used for the FBG fabrication using a scanning phase mask technique with a maximum average writing power of 280 mW at 224 nm. The TFBGs were written using a commercially available 213 nm Q-switched nanosecond Nd:VO_4 laser and a newly developed scanned phase-mask-based Talbot interferometer. The 213 nm laser produces pulses of 7 ns with an energy of 10 μJ at a repetition frequency between 0.1 and 30 kHz with a maximum average power of 130 mW. By using the interferometer, the Bragg wavelength can be chosen independently of the UV laser wavelength by changing the mutual angle between the mirrors of the interferometer and the fiber plane. To fabricate tilted gratings with interferometer, the fiber holder is rotated relative to the propagation axis of the fiber.

The proposed configurations aim to improve the performance of SPR biosensors towards miniaturization, better discrimination, increased sensitivity, and multi-analyte sensing which can add significant improvement to existing surface Plasmon resonance sensors using tilted fiber Bragg gratings.

TABLE OF CONTENTS

List of figures

LIST OF SYMBOLS AND NOTATIONS

UV	Ultra-violet
SPR	Surface Plasmon resonance
SPW	Surface Plasmon wave
SPP	Surface Plasmon polariton
LRSPR	Long range surface Plasmon resonance
SRSPR	Short range surface Plasmon resonance
LP	Linearly polarized
FBG	Fiber Bragg grating
TFBG	Tilted fiber Bragg grating
LPG	Long period grating
SMF	Single mode fiber
SMF-28	Single mode fiber (full name Corning® SMF 28™)
MMF	Multi-mode fiber
FWHM	Full-Width Half Maximum
CW	Continuous Wave
HF	Hydrofluoric acid
OSA	Optical Spectrum Analyzer
PC	Polarization Controller
DCFC	Double-clad fiber coupler
DCF	Double-clad fiber
SNR	Signal-to-Noise Ratio
NA	Numerical aperture
RIU	Refractive Index Unit
SNR	Signal to noise ratio
TE	Transverse electric
TM	Transverse magnetic
TIR	Total internal reflection
PM	Phase matching

YLF	Yttrium lithium fluoride
BBC	Broadband source
SWS	Swept wavelength system
OSA	Optical spectrum analyzer
SOP	State of polarization

LIST OF APPENDICES

CHAPTER 1 INTRODUCTION

1.1 Overview of the dissertation

This dissertation is organized as follows:

Chapter 1 reviews the literature in the field and discusses what has already been demonstrated so far. It shows the limitations of other technologies leading up to what exactly this dissertation is trying to solve. Also, chapter 1 introduces the basics and theory of surface Plasmon resonance (SPR) relevant to the project. In the end of chapter 1, the objectives of the project have been introduced. Chapter 2 presents an introduction to the theory of Bragg gratings. Equations and various techniques of fabrication relevant to the proposed project are presented, described and compared. The theory and the fabrication techniques of TFBGs are highlighted. Furthermore, the process of coating the TFBGs is introduced. Chapter 3 presents the first article presented during the PhD project. The article is on capturing the cladding modes in reflection by using the DCFC. The cladding modes are excited in this project by strong FBG written in a photosensitive fiber. The scheme has been used as refractometer to measure the SRI leading up to the TFBG-SPR sensor presented in chapter 4. Chapter 4 presents the second article based on interrogating the SPR in reflection by capturing the cladding modes by DCFC with TFBG. Chapter 5 introduce an article of distributed SPR sensors by concatenation of multi in-line sensors in a single optical fiber by TFBGs. Chapter 6 presents the fourth article of the dissertation demonstrating the improvement of sensitivity and polarization dependency of silicon and gold coated multi-channel SPR sensors using TFBGs. In Chapter 7, a general discussion on the proposed schemes and their impact on the field of SPR-TFBG sensors is presented. Also, their limitations and the recommendations to overcome them has been discussed. In Chapter 8, the work is concluded and the directions for future work is proposed.

1.2 Literature review

Surface Plasmon are surface electromagnetic excitation waves supported at a metal-dielectric interface having their electric field maxima at the metal-dielectric boundary, decaying exponentially on either side with a small penetration depth. Surface Plasmon resonance (SPR) based biosensors are label-free bio-sensors which have significant importance in applications

such as medical diagnosis and environmental assessment. They are increasingly popular in biological applications for the measurements of bio-molecular interactions in real-time [1]–[3]. When Wood in 1902 illuminated a metallic diffraction grating with polychromatic light, he observed the surface Plasmons for the first time [2], [4]. He noticed dark bands in the spectrum which he referred to anomalies. Optical excitation of surface Plasmons by attenuated total reflection method was demonstrated by Kretchman [5] and Otto [4] in the late sixties. A variety of configurations and devices have been proposed to exploit surface Plasmon on metal dielectric interfaces for bio-sensing applications [1], [2], [6]–[13]. The most common way to excite them used the prism coupling technique to create total internal reflection (TIR) at the prism-metal interface and by evanescent field coupling, the light incident on the prism at resonant angle transfers its power to the SPR, by evanescent field coupling [14], [15]. The resonance coupling can be seen as a dip in the light spectrum reflectivity, which can be tracked by wavelength interrogation and measuring the wavelength, angle interrogation or the intensity interrogation of the reflected light. The change in the conditions of the resonance coupling will result in resonant shift as can be seen in Fig. 1.

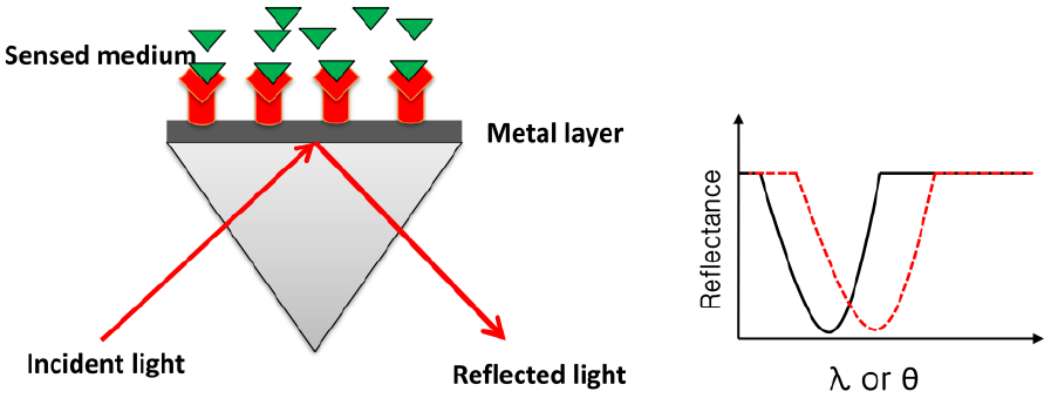

Fig. 1. (a) prism-coupling configuration and (b) resonance dip and its shift in the reflected light spectrum.

The prism structure has moving parts, makes the device cumbersome, not convenient to miniaturization and integration, and cannot be used in in-line fiber applications. The coupling prism can be conveniently replaced by the an optical waveguides which provides attractive features over the prism coupling configuration such as a simpler way to control the optical path and a smaller size [4], [6]. Also, optical fibers have been used widely in SPR bio-sensors. Optical

fibers configurations have more advantages over other configurations such as capability of remote sensing, flexible design, and the highest level of miniaturization of SPR devices [16] [13]. Single mode fiber with polished and metal-coated tip has been used in early fiber-SPR biosensors as can be seen in Fig. 2. where the changes in the SPR are measured by analysing the back reflected light from the fiber or the diffracted light from its end [17]. Taking into account the practical applications and difficulties associated with depositing a very thin, and uniform metal layer on cylindrical surfaces, SPR sensors based on side-polished single-mode optical fibers have been investigated [6], [8], [12].

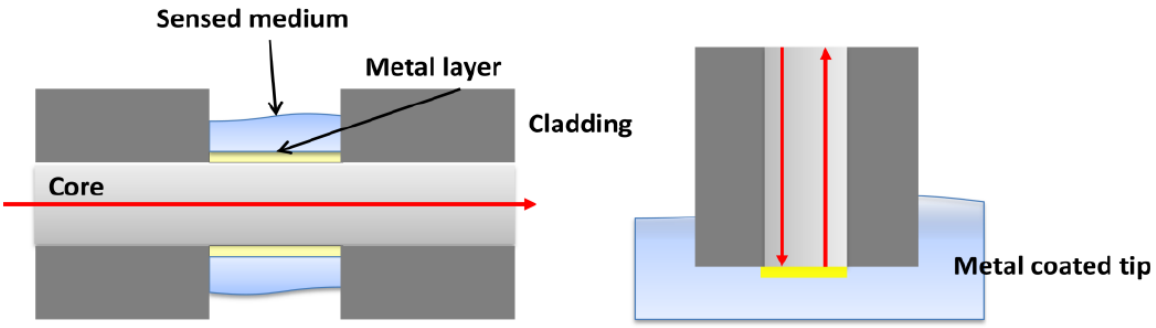

Fig. 2. Fiber-SPR with polished and metal-coated tip.

Homola proposed a SPR sensor using side-polished single mode optical fiber [2], [18] as can be seen in Fig. 3. where the cladding of the fiber has been removed and it has been coated with a metal layer surrounded by the sensed medium based on spectral interrogation. By satisfying the phase matching condition between the core mode and the SPW mode, the guided core mode excites SPW at the interface between the metal and a sensing medium. The effective refractive index and the propagation constant of the SPW depends on the ambient refractive index (ARI) of the sensed medium and hence the strength of the interaction between the SPW and the fiber mode, and consequently fiber mode damping is based on the refractive index of the sensed medium. So changes in the transmitted optical power at a fixed wavelength can be used as an intensity interrogation method to measure variations in the ARI or by measuring changes in the wavelength at which the resonant damping of the fiber mode occur as a wavelength interrogation method [18]. It has to be pointed out that the process of exciting SPW is highly polarization-sensitive since only p-polarized (TM) wave with film may excite SPW.

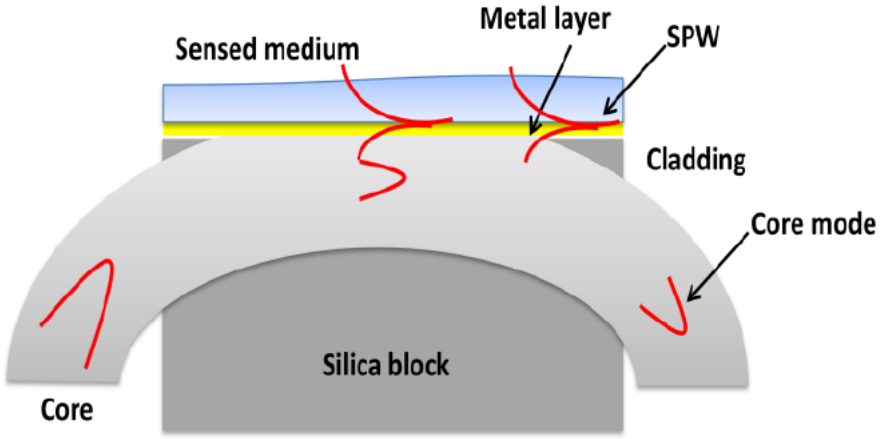

Fig. 3. Side – polished optical fiber SPR sensor.

SPR sensors based on side-polished optical fibers have small sensing area and suffer from sensitivity to fiber deformations and bending and hence from its interaction with SPW. Also, the quartz block used to support the side-polished fiber makes the sensor bulky.

It was demonstrated that the sensitivity of SPR sensor is improved up to one order of magnitude using a high-index prism SPR sensor scheme coated with silver and a top layer of 10-15 nm silicon [19], [20]. Bhatia and Gupta demonstrated a SPR optical fiber sensor using a multi-mode fiber of 600 μm core diameter coated with metal and a thin 10 nm layer of silicon as can be seen in Fig. 4 [21]. The sensor operated within a wavelength range between 600 and 900 nm and was demonstrated for a SRI between 1.333 to 1.353 RIU (Refractive Index Unite). The silicon layer improves the sensitivity of such a sensor and tunes the resonance wavelength [21]. However, repeatability seems to be big issue with this sensor since it is necessary to excite the modes stably in the MMF.

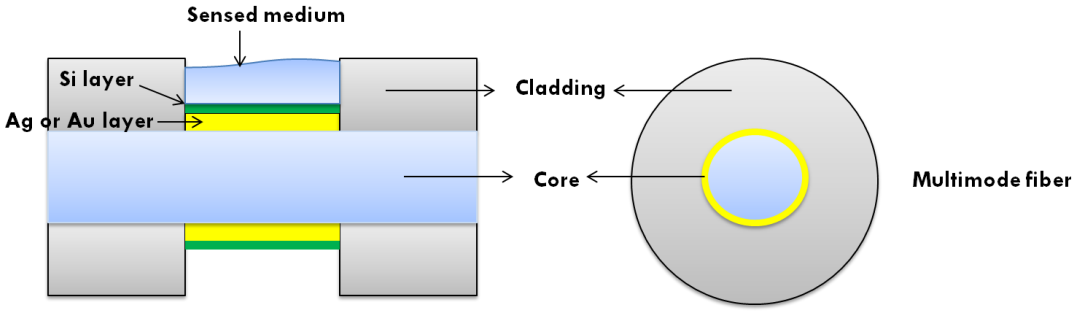

Fig. 4. Silicon-coated metalized Multi-mode optical fiber without using Bragg gratings [21].

Recently, SPR have been excited using gratings in metal coated waveguides and fibers and several schemes have been proposed to use them for bio-chemical sensing applications. Optical gratings are axial periodic refractive index variation created within the core region of the waveguide and have the potential to couple power from the core mode to a co-propagating or a counter-propagating mode, provided a satisfied phase matching condition which is in turn depends on the propagation constants of involved modes and the grating period. The guided mode power shows a minimum transmitted power at the resonance wavelength, at which the phase matching is satisfied [22].

The fiber gratings are classified into different categories, short period gratings, also known as the fiber Bragg gratings (FBG), and long period gratings (LPG) depending on the period of the grating and the refractive index variation. Fiber Bragg gratings couples a forward propagating core mode to a backward propagating core mode.

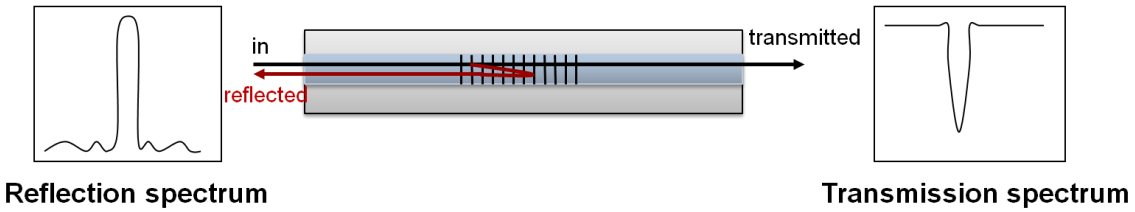

Fig. 5. Reflection and Transmission spectra using Bragg grating in optical fiber

Tilting the FBG leads up to the tilted fiber Bragg grating (TFBG) which couple the forward Bragg core mode to the backward propagating cladding modes which can be observed as a series of resonance dips on the short wavelength side of the transmission spectrum as can be seen in Fig. 6 [22]. These modes can be excited efficiently with different tilt angles relative to the propagation axis of the fiber [22]. By simply increasing the tilt angle, stronger coupling occurs to cladding modes of relatively lower effective indices and vice versa [22]. FBGs and TFBGs theory will be discussed in more details in chapter 2.

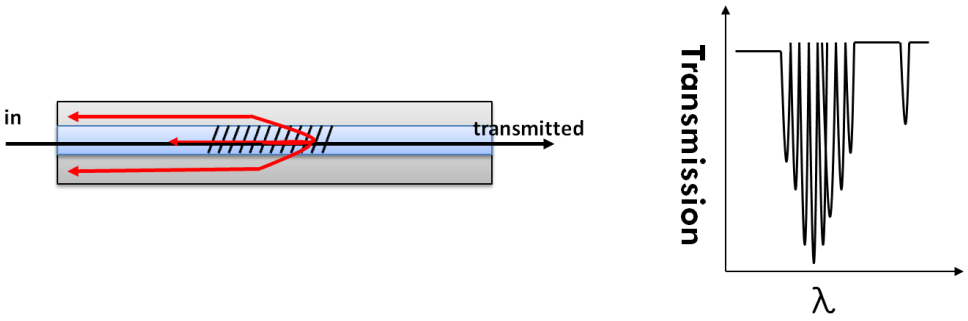

Fig. 6. Tilted fiber Bragg grating (TFBG) and its transmission spectrum in optical fiber.

On the other hand, LPG couples the core mode to a forward propagating cladding mode [22].

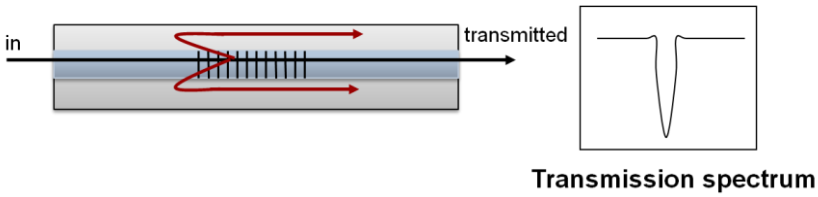

Fig. 7. Transmission spectrum using LPG in optical waveguide

Ctyroky et al. [23] proposed a theoretical model to use of the reflected or transmitted guided mode by a waveguide Bragg gratings (WBG) to detect the change in the sensed medium refractive index as can be seen in Fig. 8. [23]. This configuration gives sharp SPR compared to broad dip in the case of standard SPR sensors. The sensitivity of this SPR-WBG sensor is 50 nm/RIU and a resolution of 2×10^{-5} RIU can be reached by such a sensor [23].

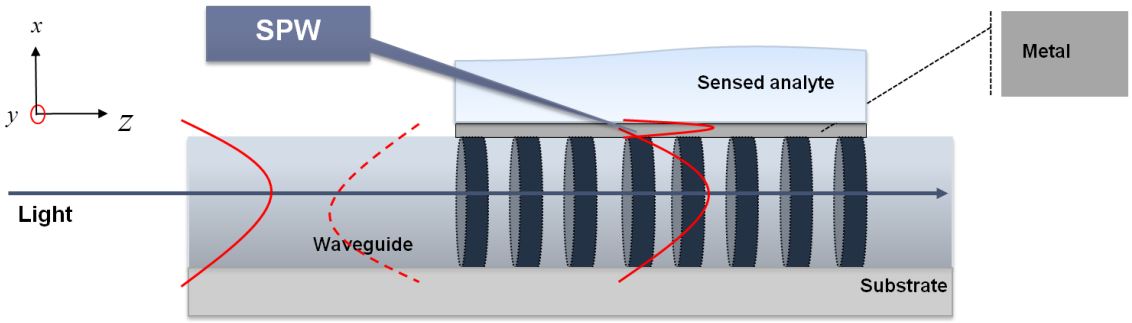

Fig. 8. SPR-WBG sensor proposed by Ctyroky

Including the use of optical waveguides and optical fibers schemes, these schemes have used a surface Plasmon wave (SPW) as a sensing tool. This wave is not the pure surface Plasmon polariton (SPP) and it has a hybrid nature consisting of the guided core mode coupled to the SPP and thus it is weakly sensitive to changes in the effective refractive index of the SPP. Spackova

and Homola have proposed theoretically a multi-channel single-mode fiber optic SPR sensor based on coupling between the forward propagating core mode to the back-propagating mixed SPP-cladding modes by FBG [24]. Such a sensor gives a maximum Fig. of merit of $\chi = 800\,RIU^{-1}$, sensitivity of 200 nm/RIU and FWHM (Full Width Half Maximum) of 0.25 nm [8].

Pure SPP has almost all its field concentrated at the metal-dielectric interfaces and hence, it is highly sensitive to changes in the sensed medium refractive index [25]–[30]. Nemova and Kashyap [26] who were the first to have proposed exciting a pure SPP, suggested the use of a fiber Bragg grating to couple the guided mode to the SPP. The core and cladding radii are 13 μm and 14 μm respectively and the fiber has a coating of 10 - 20 nm gold layer [26]. In order to achieve a strong modal coupling between the core mode and the pure SPP by their configuration, they considered a specially designed optical fiber having very thin cladding which has a thickness of about 1 μm. A theoretical model of an integrated planar SPP refractive index sensor exited by Bragg gratings has investigated in [28]. This model has a sensitivity of 250 nm/RIU and the bandwidth of the transmission spectrum is 500 pm. Nemova and Kashyap also suggested a configuration based on corrugated metal grating by writing the grating in the metal region itself [31]. It has been reported that even for a very thick cladding region of about 4.5μm, the grating length ranges typically between 4-6 cm with a sensitivity of 276 nm/RIU. Also, a pure SPP excitation by a corrugated metal LPG written in a metal coated planar integrated optical waveguide has been theoretically presented by Nemova and Kashyap [27]. Such a sensor exhibits of 1100 nm/RIU. A comparative study of metal coated side polished optical fiber Bragg gratings and LPG has been investigated theoretically [30]. The sensing characteristics of the FBG and the LPG have been analyzed and the structure of this sensor has been optimized with respect to maximum sensitivity. The proposed device gives a maximum sensitivity of 234 nm/RIU with FBG structure and 1288 nm/RIU with LPG structure. The sensing area of such a sensor is small and limited by the side-polished fiber block.

The cladding modes can be used for SPR sensing as has been demonstrated by Shevchenko and Albert [32]. Cladding modes are guided modes which can be excited easily by scattering light from the core of an optical fiber into the cladding [33]. FBG excited cladding modes are traditionally observed as a series of resonance peaks on the short wavelength side of the transmission spectrum of an FBG [22], [34], due to the limited overlap of the field of the

cladding modes with the guided mode field and the refractive index change across the core. These modes can also be excited with high efficiency as seen in the spectrum of a tilted fiber Bragg grating (TFBG) [22]. The cladding modes excited by the TFBG incident on the cladding metal interface transfer their power to the SPR at a resonant wavelength, by evanescent field coupling [15].

These are generally not observed in the reflection spectrum since they may be dissipated through propagation along the high-index polymer jacket of the fiber [33]. Recently, many schemes have been proposed to re-couple the reflected cladding modes back into the core. For example, a sensor has been proposed to re-couple cladding modes into the core of a short fiber excited by tilted fiber Bragg grating (TFBG) in which the sensor fiber was spliced to misaligned fiber [35], [36]. The sensor was used to measure the ambient refractive index, as a bend and vibration sensor [35], [36]. Such SRI sensor provides a dynamic range from 1.33 to 1.45 with sensitivity of 1100 nW/RIU at 1.33 RIU. The re-coupled cladding modes are within the wavelength band of 1538 nm and 1551 nm as merged band with no discrimination between individual cladding modes [36]. Another scheme to re-couple low order cladding modes excited by the TFBG in the core used an abrupt bi-conical fused taper [37].

Cladding modes have also been re-coupled into the core with a TFBG in which a short multimode fiber or a thin-core fiber section with a mismatched core diameter section was spliced between a single mode fiber and the TFBG [38]. The recoupled cladding modes in the best-case scenario are within the wavelength band of 1541 nm and 1549 nm. The sensor was used to measure the different refractive indices of glycerine-water solutions surrounding the TFBG providing a dynamic range from 1.33 to 1.45 RIU.

A scheme to couple the cladding modes into the core using a hybrid long period grating (LPG) and an FBG device has also been demonstrated. Here, the forward propagating core mode is partially coupled by the LPG into a cladding mode, which in turn is reflected with the core mode by a subsequent FBG, and partially re-coupled into the core by the same LPG [39], [40].

One of the problems in all these devices is that, generally when a large number of cladding modes are involved, it is difficult to capture all the modes within a large wavelength band. An efficient discrimination between individual cladding modes is another problem to consider.

Recently, many surface Plasmon resonance (SPR) sensors have been proposed using the excitation of an SPR by tilted fiber Bragg gratings in gold-coated waveguides and fibers [41]. A

variety of schemes and devices have been proposed to exploit surface Plasmon resonance (SPR) on metal dielectric interfaces using TFBG. Shevchenko and Albert have experimentally observed the existence of SPR modifying the cladding modes by using fiber tilted Bragg gratings (TBG) at a small angle (2°–10°) as can be seen in Fig. 9 [32]. The sensitivity of such a sensor is 456 nm/RIU for RI operating range between 1.42 and 1.45 RIU. The spectral width of the SPR that is perturbing some of the cladding modes is 5nm [32].

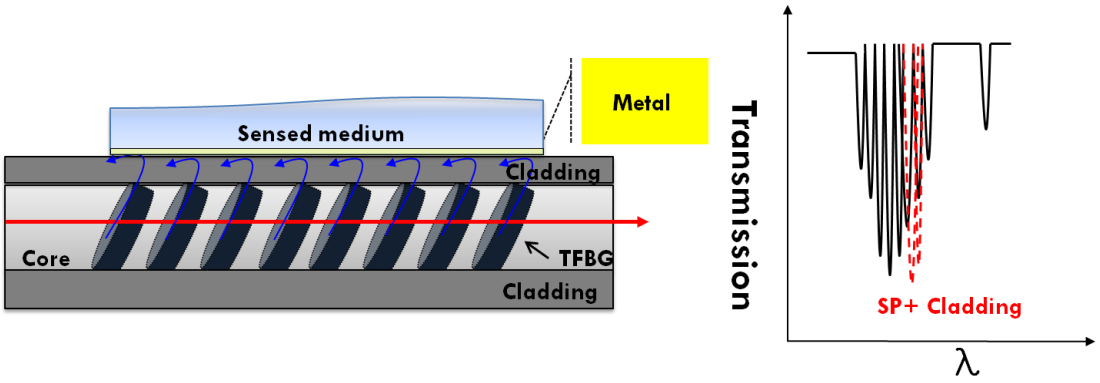

Fig. 9. SPR-cladding modes coupling using tilted fiber Bragg gratings (TFBG).

Holmes had proposed the first demonstration of an experimental planar-integrated SPR-TBG sensor [42] which operates by coupling the core waveguide mode to a set of hybrid Plasmon-dielectric modes. The proposed device gives a maximum sensitivity of 566.9 nm/RIU by tracking the largest negative gradient of the cladding envelope where for some refractive index range, the Plasmon mode does affect and modify the form of the cladding mode envelope.

Different schemes have been proposed to track individual cladding mode resonances and their dependence on the state of polarization (SOP) to improve the resolution and the performance of the SPR-TFBG sensor [43]–[45]. The first Stokes parameter and the polarization dependent loss (PDL) have been used experimentally to interrogate the SPR-TFBG. Caucheteur proposed an experimental TFBG-SPR on a gold-coated SMF sensor using different properties such as the polarization dependent loss and the first Stokes parameter [46]. Such a sensor provides a sensitivity of 673 nm/RIU, again for a limited SRI range between 1.31 and 1.38 RIU with a FWHM of the SPR envelope of 5 nm.

Chen and Caucheteur experimentally demonstrated a TFBG-SPR scheme on a single mode fiber (SMF) coated with 2.6 μm low-index polymer of Cytop and 50 nm of gold [47]. The sensor

showed both, long range SPR (LRSPR) and short range SPR (SRSPR) coupled modes over the wavelength range from 1525 to 1610 nm. Their scheme achieved an experimental sensitivity of 115 nm/RIU attributed to the LRSPR coupling and 68 nm/RIU to the SRSPR when the SRI was 1.3335. The sensitivity varied based on the SRI to reach a maximum of 186 nm/RIU between 1.31 and 1.35 RIU [47]. Also, a TFBG-SMF has been coated with silver nanowires of 1-3 μm in length and 40-50 nm in diameter [48]. The PDL spectrum of the tilted fiber Bragg grating used to excite the cladding modes has been studied and shown to provide a sensitivity of 650 nm/RIU for a SRI range 1.330 to 1.347 RIU [48]. Chan and Albert demonstrated the transmission spectrum of TFBG reflected from a cleaved fiber end-facet coated with gold for sensing [49] where the measured spectrum represents the interference between the reflection spectrum and the transmion spectrum seen reflected from the fiber end.

One of the characteristics of all these devices using the TFBG-SPR sensors is that the cladding modes are not collected since they may be dissipated through propagation along the high-index polymer jacket of the fiber. Hence, the SPR is usually observed through the transmission spectrum alone. Also, the transmission spectrum has weak cladding resonances for the low-order cladding modes which limits the operating range of the device. Additionally, sensors operating in transmission require that the grating itself be coated in gold.

A multi-channel single-mode fiber (SMF) SPR sensor scheme using fiber Bragg gratings (FBG) has been proposed theoretically [24]. Here, the multichannel is achieved by a sequence of FBGs of different periods where the forward propagating core mode is partially coupled to backward travelling cladding modes. The sensor provided a calculated sensitivity of 200 nm/RIU between 1.32 and 1.325 RIU [24]. However, this approach requires very strong gratings to be inscribed and should be used with apodized FBGs for a clear SP resonance signature.

Albert *et al.* [50] have demonstrated a TFBG-SPR biochemical sensor in SMF coated with 30-50 nm of gold functionalized with aptamer receptor molecules. The sensor can act as a stand-alone device or as a multi-sensor platform. They proposed a multiplexing scheme based on multi-fiber sensing devices in which each individual fiber represented one channel of the multiplexed system [50]. The multi-fiber TFBG-SPR sensing devices in SMF coated with 30-50 nm of gold attached [50]. The device provides a sensitivity of 500 nm/RIU between 1.32 and 1.42 RIU. The concatenation of SPR sensors has not been demonstrated experimentally in the proposed schemes

using TFBGs in a single optical fiber. Such cascaded scheme allows the sensing of different analytes by positioning a number of in-line TFBGs in which the wavelength operating range of each channel can be engineered as required. Also, the effect of incorporating a layer of silicon on the metalized TFBG-SPR sensors has not been demonstrated yet by the proposed schemes where the silicon layer is expected to tune the SRI operating range and to enhance the sensitivity of the TFBG-SPR sensor. These issues have been presented for the first time and their impact in the field has been demonstrated experimentally through this dissertation in chapter 3 to 6.

1.3 Basics of Surface Plasmon Resonance

For SPRs to exist, the real part of the dielectric constant of the metal must be negative and its magnitude must be greater than that of the dielectric region [2]. The coupling of the light to the surface Plasmon wave (SPW) requires a coupling prism, waveguide or a periodic grating surface [2].

SPR sensors can be characterised by important parameters: sensitivity, detection accuracy known as signal to noise ratio (SNR), resolution, operating range, and Figure of merit. Sensitivity of SPR sensor can be characterized by the shift in the monitored parameter, wavelength of our proposed device, to the parameter to be determined, the refractive index of sensed medium of our proposed device,:

$$S = \frac{\Delta \lambda}{\Delta n} \tag{1-1}$$

Resolution of SPR sensor is the smallest change in the parameter to be determined which produces a detectable change in the sensor output. It has to be pointed out that the resolution of the sensor depends on the sensor properties and on the accuracy of the sensor monitoring devices such as the optical spectrum analyzer (OSA) [2], [10], [11]. Another important parameter to characterize SPR sensors related to resolution is the detection accuracy is the signal to noise ratio (SNR). The detection accuracy or the SNR can be characterized by how accurately the parameter to be monitored, wavelength or resonance angle, of the sensor can be detected. Hence the parameter to be determined represented by the refractive index of the sensing layer in our detection scheme [13] where apart from the limitations of a real instruments, the detection accuracy depends on the width of the SPR dip. Therefore, if $\Delta\lambda_{FWHM}$ is the full width half

maximum (FWHM) of the SPR dip corresponding to 0.5 reflectance, the SNR of the SPR sensor with wavelength interrogation can be defined as [13]:

$$SNR = \frac{\Delta\lambda}{\Delta\lambda_{FWHM}} \tag{1-2}$$

It has to be pointed out that the narrower the SPR curve, the higher is the SNR. For better performance of the SPR sensor, sensitivity and SNR have to be as high as possible to give better sensing characteristic. SPR sensor's sensitivity and SNR can be used to introduce other parameter called Figure of merit defined by:

$$\chi = \frac{S}{\Delta\lambda_{FWHM}} \tag{1-3}$$

SPR sensing devices showing a bigger χ are capable of giving higher resolution [14]. An operating range which can be measured by a SPR sensor is the range of values of the parameter to be determined which is the sensed medium's refractive index for our proposed device [11].

In the subsequent paragraphs, we will describe the phase matching (PM) condition which has to be satisfied in order to excite the SPR coupling.

The incident wave vector (the propagation constant of the evanescent wave) is given by the following expression [2]:

$$\beta_i = \left(\frac{2\pi}{\lambda}\right) n * sin\theta_i \tag{1-4}$$

where θ_i is the incident light angle, λ is the wavelength of the incident light, $(2\pi/\lambda)$ is the free-space wave number and n is the refractive index of the fiber (silica).

If the metal film is sufficiently thin (less than 100 nm for light in visible and near infrared part of spectrum), the evanescent wave penetrates through the metal film and couples with a surface Plasmon at the outer boundary of the metal film [2]. The wave vector of the Plasmon mode, the propagation constant of the surface Plasmon propagating along a thin metal film, is described by the following expression [2]

$$\beta_{sp} = \left(\frac{2\pi}{\lambda}\right) * \sqrt{\frac{\varepsilon_m * \varepsilon_d}{\varepsilon_d + \varepsilon_m}} \tag{1-5}$$

Where ε_d and ε_m are the dielectric permittivity constants of the metal film and the dielectric exit medium, respectively.

In order for the coupling between the evanescent wave and the surface Plasmon to occur, the propagation constant of the evanescent wave β_i and that of the surface Plasmon β_{sp} have to be equal:

$$\beta_i = \mathrm{Re}\left\{\beta_{sp}\right\} \tag{1-6}$$

Thus

$$\left(\frac{2\pi}{\lambda}\right) n * sin\theta_i = Re\left\{\left(\frac{2\pi}{\lambda}\right) * \sqrt{\frac{\varepsilon_m * \varepsilon_d}{\varepsilon_d + \varepsilon_m}}\right\} \tag{1-7}$$

The dielectric constant of metals at optical wavelengths is complex [51]:

$$\varepsilon_m = \varepsilon_{m(Re)} + i * \varepsilon_{m(Im)} \tag{1-8}$$

which is equal to the square of the complex refractive index [52] :

$$\varepsilon_m = \varepsilon_{m(Re)} + i * \varepsilon_{m(im)} = \dot{\eta}^2 = (n + i * k)^2 = (n^2 - k^2) + i * 2nk \tag{1-9}$$

Where k is the extinction coefficient or the index of absorbtion or imaginary part of the complex refractive index. In most cases the Drude *model* is invoked to characterize the frequency dependence of the metallic dielectric function:

$$\varepsilon_m = 1 - \frac{w_p^2}{w(w + i\gamma)} \tag{1-10}$$

where ω_p is the bulk plasma frequency, γ is the relaxation time [52]*:*

$$w_p = \left(\frac{N e^2}{\varepsilon_0 m_e}\right)^{1/2} \tag{1-11}$$

where N is the density of conduction electrons, m_e is their effective optical mass and e is the charge of the electron.

It has to be noted that the complex refractive index of gold at 1550 nm is [53] equal to $\dot{\eta} = 0.55 + 11.5\ i$. Also the permittivity of Au is equal to $\varepsilon_{Au} = -131.95 - i\ 12.65 = \dot{\eta}^2$ [51].

In the subsequent paragraphs, we introduce a theoretical analysis and model of the SPR on three layers consisting of dielectric–metal–dielectric interface as can be seen in Fig. 10. The magnetic

field component of SPR on this interface for a gold metal film of different thicknesses where the SPR can exist in the form of transverse magnetic (TM) wave has been simulated. TM meaning that only electric fields E_x, E_z and the magnetic field H_y exist (x is normal to the surface, z and y run along the surface with z being the direction of propagation). The model represents the theoretical analysis of the SPR on three layers planar device consisting of dielectric–metal–dielectric interface. As the geometry of the SPR optical fiber sensor is more complicated, the single-mode optical fiber can be substituted by an equivalent single-mode planar waveguide with an identical propagation constant of the mode. The resulting planar SPR sensor structure can be analyzed using the mode expansion and propagation method [54], [55]. Also, the structure can be analyzed using a simple first-order perturbation method proposed by Kumar and Varshney [56]–[58] where the core of the fiber is considered as a perturbed scheme of an equivalent rectangular core region characterized by a separable index profile keeping the same area and aspect ratio. In order to obtain the respective propagation constants and field distributions, wave equations are then solved for the equivalent rectangular waveguide. Finally, a first order correction is used to obtain the propagation constants of the mode of the given fiber structure by considering the dielectric constant difference between the two structures [25], [29].

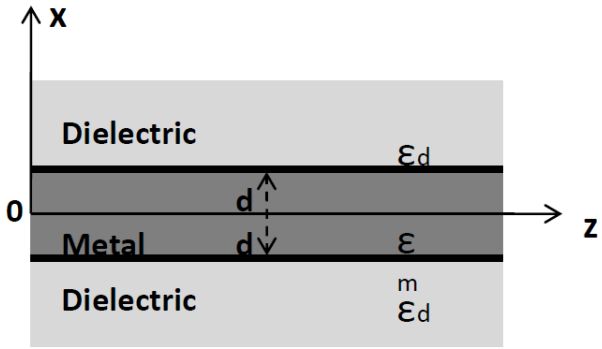

Fig. 10. Gold metal layer sandwiched between two infinite dielectric layers.

The electrical field and the magnetic field components where the modal fields are solutions to the following source-free Maxwell equations [2]:

$$\nabla . D = 0 \tag{1-12}$$

$$\nabla . B = 0 \tag{1-13}$$

$$\nabla x\, E = -\mu_0 \frac{\partial H}{\partial t} \tag{1-14}$$

$$\nabla x\, H = \varepsilon_0 n^2 \frac{\partial E}{\partial t} \tag{1-15}$$

where E is the electric field (v/m), B is the magnetic field (tesla), D is the electric displacement field (coulomb/m^2), and H is the magnetizing field (A/m).

$\varepsilon_0 = 8.85.* 10^{-12}\ F/m$, is the permittivity of free space and μ_0 is the permeability of free space (H/m).

$\nabla.$ is the divergence operator (1/m) and ∇x is the curl operator (1/m)

where the curl vector differential operator is defined as follows:

$$\nabla x\, H = \left(\frac{\partial H_z}{\partial y} - \frac{\partial H_y}{\partial z}\right) x_0 + \left(\frac{\partial H_x}{\partial z} - \frac{\partial H_z}{\partial x}\right) y_0 + \left(\frac{\partial H_y}{\partial x} - \frac{\partial H_x}{\partial y}\right) z_0 \tag{1-16}$$

where H = (H_x, H_y, H_z) are scalar and vector functions on Cartesian coordinates(x,y,x) and $x_0, y_0\ and\ z_0$ are unit vectors. The modal fields can be expressed in the forms:

$$E = e(x,y)e^{i(wt-\beta z)} \tag{1-17}$$

$$H = h(x,y)e^{i(wt-\beta z)} \tag{1-18}$$

β is the propagation constant, w is the radial frequency of radiation connected with the wavelength $\lambda = 2\pi c/w$.

By solving (1-15) with respect to x:

$$\frac{\partial H_z}{\partial y} - \frac{\partial H_y}{\partial z} = \varepsilon_0 n^2 \frac{\partial E_x}{\partial t} \tag{1-19}$$

Thus

$$i\,\beta\, H_y = \varepsilon_0 n^2\, i\, w\, E_x \tag{1-20}$$

Thus

$$E_x = \frac{\beta}{\varepsilon_0 n^2\, w}\, H_y \tag{1-21}$$

By solving (1-15) with respect to z:

$$\frac{\partial\, H_y}{\partial x} - \frac{\partial\, H_x}{\partial y} = \varepsilon_0 n^2\, \frac{\partial\, E_z}{\partial t} \tag{1-22}$$

Thus

$$\frac{\partial\, H_y}{\partial x} = \varepsilon_0 n^2\, i\, w\, E_z \tag{1-23}$$

Thus

$$E_z = \frac{1}{i\, \varepsilon_0 n^2\, w}\, \frac{\partial\, H_y}{\partial x} \tag{1-24}$$

Using equation (1-14) with respect to y, we have

$$\frac{\partial\, E_x}{\partial z} - \frac{\partial\, E_z}{\partial x} = -\mu_0\, \frac{\partial\, H_y}{\partial t} \tag{1-25}$$

on solving we get

$$-i\beta\, E_x - \frac{\partial\, E_z}{\partial x} = -\mu_0\, i\, w\, H_y \tag{1-26}$$

and then we get

$$-i\beta^2\, \frac{1}{\varepsilon_0 n^2\, w}\, H_y - \frac{1}{i\, \varepsilon_0 n^2\, w}\, \frac{\partial^2\, H_y}{\partial x^2} = -\mu_0\, i\, w\, H_y \tag{1-27}$$

Thus

$$\frac{\partial^2\, H_y}{\partial x^2} = H_y\, (-\varepsilon_0 n^2\, w^2\, \mu_0 - \beta^2\,) \tag{1-28}$$

$$\frac{\partial^2\, H_y}{\partial x^2} = H_y\, (\beta^2 - n^2\, \frac{w^2}{c^2}\,) \tag{1-29}$$

Thus

$$\frac{\partial^2\, H_y}{\partial x^2} = H_y\, (\beta^2 - k^2\, \varepsilon\,) = H_y\, \gamma^2 \tag{1-30}$$

where $k = \frac{2\pi}{\lambda}$ is the vacuum wave number and $\gamma^2 = \beta^2 - k^2\varepsilon$ and

$$\gamma_1^2 = \gamma_3^2 = \beta^2 - \kappa^2 \varepsilon_d \tag{1-31}$$

$$\gamma_2^2 = \beta^2 - \kappa^2 \varepsilon_m \tag{1-32}$$

For the dielectric and by solving (1-30)

$$H_y(x) = \begin{cases} Ae^{-\gamma_1 x}, & x > d \\ Ce^{\gamma_1 x} & x < -d \end{cases} \tag{1-33}$$

and for the metal:

$$\begin{aligned} Antisymmetric\ SP\colon\ H_y(x) &= B\sinh(\gamma_2 x), \qquad |x| < d \\ Symmetric\ SP\colon\ H_y(x) &= B\cosh(\gamma_2 x), \qquad |x| < d \end{aligned} \tag{1-34}$$

This gives none-zero electric and magnetic field components for the symmetric and anti-symmetric modes.

All field components of the SPR propagating in the planar structure along the z-axis contain a common factor $e^{i(wt-\beta z)}$ where β is the propagation constant, w is the radial frequency of radiation connected with the wavelength $\lambda = 2\pi c/w$.

Each layer of the structure can be characterised by the phase parameters:

$$\begin{aligned} \gamma_1^2 = \gamma_3^2 &= \beta^2 - \kappa^2 \varepsilon_d \\ \gamma_2^2 &= \beta^2 - \kappa^2 \varepsilon_m \end{aligned} \tag{1-35}$$

κ is the vacuum wave number and $\varepsilon_m, \varepsilon_d$ are the relative permittivity of the gold film and dielectric, respectively. The relative permittivity of gold is given by $\varepsilon_m = -131.96 - 12.69i$ and the relative permittivity of silica as dielectric is equal to 1.444^2. So the magnetic field of the symmetric mode in the structure can be presented as:

$$H_y(x) = \begin{cases} Ae^{-\gamma_1 x}, & x > d \\ B\cosh(\gamma_2 x), & |x| < d \\ Ce^{\gamma_1 x} & x < -d \end{cases} \tag{1-36}$$

The boundary conditions of Maxwell's equations require that the components of the electric and magnetic field intensity vectors parallel to the boundaries of the wave guiding layer are

continuous at the boundaries ($x = d$ and $x = -d$). Applying the boundary conditions at our structure gives:

$H_y(x)\ at\ x = d$:

$$Ae^{-\gamma_1 d} = B\cosh(\gamma_2 d) \tag{1-37}$$

$E_z(x)\ at\ x = d$:

$$\gamma_2 \frac{B}{\varepsilon_m}\sinh(\gamma_2 d) = \frac{-A}{\varepsilon_d}\ \gamma_1 e^{-\gamma_1 d} \tag{1-38}$$

Dividing the last two equations gives the following eigenvalue equation which determines β using equations (1-35):

$$\tanh(x) = -\frac{\varepsilon_m}{\varepsilon_d}\sqrt{1 - \frac{v^2}{x^2}} \tag{1-39}$$

$$x = \gamma_2 d\ and\ v = \kappa d\sqrt{\varepsilon_d - \varepsilon_m}$$

The constant A, B and C can be calculated from the boundary condition of $H_y(x)$ at both $x = d$ and $x = -d$ as follow:

$H_y(x)\ at\ x = d$:

$$Ae^{-\gamma_1 d} = B\cosh(\gamma_2 d) \tag{1-40}$$

$H_y(x)\ at\ x = -d$:

$$Ce^{-\gamma_1 d} = B\cosh(-\gamma_2 d) = B\cosh(\gamma_2 d) \tag{1-41}$$

Thus

$$A = C = Be^{\gamma_1 d}\cosh(\gamma_2 d) \tag{1-42}$$

Fig. 11 shows the real and imaginary component of the magnetic field of symmetric mode SPR when the gold film thickness is equal to 40 nm.

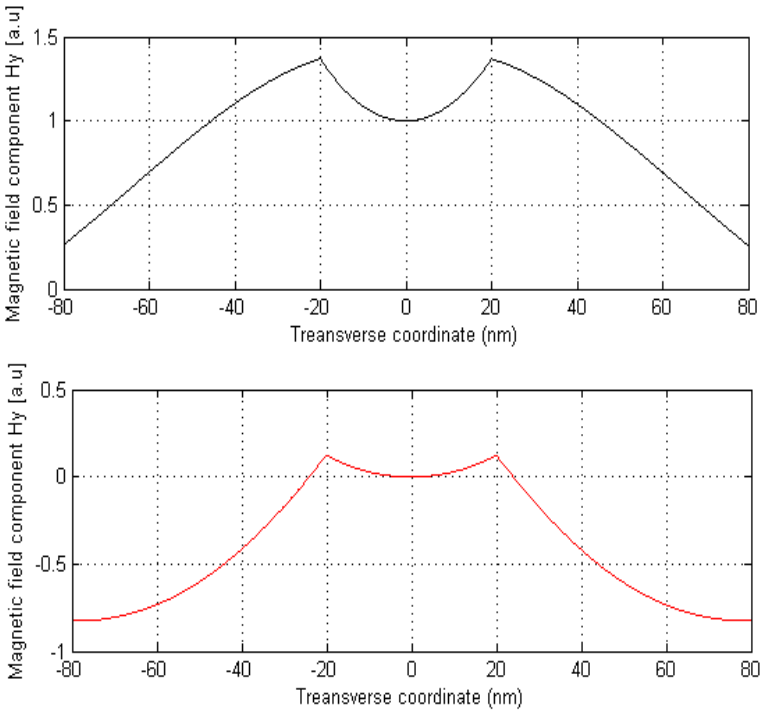

Fig. 11. Simulation results of the real component of H_y (top) and imaginary (bottom) profiles of SPR of symmetric mode of silica-gold-silica interface for a film thickness of 40 nm.

Similarly, the magnetic field of the anti-symmetric mode in the structure can be presented as:

$$H_y(x) = \begin{cases} Ae^{-\gamma_1 x}, & x > d \\ B\sinh(\gamma_2 x), & |x| < d \\ Ce^{\gamma_1 x} & x < -d \end{cases} \tag{1-43}$$

Applying the boundary conditions to the structure gives:

$H_y(x)\ at\ x = d$:

$$Ae^{-\gamma_1 d} = B\sinh(\gamma_2 d) \tag{1-44}$$

$E_z(x)\ at\ x = d$:

$$\gamma_2 \frac{B}{\varepsilon_m}\cosh(\gamma_2 d) = \frac{-A}{\varepsilon_d}\gamma_1 e^{-\gamma_1 d} \tag{1-45}$$

Dividing the last two equations gives the following eigenvalue equation which determines β using equations (1-35):

$$\tanh(x) = -\frac{\varepsilon_d}{\varepsilon_m}\sqrt{\frac{1}{1-\frac{v^2}{x^2}}} \tag{1-46}$$

$$x = \gamma_2 d \; and \; v = \kappa d\sqrt{\varepsilon_d - \varepsilon_m}$$

The constant A, B and C can be calculated from the boundary condition of $H_y(x)$ at both $x = d$ and $x = -d$ as follow:

$H_y(x) \; at \; x = d$:

$$x = \gamma_2 d \; and \; v = \kappa d\sqrt{\varepsilon_d - \varepsilon_m} \tag{1-47}$$

$$Ae^{-\gamma_1 d} = B\sinh(\gamma_2 d) \tag{1-48}$$

$H_y(x) \; at \; x = -d$:

$$Ce^{-\gamma_1 d} = B\cosh(\gamma_2 d) \tag{1-49}$$

Thus

$$A = C = Be^{\gamma_1 d}\cosh(\gamma_2 d) \tag{1-50}$$

Fig. 12. shows the magnetic field component of SPR anti-symmetric mode when the gold film thickness is equal to 40 nm.

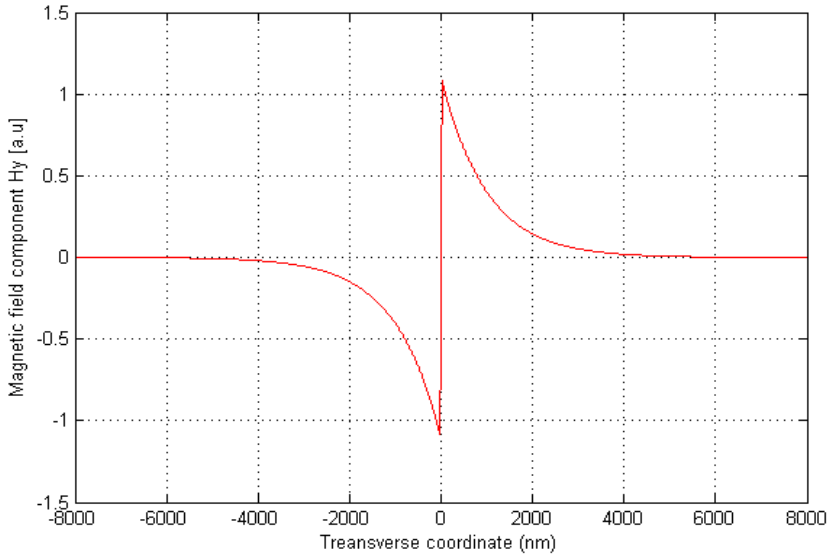

Fig. 12. Simulation of the H_y component profile of SPR anti-symmetric mode of dielectric-gold-dielectric interface for a film thickness of 40 nm.

In addition to satisfying the phase-matching condition, coupling to the SPR needs the polarization state of the cladding modes to be matched to the SPR, since only the *p*-polarisation state (TM mode) is allowed; SPR only couples to one polarisation only. In the following paragraph, we show that only the TM mode can excite the SPR. We use a planar structure consisting of a metal-dielectric interface as an example to simplify the proof. As was mentioned earlier, the dielectric constant distribution is,

$$\varepsilon(x) = \begin{cases} \varepsilon_d \text{ for } x > 0 \text{ (dielectric)} \\ \varepsilon_m \text{ for } x < 0 \text{ (metal)} \end{cases} \tag{1-51}$$

Typically ε_m is a complex quantity with its real part being negative and much larger than the imaginary part. Firstly, we obtain the solutions of the wave equation of the TM mode and see under what conditions the interface supports a surface wave. The wave equation to be solved for the TM mode is:

$$\frac{\partial^2 H_y}{\partial x^2} + \left(k_0^2 n^2 - \beta^2\right) H_y = 0 \tag{1-52}$$

i.e.

$$\frac{d^2 H_y}{dx^2} + \left(k_0^2 \varepsilon_d - \beta^2\right) H_y = 0 \quad \text{for x>0} \tag{1-53}$$

and

$$\frac{d^2 H_y}{dx^2} - \left(k_0^2 \varepsilon_m + \beta^2\right) H_y = 0 \quad \text{for x<0} \tag{1-54}$$

We take the solutions of the form,

$$H_y = \begin{cases} Ae^{-\gamma_d x}; & \text{for } x > 0,\ \gamma_d^2 = \beta^2 - k_0^2 \varepsilon_d \\ Be^{+\gamma_m x}; & \text{for } x < 0,\ \gamma_m^2 = \beta^2 + k_0^2 \varepsilon_m \end{cases} \tag{1-55}$$

Now, applying the boundary condition, *i.e.* continuity of H_y and $\frac{1}{n^2}\frac{dH_y}{dx}$ at $x = 0$, we get,

$$A = B, \tag{1-56}$$

and,

$$-\frac{\gamma_d}{\varepsilon_d} A = -\frac{\gamma_m}{\varepsilon_m} B \tag{1-57}$$

and thus we get,

$$\frac{\gamma_d^2}{\varepsilon_d^2} = \frac{\gamma_m^2}{\varepsilon_m^2} \Rightarrow \frac{\beta^2 - k_0^2 \varepsilon_d}{\beta^2 + k_0^2 \varepsilon_m} = \frac{\varepsilon_d^2}{\varepsilon_m^2} \tag{1-58}$$

this after simplification gives,

$$n_{eff} = \frac{\beta}{k_0} = \sqrt{\frac{\varepsilon_d \varepsilon_m}{\varepsilon_m - \varepsilon_d}} \tag{1-59}$$

The above TM solution is known as effective refractive index of the surface Plasmon wave (SPW). Secondly, we try to obtain the solutions of the wave equation of the TE mode and see under what conditions the interface may support a surface wave. For the TE mode, the wave equation which has to be solved is:

$$\frac{\partial^2 E_y}{\partial x^2} + \left(k_0^2 n^2 - \beta^2\right) E_y = 0 \tag{1-60}$$

taking the solution of the form:

$$E_y = \begin{cases} Ae^{-\gamma_d x}; & \text{for } x > 0,\ \gamma_d^2 = \beta^2 - k_0^2 \varepsilon_d \\ Be^{+\gamma_m x}; & \text{for } x < 0,\ \gamma_m^2 = \beta^2 + k_0^2 \varepsilon_m \end{cases} \tag{1-61}$$

and applying the continuity of E_y and $\frac{dE_y}{dx}$ at $x = 0$ we get,

$$A = B \tag{1-62}$$

and

$$-\gamma_d A = \gamma_m B \tag{1-63}$$

this implies that,

$$\varepsilon_d = -\varepsilon_m \tag{1-64}$$

The above condition cannot be satisfied as both the ε_m and ε_d are positive quantities. This means that a dielectric-metal interface cannot support a TE mode which is actually proofs that SPR only couples to one polarisation only which is the TM mode. However in the case of SPR excitation on a metal coated optical fiber, the cladding is a circular waveguide and it supports more complicated mode structures known as hybrid modes and we cannot consider the TE or TM modes only.

The proposed schemes in this dissertation are TFBG-SPR optical fiber sensors where the TFBG are coated with metals and coupling of the cladding modes to the SPR occurs if the phase matching condition (PM) is satisfied, as was mentioned previously in chapter 1. The excited cladding modes couple to the SPR are dissipated in the metal. This happens when the effective refractive index of cladding modes is close to that of the SPR, as determined by the SRI. The PM condition between a cladding mode and the SPR can be expressed as

$$n_{cl} \sin(\theta_{cl}) = \mathrm{Re}\left(\sqrt{\frac{\varepsilon_m \times \varepsilon_d}{\varepsilon_m + \varepsilon_d}}\right) \tag{1-65}$$

where ε_m being the dielectric constant of the metal , ε_d is the dielectric constant of the sensing medium around the metal, n_{cl} is the cladding refractive index, and θ_{cl} is the angle of the cladding mode ray incident on the cladding-metal interface.

Each cladding mode represents an optical ray striking the cladding-metal boundary at some angle of incidence according to the geometrical optics picture. The reflectance with respect to the incidence angle can be calculated in the Kretschmann configuration using the matrix method for a number of layers including the cladding, the coating, and the SRI [59], [60]. The reflection coefficient of the model for *p*-polarized light is $R=|r_p|^2$, where r_p is the amplitude reflection coefficient given by:

$$r_p = \frac{(M_{11} + M_{12} q_N) q_1 - (M_{21} + M_{22} q_N)}{(M_{11} + M_{12} q_N) q_1 + (M_{11} + M_{12} q_N)} \tag{1-66}$$

where:

$$M_d = \begin{pmatrix} \cos \beta_d & -i \sin \beta_d / q_d \\ -i q_d \sin \beta_d & \cos \beta_d \end{pmatrix} \tag{1-67}$$

$$q_d = (\varepsilon_d - n^2 \sin^2 \theta)^{1/2} \tag{1-68}$$

$$\beta_d = t_d (2\pi / \lambda)(\varepsilon_d - n^2 \sin^2 \theta)^{1/2} \tag{1-69}$$

considering M as the characteristic matrix of the proposed structure consisting of *N* number of layers and where ε_d being the dielectric constant of the layer, n its refractive index, and t_d is the thickness. The resonant angle corresponds to the localised minimum in the reflection coefficient [59]. Thus the SPR resonance angle as a function of the SRI can be simulated. The results of this simulation have been introduced in chapters 4 and 6 for TFBG-SPR sensors coated with chromium and gold with/without silicon. The above approach is developed for a planar geometry where it is possible to use this approach to predict the SPR and the cladding modes coupling, but still there is a need to develop a complete model taking into account the circular geometry of the optical fiber into account and to study how the results supported by the geometry of optical fiber differs from the results supported by the planar geometry.

1.4 Objectives

The objective of this dissertation is to develop novel SPR sensors using TFBGs which may provide a unique opportunity to improve the performance of SPR sensors. This improvement of SPR performance can be achieved through capturing the cladding modes in reflection and to use the reflection spectrum to interrogate the SPR. Also, multiplexing and distributed SPR sensors in single optical fiber has high impact. The sensitivity along the strong electromagnetic field generated by gold and silicon-coated TFBGs is advantageous. Also, the proposed structures are also free from any moving parts allow sensing in inaccessible conditions with the ability to transmit signals easily over long distances. At the same time, the proposed SPR-TFBGs sensors will certainly have an impact in multi-analyte sensing and reducing costs of traditional surface Plasmon resonance sensor instruments. To achieve these objectives, a few steps have been identified, corresponding to the main components of the realization of these devices:

1.4.1 Design step

This step consists of covering the state-of-art work in the field by literature review, design the experimental schemes proposed in this dissertation, and then theoretical analysis and modelling the behaviour of the proposed sensor when coated with gold and silicon by obtaining the reflectance with respect to the incident angles and the dependence of the resonant SPR and the cladding modes incident angles on the SRI.

1.4.2 Fabrication and implementation step

The second step consists of developing a procedure for the fabrication and characterization of such novel sensor structures including experimental investigation and analysis. Also, it requires measuring and quantifying the improvement and enhancements achieved experimentally by the fabricated SPR sensor.

1.4.3 Validation step

The goal of the final step is to demonstrate the improvement for surrounding refractive index (SRI) measurement in real time.

1.5 Note on collaborations

The proposed project has been achieved in partial collaboration with Prof. Caroline Boudoux and Prof. Nicolas Godboux groups, LODI and FOL Labs, from Polytechnique Montreal in order to fabricate the double-clad fiber coupler.

CHAPTER 2 INTRODUCTION TO BRAGG GRATINGS

Fiber Bragg gratings (FBGs) and tilted fiber Bragg gratings (TFBGs) written in optical fibers are the key elements of the proposed sensors. They have been used in this dissertation to excite the cladding modes which in turn have been used for SPR sensing. This chapter presents the theory of Bragg gratings and the various techniques to fabricate the gratings. The theory and the fabrication techniques of TFBGs are highlighted. The phenomenon of photosensitivity which allows writing Bragg gratings in optical fibers is introduced in Appendix A.

Fiber Bragg gratings (FBGs) written in optical fibers have attracted considerable interest in the past three decades as a key technology in variously expandable applications. The optical fibers and FBGs have made an enormous impact on modern telecommunication systems. It is believed that there will be an increased use of such devices in many applications, e.g. wavelength-division-multiplexed systems, viable routing schemes, and channel selection [22]. FBGs contributes in the creation of optical fiber amplifiers, as every semiconductor pump laser has one [22]. Not only does the FBG have applications in telecommunications systems, but also in the area of sensing. The number of FBGs application in sensing has still been exploded, with oil, temperature, and gas exploration. Furthermore, FBGs are finding applications in unusual biomedical areas as to be commercialized further like tumor detection and post-trauma care [22].

FBG can be fabricated using different techniques like holographic, and non-interoferometric techniques [22], [61], [62]. The holographic techniques are based on a beam splitter which divides a UV beam into two interfering beams overlapping at the fiber. On the other hand, the non-interferometric methods use a spatially periodic amplitude mask. The interferometer inscription techniques falls in the holography category where a UV beam divided into two at a beam splitter and then the two beams overlap together on the fiber by using two mirrors as a beam combiner [63]. By using the interferometer, the Bragg wavelength can be chosen independently of the UV laser wavelength [22]. A phase mask, a relief grating etched in a silica plate, can be used instead of the beam splitter as a wavelength defining element with the mirrors to adjust the wavelength of the fiber grating [22]. The phase mask can be scanned using a translation stage for inscribing longer gratings in the fiber [64]. This chapter presents the different

techniques which has been used in this dissertation. It also describe the phenomenon of photosensitivity and the theory of Bragg gratings.

2.1 Basic concepts of fiber Bragg gratings

A fiber Bragg grating is simply an optical diffraction grating. Its effect upon a light wave incident on the FBG at an angle θ_1 and diffracted at an angle θ_2 can be described by the familiar grating equation as follow [65]:

$$n \sin \theta_2 = n \sin \theta_1 + m * (\lambda / \Lambda) \tag{2-1}$$

where Λ is the grating period, λ the wavelength in vacuum, n the refractive index and m is the integer which determines the diffraction order as can be seen in Fig. 13.

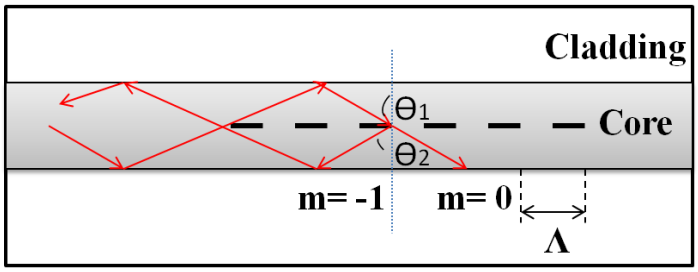

Fig. 13. Ray-optic illustration of core-mode Bragg reflection by a fiber Bragg grating

In the case of an optical fiber $n_{eff} = n_{co} * \sin \theta$ where n_{eff} is the effective refractive index of the fiber core and n_{co} is the core refractive index. Fig. 13 shows the reflection by a Bragg grating of a mode into the same mode traveling in the opposite direction with a diffracted angle of $\theta_1 = -\theta_2$, giving the Bragg condition when m= -1 for the first-order diffraction, which usually dominates in a fiber grating:

$$\lambda_B = 2 n_e \Lambda \tag{2-2}$$

where λ_B is the Bragg wavelength. The Bragg grating condition is the requirement to satisfy both energy and momentum conservation. For energy conservation, the frequency of the incoming light must match that of the reflected light:

$$h\nu_i = h\nu_r \tag{2-3}$$

where *h* is Planck's constant and *v is the* frequency. On the other hand, the momentum conservation implies that the incident wave vector K_{core}, plus the grating wave vector K_G, are equal to the radiated wave vector K_R:

$$K_R = K_{core} + K_G \tag{2-4}$$

where the grating wave vector K_G has a direction normal to the grating plane with a magnitude equal to $2\pi/\Lambda$. The diffracted wave vector K_R is equal in magnitude to the incident wave vector K_{core} ($2\pi n_{eff}/\lambda$) with opposite direction. Thus, the momentum conservation condition can be simplified as the first order Bragg condition which has been illustrated in equation (2-2).

The basic parameters characterizing a Bragg grating are shown in Fig. 14. The coupled mode theory which has been described in details in Appendix A is usually used to define these parameters. The reflectivity, or the strength of the gratings, is a function of the modulation index Δn and of the length of the grating L [66]. Typically, the modulation index can vary between 10^{-7} and 10^{-2}, depending on the type of fiber, on the exposure time and on the laser which is used. To reach values as high as 10^{-2}, the use of hydrogen loaded fiber is recommended as was mentioned earlier [22].

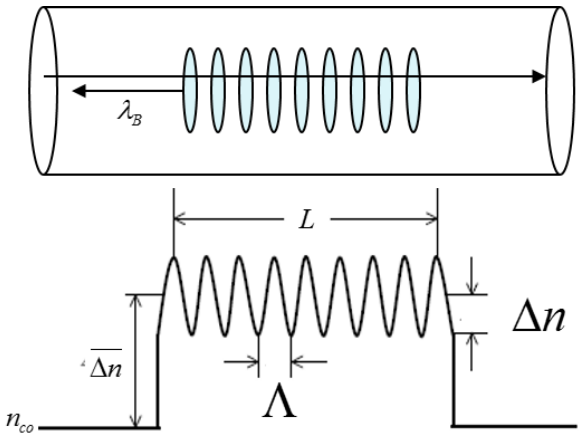

Fig. 14. Schematic representing fiber Bragg gratings.

Taking the periodic refractive index modulation of the form:

$$\Delta n(z) = \overline{\Delta n}\left\{1 + \nu \sin\left(\frac{2\pi}{\Lambda} z\right)\right\} \tag{2-5}$$

where, $\overline{\Delta n}$ is the average refractive index change over a single period of the grating in the grating region, ν is the visibility of the fringes, and Λ is the grating period. The amplitude of the *ac* part of the refractive index variation Δn is thus, $\Delta n = \overline{\Delta n}\,\nu$. A Bragg grating has in general sinusoidal index change at the core of the fiber. This periodic perturbation causes a coupling between different modes of different propagation constants if the condition of phase matching is satisfied:

$$\beta_1 = \beta_2 \tag{2-6}$$

where β_1 and β_2 are the propagation constants of the modes propagating in opposite directions. The phase mismatch of this condition is expressed as:

$$\Delta\beta = \beta_1 - \beta_2 \tag{2-7}$$

adding a term associated with the periodic perturbation of the Bragg grating [66]:

$$\Delta\beta = \beta_1 \pm \beta_2 - \frac{2\pi N}{\Lambda} \tag{2-8}$$

where Λ is the grating period and N is an integer. If both β_1 and β_2 have positive signs, then the phase-matching condition is satisfied $\Delta\beta = 0$ for counter-propagating modes; and if they have opposite signs, then the interaction is between co-propagating modes [22].

The following differential equations are used to calculate the characteristics of the amplitudes of the two modes propagating through the Bragg grating [66]:

$$\frac{\partial A_1}{\partial z} = -i\kappa_{dc} A_1 - i\kappa_{ac}^{*} B_2 e^{i(\Delta\beta z - \phi(z))} \tag{2-9}$$

$$\frac{\partial B_2}{\partial z} = i\kappa_{dc} B_2 + i\kappa_{ac} A_1 e^{-i(\Delta\beta z - \phi(z))} \tag{2-10}$$

where A_1 and B_2 represent the amplitude of the reflected and incident mode, respectively and $\phi(z)$ is the phase of the wave. κ_{dc} is the dc coupling constant associated with the change in average index modulation $\overline{\Delta n}$ as follow:

$$\kappa_{dc} = \frac{4\pi\eta\overline{\Delta n}}{\lambda} \tag{2-11}$$

where $\eta \approx 1$ is the overlap integral between modes. κ_{dc} may also include an imaginary part that is based on the absorption or gain of the fiber. κ_{ac} is the ac coupling constant associated with the modulation index of the Bragg grating as a function of the visibility υ by [22]:

$$\kappa_{ac} = \frac{\upsilon}{2}\kappa_{dc} \tag{2-12}$$

To solve equations (2-9) and (2-10) the following consideration should be taken into account for the forward and backward propagating modes:

$$R = A_1 e^{-i\left(\Delta\beta z - \phi(z)\right)/2} \tag{2-13}$$

$$S = B_2 e^{i\left(\Delta\beta z - \phi(z)\right)/2} \tag{2-14}$$

Differentiating equation (2-13) and (2-14) and substituting into equation (2-9) results in the following coupled-mode equation s:

$$\frac{dR}{dz} + i\left[\kappa_{dc} + \frac{1}{2}\left(\Delta\beta - \frac{d\phi(z)}{dz}\right)\right]R = -i\kappa_{ac}^{*}S \tag{2-15}$$

$$\frac{dR}{dz} + i\left[\kappa_{dc} + \frac{1}{2}\left(\Delta\beta - \frac{d\phi(z)}{dz}\right)\right]R = -i\kappa_{ac}^{*}S \tag{2-16}$$

It is then possible to determine the analytical solution of the previous equations $d\phi(z)/dz = 0$. Whereas for a uniform grating $\upsilon = 1$, and therefore $\kappa_{ac} = \kappa_{dc}/2$ which results in the following analytical solution for the amplitude reflection coefficient:

$$\rho = \frac{S(0)}{R(0)} = \frac{-\kappa_{ac}\sinh(\alpha L)}{\delta\sinh(\alpha L) - i\alpha\cosh(\alpha L)} \tag{2-17}$$

where:

$$\delta = \kappa_{dc} + \frac{1}{2}\left(\Delta\beta - \frac{d\phi(z)}{dz}\right) \tag{2-18}$$

$$\alpha = \sqrt{\left|\kappa_{ac}\right|^2 - \delta} \tag{2-19}$$

The reflectivity of the uniform Bragg grating is given by:

$$\left|\rho\right|^2 = \frac{\left|\kappa_{ac}\right|^2\sin^2(\alpha L)}{\delta^2 - \left|\kappa_{ac}\right|^2\cos^2(\alpha L)} \tag{2-20}$$

At the wavelength where the phase matching is satisfied $\delta = 0$, and hence the reflectivity can be obtained for the grating as follow [22]:

$$\left|\rho\right|^2 = \tanh^2(\kappa_{ac}L) \tag{2-21}$$

The bandwidth of a uniform Bragg grating is generally defined as the interval between the first two zeroes of the central grating dip of the transmission spectrum. It can be given as:

$$\alpha L = \sqrt{\kappa_{ac}^2 - \delta^2 L} = i\pi \tag{2-22}$$

$$(\kappa_{ac}^2 - \delta^2)L^2 = -\pi^2 \tag{2-23}$$

where:

$$\delta = \frac{1}{L}\sqrt{\kappa_{ac}^2 L^2 + \pi^2} \tag{2-24}$$

substituting $\kappa_{dc} = 0$ and $d\phi/dz = 0$ into equation (2-24) gives:

$$\delta = \frac{\Delta\beta}{2} \tag{2-25}$$

The first zero is determined from:

$$\Delta\beta L = 2\sqrt{\kappa_{ac}^{2} L^{2} + \pi^{2}} \tag{2-26}$$

this gives:

$$\Delta\beta = \frac{4\pi n_e (\lambda_B - \lambda)}{\lambda\lambda_B} \approx \frac{4\pi n_e \Delta\lambda}{\lambda^2} \tag{2-27}$$

giving the bandwidth of a uniform grating [22]:

$$2\Delta\lambda = \frac{\lambda^2}{\pi n_e L}\sqrt{(\kappa_{ac} L)^2 + \pi^2} \tag{2-28}$$

which can be simplified considering $(\kappa_{ac} L)^2 \langle\langle \pi^2$ for a weak grating:

$$2\Delta\lambda \approx \frac{\lambda^2}{n_e L} \tag{2-29}$$

considering $(\kappa_{ac} L)^2 \rangle\rangle \pi^2$ for a strong grating, the bandwidth is hence given by:

$$2\Delta\lambda \approx \frac{\lambda^2 \kappa_{ac}}{\pi n_e} \tag{2-30}$$

Fig. 15. shows the transmission spectrum of a fiber Bragg grating written in photosensitive fiber, photosensitivity refers to the permanent change in the refractive index of glass induced by exposure to light radiation [22], at 1550 nm. The grating has a length of 3 mm and $\approx$ 1.5 nm bandwidth of between the first zeros. A weak cladding mode can be seen on the short wavelength side of the grating at 1548 nm.

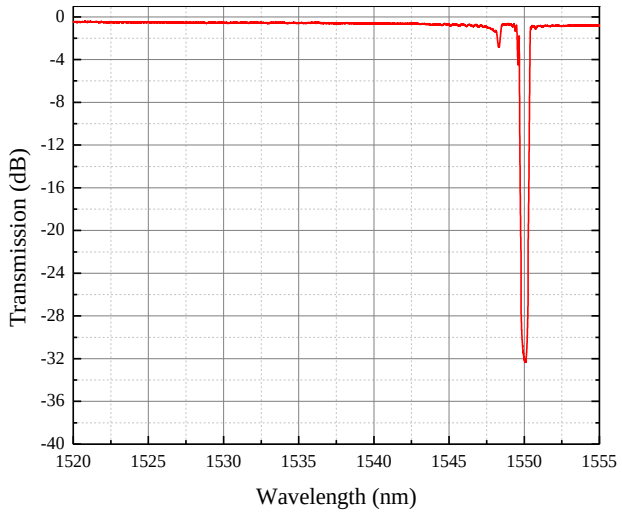

Fig. 15. Transmission spectrum of fiber Bragg gratings at 1550 nm.

2.2 Tilted fiber Bragg gratings

Cladding modes are guided modes which can be excited easily by scattering light from the core of an optical fiber into the cladding [33]. Tilted fiber Bragg gratings (TFBG) couple the forward Bragg core mode to the backward propagating cladding modes which can be observed as a series of resonance dips on the short wavelength side of the transmission spectrum [22], [34]. These modes can be excited efficiently with different tilt angles relative to the propagation axis of the fiber [22]. By simply increasing the tilt angle, stronger coupling occurs to cladding modes of relatively lower effective indices and vice versa [22].

The light components are radiated out of the fiber core in different directions with different strengths when it faces TFBG [67]. The strongest light coupling is at the phase-match condition:

$$K_R = K_{core} + K_G \tag{2-31}$$

where K_R, K_{core}, and K_G are wave vectors of the radiated light, core mode, and the grating itself, respectively. Fig. 16. shows the TFBG phase matching conditions and it can be seen that the relationship between the amplitudes of K_R and K_{core} is given by [67]:

$$K_R = \frac{K_G}{2\cos(\theta)}, (\delta = \pi - 2\theta) \tag{2-32}$$

where δ and θ are the radiation and tilted angle of the TFBG, respectively.

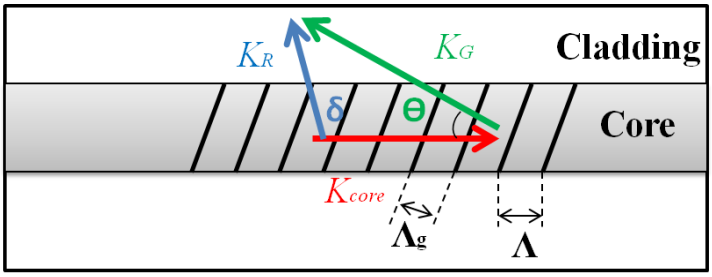

Fig. 16. Phase matching and wavevectors of TFBG with tilt angle < 45°.

The incident wavevector K_{core} is equal to:

$$K_{core} = \frac{2\pi n_{eff}^{n}}{\lambda} \tag{2-33}$$

K_G as the grating wavevector is given by:

$$K_G = \frac{2\pi}{\Lambda_g}\cos\theta \tag{2-34}$$

The radiated wavevector K_R is given by:

$$K_R = \frac{2\pi n_{eff}^{m}}{\lambda} \tag{2-35}$$

where n_{eff}^{m} and n_{eff}^{n} are the effective indices of the modes to be coupled at λ .Taking into account that the radiated wave vector is opposite in direction to the incident wave vector and that the modified tilted period Λ_g is equal to ($\Lambda / \cos\theta$), gives the Bragg resonance condition for TFBG as:

$$\frac{2\pi n_{eff}}{\lambda_B} + \frac{2\pi n_{eff}}{\lambda_B} = \frac{2\pi}{\Lambda_g}\cos\theta \tag{2-36}$$

So the effective refractive index of a cladding mode can be calculated from the Bragg phase-matching resonant condition of the TFBG by [22]

$$n_{eff}^{clad} = \frac{\lambda_{cl} \times \cos(\theta)}{\Lambda_g} - n_{eff}^{core} \tag{2-37}$$

where θ is the tilt angle with respect to the plane of the propagation axis in the fiber, Λ is the grating period, and n_{eff} is the effective refractive index of the core mode at the resonant wavelength (λ_{cl}).

Imprinting TFBG in a fiber is equivalent to introducing a spatially dependent phase $\phi(r,\varphi,\theta)$ in the grating [68], with a uniform refractive-index modulation of Δn_{mod} giving as:

$$\Delta n = \Delta n_{\mathrm{mod}} \cos[2\pi z / \Lambda + \phi(r,\varphi,\theta)] \tag{2-38}$$

where

$$\phi = \frac{2\pi r \cos\varphi \tan\theta}{\Lambda} \tag{2-39}$$

The strength of the coupling between the core mode $\Psi(r)$ and the other coupled mode $\Psi(r,\varphi)$ is measured by the effective refractive index modulation $\overline{\Delta n}$ of the coupling where $\Psi(r)$ is the normalized field distribution in polar coordinates represents the electric or the magnetic field of the guided fundamental core mode. The fundamental core mode has only a radial dependence. The effective refractive index modulation $\overline{\Delta n}$ is given by [68]

$$\overline{\Delta n} = \int_0^{2\pi}\int_0^{\infty} \Delta n_{\mathrm{mod}} \Psi(r)\Psi_{lm}(r,\varphi)\exp(j\phi) r\,dr\,d\varphi \tag{2-40}$$

The overlap integral OI is a measure indicator of the coupling strength between two modes due to the TFBG and is determined by the modal distribution of the two modes involved and the distribution of the grating:

$$OI = \int_0^{2\pi}\int_0^{\infty} \Psi(r)\Psi_{lm}(r,\varphi)\exp(j\phi) r\,dr\,d\varphi \tag{2-41}$$

and thus [68]

$$\overline{\Delta n} = OI * \Delta n_{\mathrm{mod}} \tag{2-42}$$

As was mentioned earlier, the strength of the grating resonances depends on the coupling coefficient k between the incident core mode and the mode that is phase matched, and on the length L of the grating according to equation (2-21).

The wavelength at which the cladding mode begins can be calculated from [22]

$$\lambda_{start} = \frac{\lambda_{Bragg}}{2}(1 + \frac{n_{clad}}{n_{eff}}) \quad (2\text{-}43)$$

where λ_{start} indicates the wavelength at which the cladding mode coupling begins, n_{eff} is the effective refractive index of the core mode at the Bragg resonant wavelength (λ_{Bragg}), and n_{cl} is the cladding refractive index. Fig. 17. shows the transmission spectrum of a 6° TFBG written in photosensitive fiber. The grating has a length of 10 mm. The transmission spectrum consists of two bands: a weak core mode resonance at 1586 nm and a set of resonances from the cladding modes on the short wavelength side of the core resonance. Cladding mode resonances begin at a wavelength of 1584 nm and consist of low-order cladding modes as well as many high-order cladding modes.

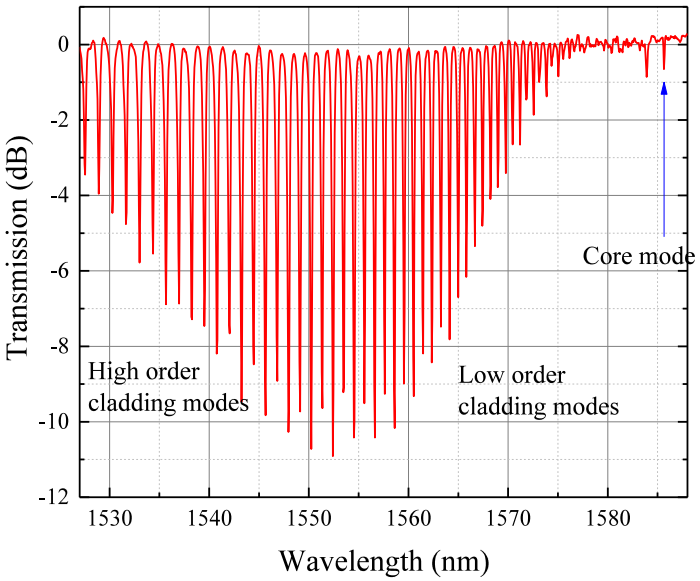

Fig. 17. Transmission Spectrum of 6° TFBG written in photosensitive fiber.

2.3 Fabrication of Bragg gratings

Different techniques can be used to write Bragg gratings. This thesis describes the techniques which have been used to write the FBGs and TFBGs experimentally in order to accomplish the objectives of this dissertation.

The first technique which have been used is the scanning phase mask with 224 nm laser. The phase mask is a relief grating etched in a silica plate transparent to UV. The depth of the slots of

the grating etched is designed to minimize the intensity diffracted in the zero order and to maximize the intensity in the order ±1 as can be seen in Fig. 18.

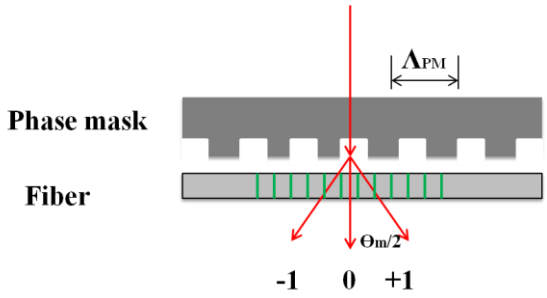

Fig. 18. Scheme of the phase mask.

The incident and diffracted orders of the phase mask satisfy the general diffraction equation:

$$\Lambda_{pm} = \frac{m\lambda_{uv}}{(\sin\frac{\theta_m}{2} - \sin\theta_i)} \tag{2-44}$$

where $\theta_m / 2$ is the angle between the beam and the normal, θ_i the incident angle of the beam relative to the normal, λ_{uv} the wavelength of the incident light and Λ_{pm} is the period of the phase mask. The interference pattern at the fiber of the orders ±1 has a period Λ_{pm} related to the diffraction angle $\theta_m / 2$ by

$$\Lambda_g = \frac{\lambda_{uv}}{2n_{uv}\sin\frac{\theta_m}{2}} = \frac{\Lambda_{pm}}{2} \tag{2-45}$$

Bragg gratings was imprinted using the scanning phase mask by a commercially available source, the new laser is 224nm Nd:YVO_4 laser which produces pulses of 7 ns and 30 μJ at a frequency between 0.1 and 30 kHz with a maximum average power of 300 mW [69]. Its beam is about 1 mm in diameter and is slightly elliptical. The new laser has excellent beam profile and stable laser output and it needs less electrical power than Argon laser which used for FBG fabrication. Fig. 19 shows the experimental setup of FBG fabrication where a phase mask technique is used. This simple and easy to align technique offers many advantages like good reproducibility and is its simple setup. The laser scanned the fiber with the help of the mirror on a linear translation stage and a 20 cm cylindrical lens is used to focus the light.

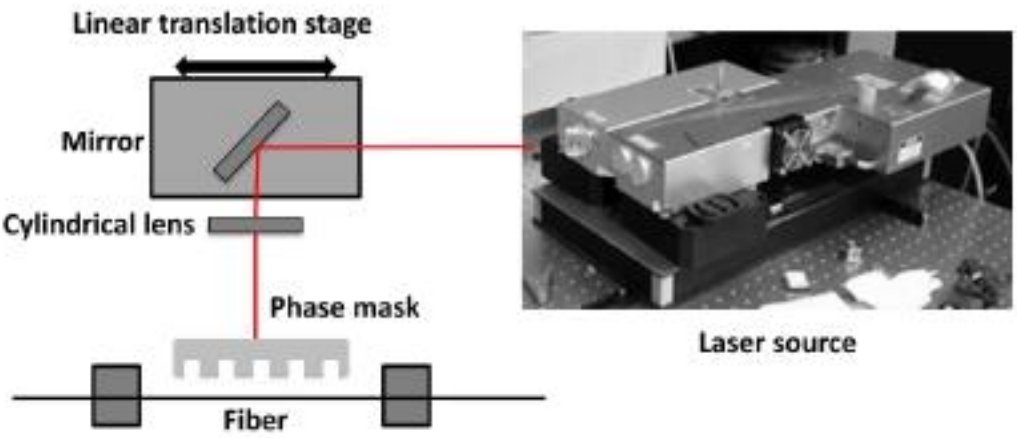

Fig. 19. Setup of the phase mask technique Bragg gratings fabrication.

Fig. 20 shows the phase mask which is used for FBG fabrication. The gratings period is fixed by the phase mask period (Λ_{pm}) [22]

$$\Lambda = \frac{N \lambda_{Bragg}}{2 n_{eff}} = \frac{\Lambda_{pm}}{2} \tag{2-46}$$

where n_{eff} is the effective mode index in the fiber, and N is an integer indicating the order of the grating period. The drawback of this technique is that the length of the written gratings is limited by phase mask to a maximum length of 2″.

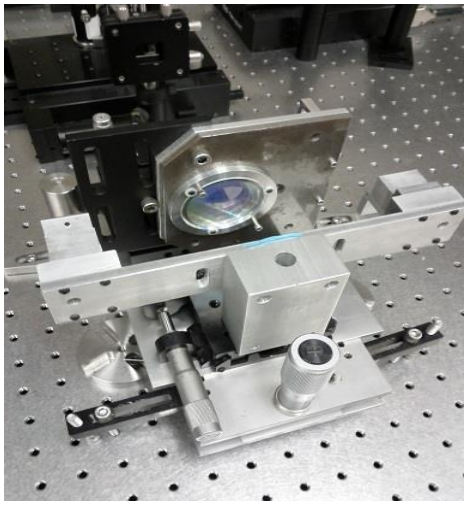

Fig. 20. Phase mask used for FBG fabrication

Fig. 21 shows a transmission spectrum of a 12 mm FBG written in high Ge doped fiber under 224 nm with 240 mW average. As can be seen, the maximum transmission loss was -17 dB, giving a gratings strength (index modulation) of $1x10^{-4}$ calculated using the following equation s as was mentioned earlier [22]:

$$L \approx \frac{\lambda_{Bragg}^{2}}{\pi n_{eff} 2\Delta\lambda}, \; R = \tanh^{2}(\kappa L), \sigma \approx \frac{4\pi\kappa\eta}{\lambda_{Bragg}} \qquad (2\text{-}47)$$

Where the overlap integral is equal to one ($\eta \approx 1$) for identical modes.

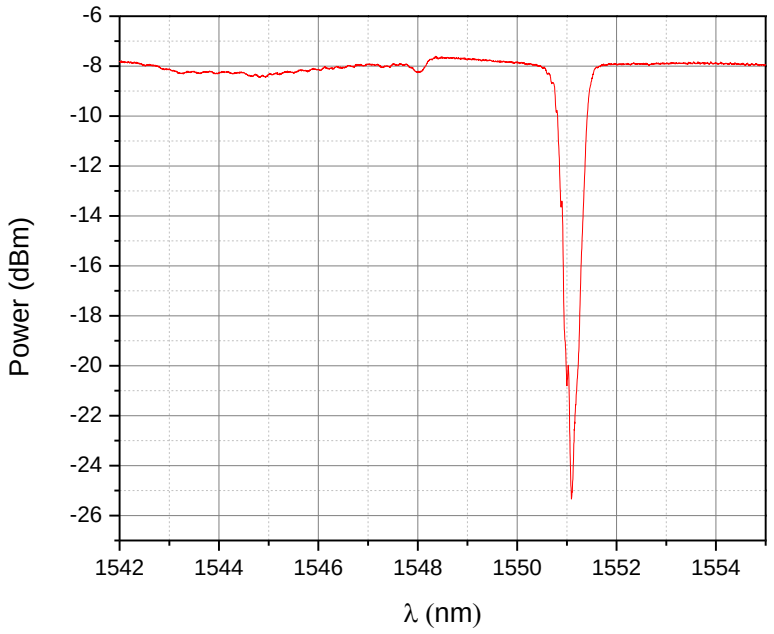

Fig. 21. Transmission spectrum of a 12 mm FBG written in a fiber with 240 mW 224 nm laser.

It can be seen clearly that the longest wavelength resonance dip corresponds to the reflection of the core mode light onto itself as Bragg wavelength while all the shorter wavelength resonances correspond to the excitation of backward-propagating cladding modes. Fig. 22 shows the gratings profile growth of B/Ge doped fiber written by the used 224 nm laser. It can be pointed out that a maximum grating strength of $8x10^{-4}$. So stronger gratings can be obtained with this laser.

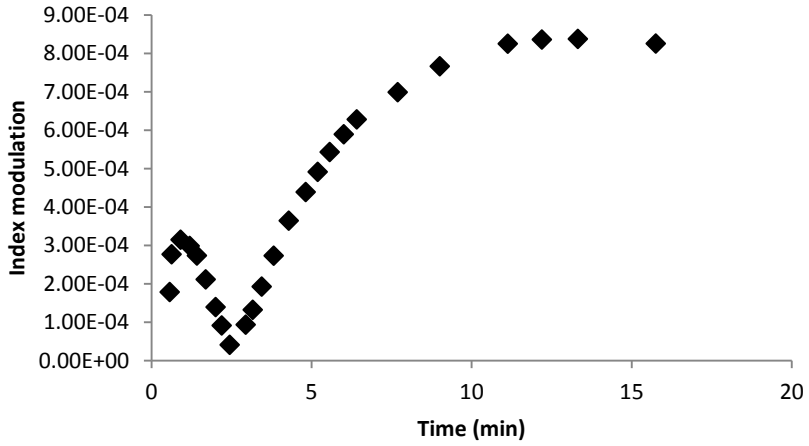

Fig. 22. Growth of the gratings strength (index modulation) for a 3 mm FBG written on a B/Ge doped for 224 nm from [69].

To overcome the drawback of having fixed grating period, the scanning phase mask Talbot interferometer, Model FBGTMI-913 from PhotoNova Inc., Montreal, Canada, has been used [22] as can be seen in Fig. 23. The interferometer inscription techniques falls in the holography category where a UV beam divided into two at the phase mask and then the two beams overlap together on the fiber by using two mirrors as a beam combiner [63]. By using the interferometer, the Bragg wavelength can be chosen independently of the UV laser wavelength [22]. The phase mask used as a beam splitter for inscription of fiber gratings. The phase mask predefines the wavelength of the reflection grating, when the mirrors are at right angles to the axis of the fiber and the phase-mask plate [22]. The phase mask can be scanned using a translation stage for inscribing longer gratings in the fiber [64].

The Bragg wavelength for a configuration with parallel mirrors can be obtained with equation (2-2). The change in the Bragg wavelength as a function of the change in the mutual angle between the two beams can be obtained as:

$$\frac{\Delta\lambda}{\lambda_{Bragg}} = \frac{\Delta\theta}{2}\cos\frac{\theta}{2} \tag{2-48}$$

where θ is the initial angle, the angle change $\Delta\theta$, λ_{Bragg} is the Bragg wavelength of the reference and the variation of the Bragg wavelength is $\Delta\lambda$.

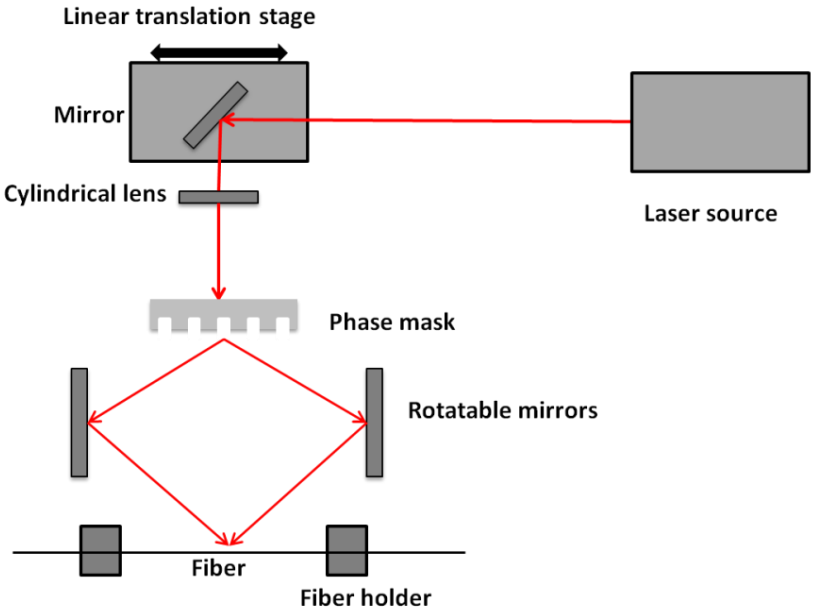

Fig. 23. Scheme of the scanning phase mask interferometer to write Bragg gratings.

The laser source which have been used with this technique is a commercially available 213 nm Q-switched nanosecond Nd:VO_4 laser (Xiton Photonics). The laser produces pulses of 7 ns with an energy of 10 μJ at a repetition frequency between 0.1 and 30 kHz with a maximum average power of 130 mW. The beam is about 1 mm in diameter and it has a relatively high wall-plug efficiency [70]. Fig. 24. shows FBG written in 1060 Flexcore fiber when the mirrors are at right angles to the axis of the fiber and the phase-mask plate showing the ability to find a reference position for the phase-mask Bragg wavelength

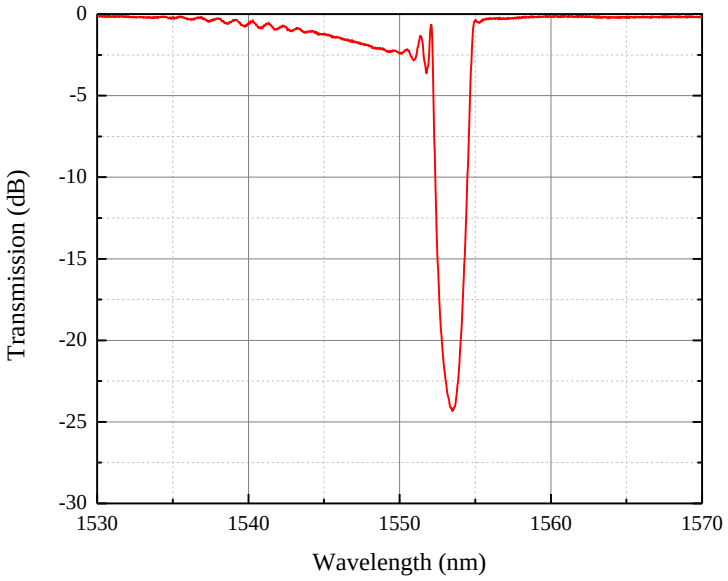

Fig. 24. FBG written the Talbot interferometer when the mirrors are at right angles to the axis of the fiber and the phase-mask plate in 1060 Flexcore fiber.

The tunability of the interferometer at different wavelengths can be adjusted easily. As was mentioned, using the interferometer allows the Bragg wavelength to be chosen independently by changing the mutual angle between the mirrors of the interferometer and the fiber plane.

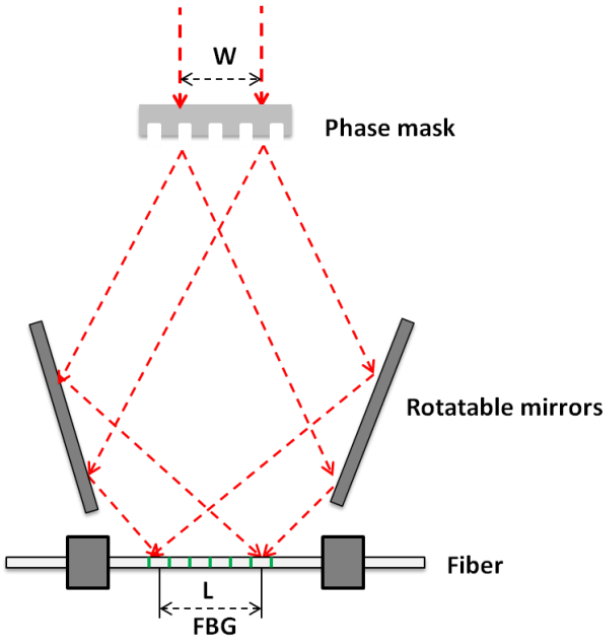

Fig. 25. Rotating the mirrors and tunning the mutual angle to write Bragg gratings at shorter wavelengths.

So two modifications are required to achieve it, The mirrors need to be rotated to a specific mutual angle, and the distance of the fiber from the phase mask has to be changed as can be seen in Fig. 25. The length of the grating L becomes higher than the beam width of the UV beam incident on the phase mask. So far the interferometer can be used to write a gratings for a bandwidth well below a Bragg wavelength of 532 nm as can be seen in Fig. 26 at 617 nm up to 1700 nm.

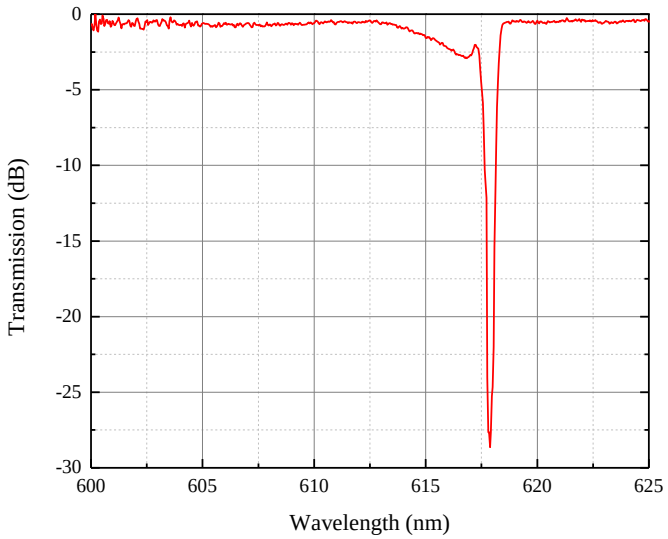

Fig. 26. FBG written in Corning RGB fiber at 617 nm by the Talbot interferometer.

TFBG can be easily written using the scanning phase mask technique by simply orienting the fiber at an angle α in the plane of the incoming UV beams as can be seen in Fig. 27. At the same time, the fiber holder has to be arranged such that the fiber location is in the vertical axis around which the fiber holder assembly is rotated to ensure that the position of the fiber center is invariant to the UV beams.

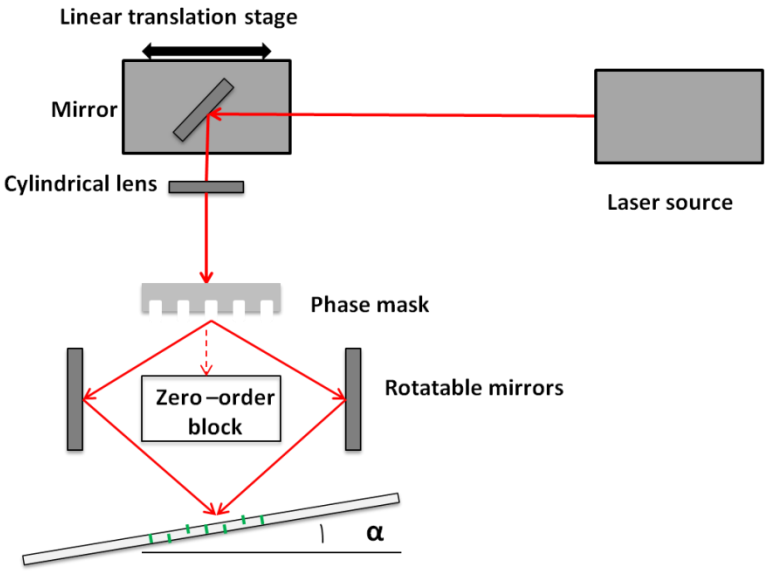

Fig. 27. Writing TFBGs with the Talbot interferometer and the scanning phase mask technique.

Hence, the distance of the fiber from the incoming beams increase in one direction and reduce in the other which change the path length difference between the interfering beams. Hence, the coherence properties of the laser will determine the visibility of the fringes. For small tilt angles α, the variation of the TFBG period Λ_s in the direction of propagation is given by:

$$\Lambda_s \approx \Lambda_g / \cos\alpha \tag{2-49}$$

Fig. 28. shows an example of TFBG written by the scanning phase mask and the interferometer in a unique fiber which have small core-cladding index difference and large ν-value as will be described in chapter 5.

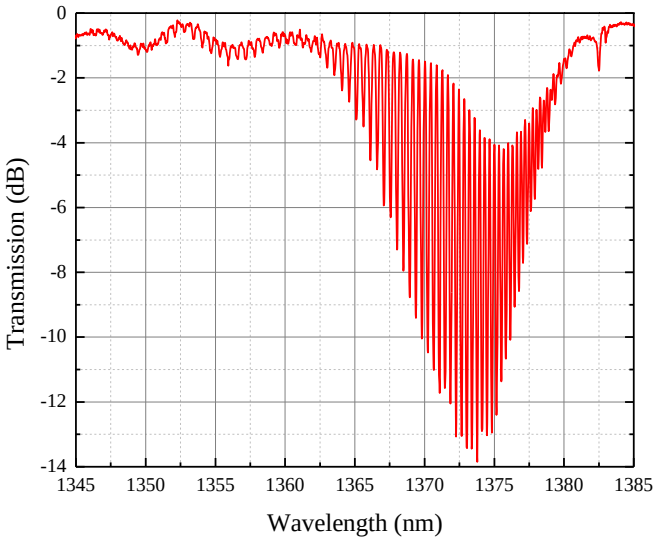

Fig. 28. TFBG written in a specially fabricated fiber by the scanning phase mask interferometer.

2.4 Coating of tilted fiber Bragg gratings

Since the proposed TFBG-SPR sensors are planned to be coated with chromium and gold as will be shown in the subsequent chapters, the coating process is consisted of coating each sample of a 2.5 nm chromium coating first in a sputtering chamber and then a gold layer of 35 nm was deposited on the TFBGs written in the optical fiber. The deposition was performed in the clean room of the LMF Microfabrication Laboratory of Polytechnique Montreal.

By the physical sputtering deposition process, particles vaporized from a surface target which can be chromium, gold or silicon. Since the optical fibers are cylindrical, characterizing the deposition thickness on the optical fiber and optimizing the process is difficult. So, we characterize each sample thickness by coating a flat glass slide first and then the optical fiber is coated. The characterization is performed by a roughness and contour measuring system (Dektak profilometer) in order to obtain the average metal thickness and to ensure that the thickness difference is minimized as can be seen in Fig. 29 for a 2.5 nm chromium layer and gold layer of 25 nm thickness. The maximum thickness error was ± 3 nm. A chromium layer of 2.5 nm requires 10 s of deposition at a pressure of 1 mTorr, and a power of 100 W. A 35 nm gold layer requires 75 s of deposition at a pressure of 10 mTorr, and a power of 50 W.

During the deposition, the fiber is positioned parallel to the sputtering target. So only one side of the cylindrical optical fiber is coated although it is desirable to have a uniform coatings. In order

to improve the uniformity of the optical fiber coatings, rotating the fiber by 180° in two exposures was performed. Hence, the thickness varies from zero to a maximum value of the desired thickness. The rotation of the fiber in the second exposure increase the distance between the sputtering target and the fiber. So the time required has to be increased. For the second exposure, the time required to deposit a 2.5 nm chromium is 25 s and for a 35 nm gold layer it is 180 s. For our proposed scheme of silicon-coated multiplexed TFBG-SPR sensors which will be presented in chapter 6, a silicon layer of 10 nm had to be deposited on the chromium and gold-coated TFBGs. Such a layer requires 23 s of deposition at a pressure of 10 mTorr, and a power of 200 W before rotating the fiber. The second exposure required a sputtering time of 67 s. The resulting deposited layer thicknesses were studied with scanning electron microscopy (SEM) and with atomic force microscopy (AFM) in order to characterize the surface smoothness as can be seen in Fig. 29.

The SPR sensor schemes proposed in this thesis relies on TFBG as a coupling element to excite SPR. Proposed sensor configurations consist of optical fibers that have TFBGs written in the core and a chromium and gold coating on the surface of the cladding. Chapter 2 is followed by four chapters which consist of three published articles and one accepted article in journals for the different TFBG-SPR schemes.

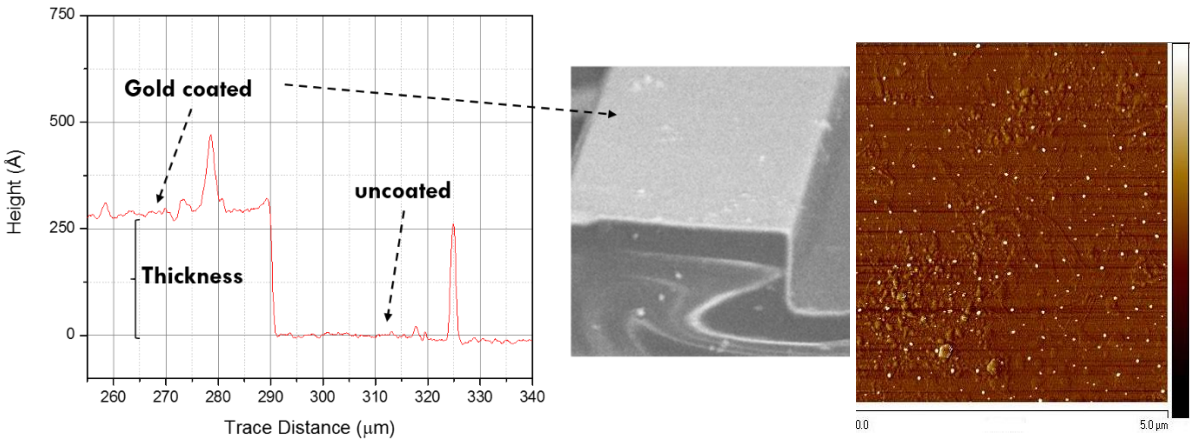

Fig. 29. Characterizing the metal thickness by surface profilometer (left) on a flat glass slide, and by SEM (middle), and characterizing the surface smoothness by AFM (right). After the characterization, the optical fiber is coated with the desired metal thickness.

Chapter 3 presents the first article presented during the PhD project. The article is on capturing the cladding modes in reflection and using the scheme as refractometer to measure the SRI

leading up to the TFBG-SPR sensor presented in chapter 4. The work presented in these articles shows the physical principles underlying different TFBG-SPR schemes behavior, their characterization and how they can be optimized.

CHAPTER 3 ARTICLE 1: CAPTURING REFLECTED CLADDING MODES FROM A FIBER BRAGG GRATING WITH A DOUBLE-CLAD FIBER COUPLER

Mohamad Diaa Baiad,[1,*] Mathieu Gagné,[2] Simon Lemire-Renaud,[3] Etienne De Montigny,[3] Wendy-Julie Madore,[3] Nicolas Godbout,[3] Caroline Boudoux,[3] and Raman Kashyap[1,2]

[1]Department of Electrical Engineering, École Polytechnique de Montréal, C.P. 6079, Succ. Centre-ville, Montréal H3C 3A7, QC, Canada

[2]Advanced Photonics Concepts Laboratory, Department of l Engineering Physics, École Polytechnique de Montréal, C.P. 6079, Succ. Centre-ville, Montréal H3C 3A7, QC, Canada

[3] Centre d'Optique, Photonique et Laser, Department of Engineering Physics, École Polytechnique de Montréal, C.P. 6079, Succ. Centre-ville, Montréal H3C 3A7, QC, Canada

Published in Optics Express on March 2013

OVERVIEW:

This paper demonstrates for the first time capturing the cladding modes with double-clad fiber coupler (DCFC) and how a surrounding refractive index (SRI) measurement can be made with high precision using an FBG. It is capable of being used remotely over a long distance. These results led to the subsequent article in chapter 4. This article contributes to show the potential in sensing of using the DCFC which is the first product of Castor Optics, a start-up launched recently by scientists from Polytechnique Montreal. The results of the article were presented at different meetings and international conferences like OECC 2013 in Kyoto of Japan, and WOFS in Warsaw, Poland.

The complete reference to the article:

M. Baiad, M. Gagné, S. Lemire-Renaud, E. De Montigny, W. Madore, N. Godbout, C. Boudoux, and R. Kashyap, "Capturing reflected cladding modes from a fiber Bragg grating with a double-clad fiber coupler," Opt. Express 21, 6873-6879 (2013).

3.1 Abstract

We present a novel measurement scheme using a double-clad fiber coupler (DCFC) and a fiber Bragg grating (FBG) to resolve cladding modes. Direct measurement of the optical spectra and power in the cladding modes is obtained through the use of a specially designed DCFC spliced to a highly reflective FBG written into slightly etched standard photosensitive single mode fiber to match the inner cladding diameter of the DCFC. The DCFC is made by tapering and fusing two double-clad fibers (DCF) together. The device is capable of capturing backward propagating low and high order cladding modes simply and efficiently. Also, we demonstrate the capability of such a device to measure the surrounding refractive index (SRI) with an extremely high sensitivity of 69.769 ± 0.035 μW/RIU and a resolution of $1.433\times10^{-5} \pm 8\times10^{-9}$ RIU between 1.37 and 1.45 RIU. The device provides a large SRI operating range from 1.30 to 1.45 RIU with sufficient discrimination for all individual captured cladding modes. The proposed scheme can be adapted to many different types of bend, temperature, refractive index and other evanescent wave based sensors.

3.2 Introduction

Cladding modes are guided modes which can be excited easily by scattering light from the core of an optical fiber into the cladding [33]. FBG excited cladding modes are traditionally observed as a series of resonance peaks on the short wavelength side of the transmission spectrum of an FBG [22], due to the limited overlap of the field of the cladding modes with the guided mode field and the refractive index change across the core. These modes can also be excited with high efficiency as seen in the spectrum of a tilted fiber Bragg grating (TFBG) [22]. These are generally not observed in the reflection spectrum since they may be dissipated through propagation along the high-index polymer jacket of the fiber [33]. Recently, many schemes have been proposed to re-couple the reflected cladding modes back into the core. For example, a sensor has been proposed to re-couple cladding modes into the core of a short fiber excited by tilted fiber Bragg grating (TFBG) in which the sensor fiber was spliced to misaligned fiber [35], [36]. The sensor was used to measure the ambient refractive index, as a bend and vibration sensor [35], [36]. Such SRI sensor provides a dynamic range from 1.33 to 1.45 with sensitivity of 1100 nW/RIU at 1.33.The re-coupled cladding modes are within the wavelength band of 1538 nm and 1551 nm as merged band with no discrimination between individual cladding modes [36]. Another scheme to re-couple low order cladding modes excited by the TFBG in the core used an abrupt bi-conical fused taper [37].

Cladding modes have also been re-coupled into the core with a TFBG in which a short multimode fiber or a thin-core fiber section with a mismatched core diameter section was spliced between a single mode fiber and the TFBG [38]. The recoupled cladding modes in the best-case scenario are within the wavelength band of 1541 nm and 1549 nm. The sensor was used to measure the differrent refractive indices of glycerine-water solutions surrounding the TFBG providing a dynamic range from 1.33 to 1.45 RIU.

A scheme to couple the cladding modes into the core using a hybrid long period grating (LPG) and an FBG device has also been demonstrated. Here, the forward propagating core mode is partially coupled by the LPG into a cladding mode, which in turn is reflected with the core mode by a subsequent FBG, and partially re-coupled into the core by the same LPG [39], [40].

One of the problems in all these devices is that, generally when a large number of cladding modes are involved, it is difficult to capture all the modes within a large wavelength band. An efficient discrimination between individual cladding modes is another problem to consider.

In this paper, we present a novel and simple device, which is capable of measuring cladding modes efficiently including both low-order, as well as higher order cladding modes propagating at steeper angles, which are more sensitive to the surrounding medium. We use the reflection from a single FBG in a standard photosensitive single mode fiber to couple the cladding modes into the inner cladding of a fusion spliced and diameter-matched DCF. The signal is viewed on the return port of a double-clad fibre coupler (DCFC).

3.3 Experimental procedure

The DCF has a single mode core, a lower index first cladding and a depressed outer cladding. Our device consists of a DCFC, whose single mode core is excited by a standard single mode fiber (SMF) spliced to one of its two branches and connected to a swept wavelength system (SWS) in a wavelength range between 1500 and 1560 nm (branch 1), and is schematically shown in Fig. 30. A single mode photosensitive fiber with an imprinted FBG is fusion spliced to the DCF a short distance away (~5 mm). The device is characterized by measuring the reflected core and cladding light through the DCFC (branch 2) on an oscilloscope.

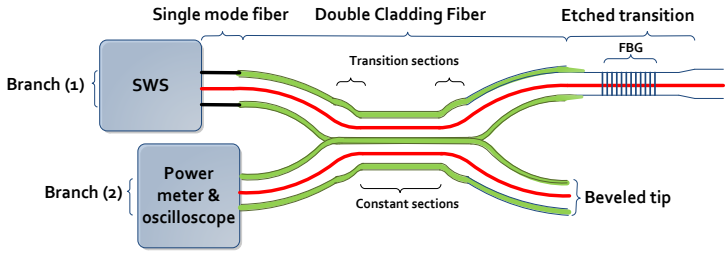

Fig. 30. Schematic of the proposed device to characterize the reflection spectrum.

The DCFC is made by fusing and tapering two DCFs [71]. The fibers are stripped of their protective jacket, cleaned, installed and inspected on a custom-made fiber coupler fabrication station. As a first step, the fibers are fused at high temperature using an oxy-propane micro-torch. The torch, mounted on a three-axis motorized stage, moves back and forth along the fibers to control the fusion length. As a second step, both ends of the structures are pulled apart using two additional motorized stages moving at a speed of 50 µm/s. The optical response is measured in real-time during fabrication. The DCF (Nufern, East Granby, CT, SM-9/105/125-20A) has a core diameter of 9 µm, an inner cladding diameter of 105 µm and fluorine-doped outer cladding diameter of 125µm of lower refractive index. The numerical aperture (NA) of the single mode core of the DCF is 0.12 and the inner cladding NA is 0.20. Our optical spectrum analyzer could accommodate a maximum light guiding diameter of only 62 micron and was therefore insufficient for the 105 micron inner cladding diameter in our experiments. We therefore used an integrating sphere power meter which has an entrance slit of 2.2 mm connected to the DCFC. The back reflected cladding modes are collected at the splice between the photosensitive fiber and the DCF by the inner cladding of the DCF and routed to the power meter by the second branch of the DCFC (see Fig. 30).

The FBG was imprinted in a photosensitive fiber by a commercially available 224 nm Nd:YVO_4 laser which produces pulses of 7 ns an energy of 30 µJ at a repetition frequency of between 0.1 and 30 kHz with a maximum average power of 300 mW (Xiton Photonics). The beam is about 1 mm in diameter and is slightly elliptical. This laser has an excellent beam profile and stable laser output. It has a high wall-plug efficiency compared to the Argon laser used in the past for FBG fabrication [69]. A mirror on a linear translation stage was used to scan the fiber, and a 20 cm cylindrical lens is used to focus the light. A Bragg wavelength at 1554.5 nm was imprinted with a length of 12 mm.

3.4 Results and Discussion

Fig. 31 shows the transmission and the reflection spectra in the proposed scheme normalized with respect to the transmitted power at 1560 nm. The transmission spectra consist of two bands, a strong Bragg resonance at 1554.5 nm and several narrow resonances, which are the cladding modes on the short wavelength side of the Bragg resonance. The cladding mode resonances begin at a wavelength of 1547 nm and consist of relatively strong low order modes, which are more confined and propagate at low angles. It can be seen that the reflection spectra of the cladding modes consist of modes within a wavelength band from 1543 nm to 1547 nm, which complements a limited sub-set of the cladding mode resonances seen in the transmission spectra.

Characterisation of the coupler response is shown in Fig. 32. These experiments were conducted by exciting the port where the FBG was situated but without the FBG in place. The DCFC was designed to act as a null coupler for the core mode and as an 50:50 coupler for the inner cladding modes from 1265 to 1325 nm [71]. At 1555 nm, the measured power in the core mode in the second branch where the reflected light from the DCFC is measured reaches ~ -11.5 dB including the 10.5 dB coupler loss (see Fig. 32). The characterization of the spectral response of the DCFC core transmission is achieved with a conventional broadband source and an optical spectrum analyzer. In addition, the splice loss between the SMF28 and the DCF is ~ 1 dB.

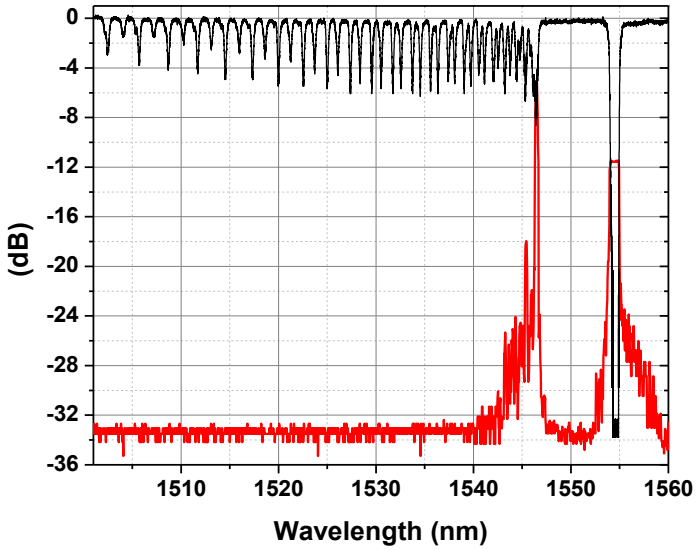

Fig. 31. The transmission and reflection spectra of the proposed scheme before etching of the DCF.

The reflected power in the lowest order cladding mode is ~ -5.3 dB since the maximum value for transmission by inner cladding modes is 33.5% in the second branch of the DCFC coupler between 1500 nm and 1547 nm (see Fig. 32). The characterization of the spectral response of the DCFC inner cladding transmission is achieved by using a wavelength-swept source and a diffuser. The diffuser is used to excite the high and low order modes in the inner cladding of the DCF [71].

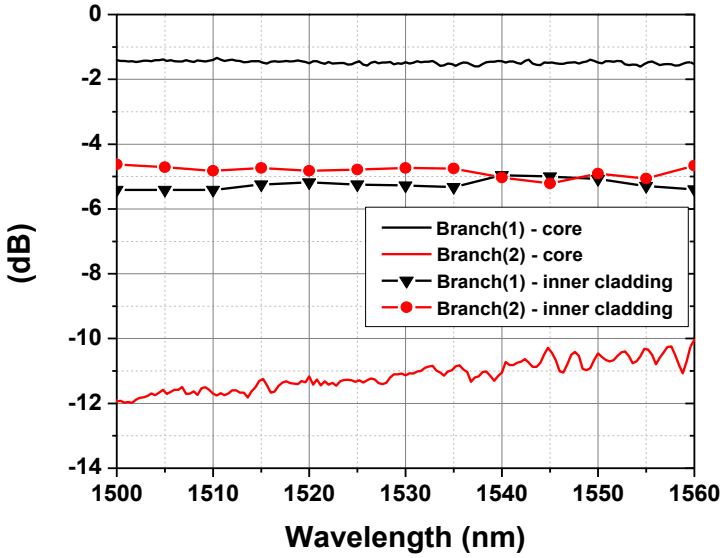

Fig. 32. Spectral response of the DCFC core transmission and the inner cladding transmission.

In order to improve the efficiency of our device to capture greater number of the back reflected cladding modes at the splice between the FBG photosensitive fiber and the inner cladding of the DCF, the cladding diameter of the photosensitive SMF and the inner cladding diameter of the DCF have to be matched by decreasing the SMF diameter by 20 μm. This is achieved by etching the SMF, removing 20 μm of the cladding. In our scheme, the etched transition region (see Fig. 30) consists of the FBG in the photosensitive SMF and a small part of the DCF. To ensure better wet etch uniformity, a buffered oxide etch (BOE) [diluted HF with ammonium fluoride (NH_4F)] is used to slow down the etch rate of SiO_2 and to promote more uniform etching of the glass surface. The dilution ratio used in our experiment was 7:1 NH_4F:HF. The reflection spectra in Fig. 33 show that decreasing the diameter by 20 μm increases the captured higher order modes significantly and increases the power of the captured low order modes as well.

Fig. 34 shows both the reflection and transmission spectra of the device after HF wet etching. It can be seen that both low and high order modes, which are excited by the FBG can be recaptured

efficiently by the proposed scheme. The captured cladding modes are within the wavelength band of 1500 nm and 1547 nm. Low order modes are captured very effectively, and the weakest high order mode are also well resolved and exceed 8 dB above the noise level, which can therefore be used in sensing. The different individual cladding modes can be easily discriminated and tracked.

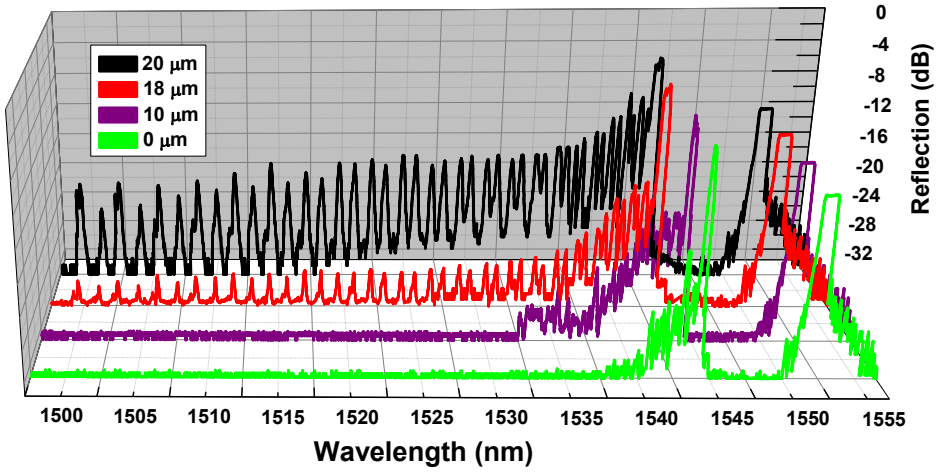

Fig. 33. The reflection spectra of the proposed scheme with the fiber diameter decreased by 10, 18 and 20 ± 0.2 μm by wet etching.

Although the coupling loss of the DCFC increases with higher order cladding modes, there is sufficient discrimination even for the 41st cladding mode, to be used for sensing (see Fig. 34). The reflected power in the highest order cladding modes shown in Fig. 30 should ideally reach -12 to -14 dB including the 4.8 dB coupler loss. However, the splice loss between the SMF and the DCF of ~1 dB needs to be optimised, as this affects higher order modes more severely than lower order modes.

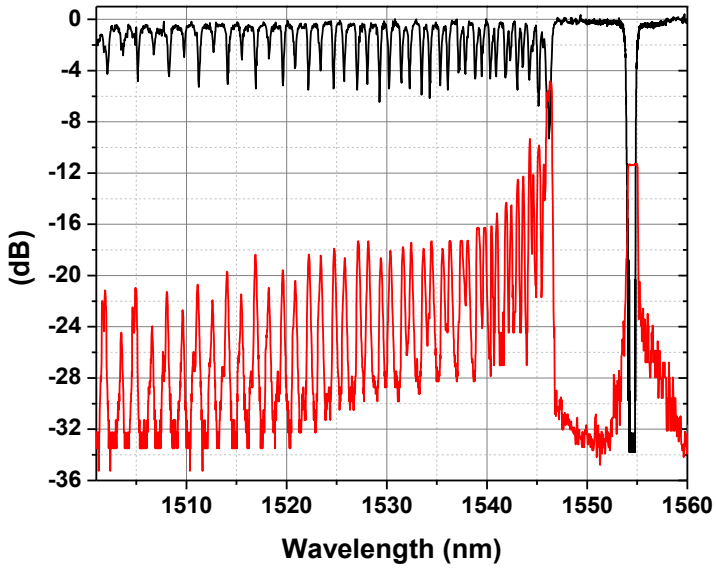

Fig. 34. The reflection (red curve) and the transmission (black curve) spectra of the proposed device after wet etching by 20 μm.

To demonstrate that the proposed scheme can be adapted as an evanescent wave based sensor, we characterize the response of the device to different surrounding refractive index (SRI) liquids from 1.30 to 1.51 (Cargille refractive index matching liquids).

Fig. 35 shows the reflection spectra in response to different SRI. It can be seen that for SRI of 1.30, all the higher order modes can be discriminated and few high cladding modes are affected giving a spectra similar to that shown in Fig. 34 where the SRI is air. Increasing the SRI affects the higher order modes which disappear first, followed by the more confined cladding modes until all the cladding modes including the low order modes disappear at an SRI of 1.51. As the SRI gradually approaches and then exceeds the effective refractive indices of the cladding modes, they can no longer exist as bound modes and hence the high order modes are attenuated first. As is obvious, monitoring the Bragg reflection simultaneously allows self-referencing of the ambient temperature during measurements.

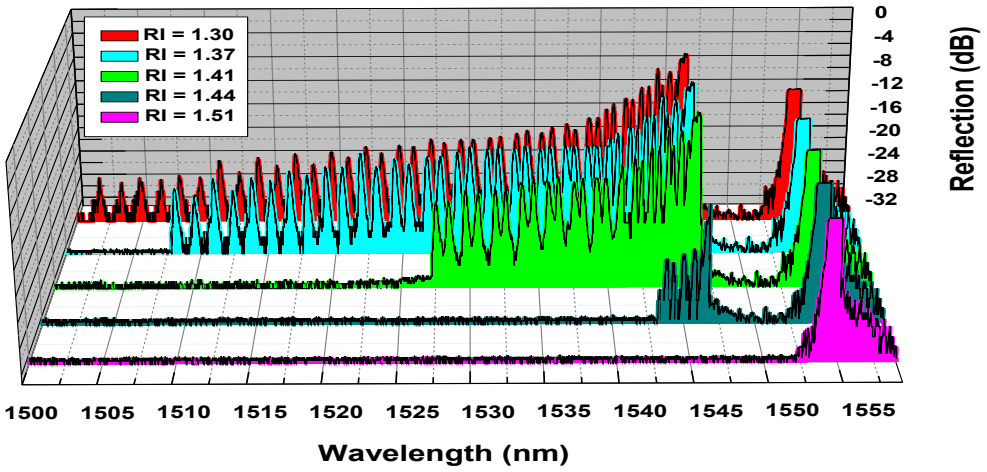

Fig. 35. The reflection spectra of the optimised device (20 micron etch) in response to different SRI.

The disappearing individual cladding modes can be easily discriminated and tracked by increasing the SRI between 1.37 and 1.45, indicating that the device can be used to determine the change in SRI by tracking the number of the attenuated cladding modes, as can be seen in Fig.36. For example, by increasing the RI from 1.37 to 1.39, six cladding modes disappear and by increasing the RI further to 1.41, 10 more cladding modes disappear until almost all the cladding modes vanish when the SRI is >1.45. The disappearance of the reflected cladding modes was fitted to a straight line using linear regression between 1.37 and 1.45 showing a step of ~ 2.15×10^{-3} RIU/ mode lost.

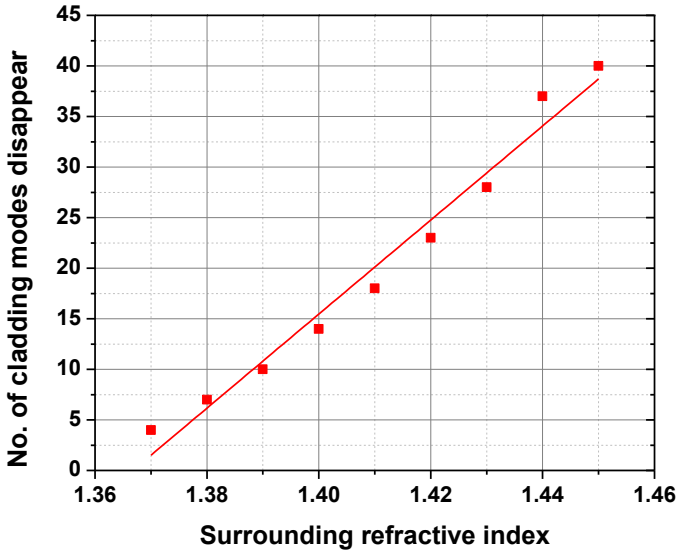

Fig.36. Dependence between the number of cladding modes disappear on increasing the SRIs from 1.37 to 1.45 RIU.

Fig. 37 shows another technique for measuring the SRI. Here, the reflected power of the proposed device is averaged over all the cladding modes. The cladding power decreases with increasing refractive index, indicating that the device can be used to determine the change in SRI by measuring the total cladding power reflected, noting that the Bragg reflection power remains unchanged with changing SRI. The power in the reflected Bragg wavelength was measured from 1552.5 nm to 1560 nm, while the cladding power was measured from 1500 nm to 1547.5 nm. Also, the reflected cladding power was fitted to 2 straight lines using linear regression between 1.30 and 1.37 and between 1.37 and 1.45, where it can be seen that there is a larger decrease in the cladding and total power between the SRIs compared with the lower SRIs in the range 1.30 and 1.37. The effective RIs of the high power containing lower order cladding modes lie between SRIs of 1.37 to 1.45. By matching the SRI with their effective refractive indices, the relevant modes disappear and hence the cladding or total power drops significantly. Between 1.45 and 1.51, it can be seen that the cladding power decrease is relatively small since almost all the cladding modes have vanished as they are no longer guided.

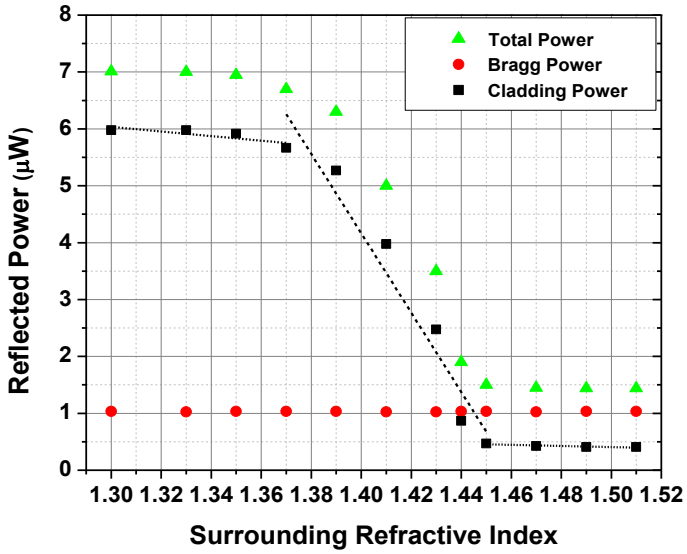

Fig. 37**.** Distribution of the reflected power with different SRI.

With this experimental scheme used in our measurements, the device shows a maximum sensitivity of 69.769 ± 0.035 μW/RIU between SRIs of 1.37 and 1.45 with a maximum standard deviation of 0.035 μW in response to different SRI measurements. The device shows minimum sensitivity of 4.043 μW/RIU between RIs of 1.30 and 1.37 indicating that the device is sensitive to RI changes down to 1.30 and providing a large dynamic range of SRI from 1.30 to 1.45. The device has high resolution for the higher sensitivity regime equivalent to an SRI change of 1.433×10^{-5} RIU ± 8×10^{-9} RIU, assuming an optical power meter with measurement resolution of 1 nW.

Finally, we note that the entire device could be simplified, by being fabricated in DCF fibre alone, including the FBG, so that no splicing of the FBG would be necessary. Only the FBG region would have to be etched so that the inner cladding could be exposed to the SRI for sensing. This would ensure minimum loss of the device. Furthermore, the DCFC fabrication process for the coupler can be optimised to ensure lower coupling loss for the high order modes and to improve the isolation between the cores of the DCFs. Work is under way to make this improvement, and the results will be reported elsewhere. Also, we note that the DCF coupler may also be used as an effective device to capture forward propagating cladding-modes excited by a long period grating (LPG), when used at the output.

3.5 Conclusion

In conclusion, an experimental scheme for a simple and novel device to recapture efficiently a large number of discriminated cladding modes in reflection from a fiber Bragg grating with a double clad fiber coupler has been proposed and demonstrated. The coupler is made by fusing and tapering two double clad fibers. Etching the single mode fiber with a Bragg grating inscribed in the core increases the efficiency of capturing the high order cladding modes. Using the scheme, low and high order cladding modes within a wavelength band from 1500 nm and 1547 nm can be captured with sufficient efficiency for the modes to be used in sensing. We have demonstrated this device for SRI sensing. The device shows a maximum sensitivity to SRI of 69.769 ± 0.035 μW/RIU and a resolution of $1.433\times10^{-5} \pm 8\times10^{-9}$ RIU between 1.37 and 1.45. The device has a large dynamic range to operate from 1.30 and 1.45. In addition, we have demonstrated a new method in which the individual cladding mode peaks can be used to measure the SRI in a stepped fashion with a sensitivity of ~ 2.15×10^{-3} RIU per mode. We anticipate that this device will have many applications for evanescent wave sensing systems.

CHAPTER 4 ARTICLE 2: SURFACE PLASMON RESONANCE SENSOR INTERROGATION WITH A DOUBLE-CLAD FIBER COUPLER AND CLADDING MODES EXCITED BY A TILTED FIBER BRAGG GRATING

Mohamad Diaa Baiad,[1,*] Mathieu Gagné,[2] Wendy-Julie Madore,[2] Etienne De Montigny,[2] Nicolas Godbout,[2] Caroline Boudoux,[2] and Raman Kashyap[1,2]

[1]Department of Electrical Engineering, École Polytechnique Montréal, C.P. 6079, Succ. Centre-ville, Montréal H3C 3A7, QC, Canada

[2]Department of Engineering Physics, École Polytechnique Montréal, C.P. 6079, Succ. Centre-ville, Montréal H3C 3A7, QC, Canada

Published in Optics Letters on November 2013

OVERVIEW:

This paper demonstrates the potential of using captured cladding modes in reflection for SPR sensing for the first time. The results of this article demonstrate the improvement of the sensor operating range and shows better discrimination of cladding and SPR coupling compared to the standard interrogation method of SPR-TFBG sensors using the transmission spectrum. The published article was selected for inclusion in Spotlight on Optics where feature articles are nominated to show the breadth and quality of the Optical Society of America's (OSA) content. The journal editors identify articles for Spotlight that have excellent scientific quality creating also the potential for dialogue between author and reader. The article results were presented at different meetings and international conferences like the SPIE Conference, Photonics West, 2014 in San Francisco, and SPP6 2013 in Ottawa.

The complete reference to the article:

M. D. Baiad, M. Gagné, W.-J. Madore, E. De Montigny, N. Godbout, C. Boudoux, and R. Kashyap, “Surface plasmon resonance sensor interrogation with a double-clad fiber coupler and cladding modes excited by a tilted fiber Bragg grating,” *Opt. Lett.*, vol. 38, no. 22, pp. 4911–4914, Nov. 2013.

4.1 Abstract

We present a novel optical fiber surface Plasmon resonance (SPR) sensor scheme using reflected guided cladding modes captured by a double-clad fiber coupler, and excited in a gold-coated fiber with a tilted Bragg grating. This new interrogation approach, based on the reflection spectrum provides an improvement in the operating range of the device over previous techniques. The device allows detection of SPR in the reflected guided cladding modes and also in the transmitted spectrum, allowing comparison with standard techniques. The sensor has a large operating range from 1.335 to 1.432 RIU, and a sensitivity of 510.5 nm/RIU. The device shows strong dependence on the polarization state of the guided core mode which can be used to turn the SPR on or off.

4.2 Introduction

Recently, many surface Plasmon resonance (SPR) sensors have been proposed using the excitation of an SPR by tilted fiber Bragg gratings in gold-coated waveguides and fibers. Shevchenko *et al.* [32] observed experimentally the SPR modifying the cladding mode transmission spectrum by using tilted fiber Bragg gratings (TFBG) at a small angle ranging from 2 to 10 degrees. The sensitivity of such a sensor was reported to be 456 nm/RIU for a limited surrounding refractive index (SRI) operating range of between 1.42 and 1.45 RIU. The full width half maximum (FWHM) spectral width of the SPR localization in the observed cladding modes was 5 nm [32].

Spackova and Homola have proposed theoretically a multi-channel single-mode fiber (SMF) optic SPR sensor based on coupling of the forward-propagating core mode into the counter-propagating mixed SPR-cladding modes by a fiber Bragg grating (FBG) [24]. Such a sensor provides a sensitivity of 200 nm/RIU and a FWHM of 0.25 nm [24]. Caucheteur proposed an experimental TFBG-SPR on a gold-coated SMF sensor using different properties such as the polarization dependent loss and the first Stokes parameter [46]. Such a sensor provides a sensitivity of 673 nm/RIU, again for a limited SRI range between 1.31 and 1.38 RIU with a FWHM of the SPR envelope of 5 nm. Holmes has proposed an experimental planar-integrated SPR-TFBG sensor [42] which operates by coupling the core mode of a planar waveguide to a set of hybrid Plasmon-dielectric modes. The proposed device yields a maximum predicted sensitivity of 567 nm/RIU.

One of the characteristics of all these devices [24], [32], [42], [46] is that the cladding modes are not collected since they may be dissipated through propagation along the high-index polymer jacket of the fiber. Hence, the SPR is usually observed through the transmission spectrum alone. Also, the transmission spectrum has weak cladding resonances for the low-order cladding modes which limits the operating range of the device. Additionally, sensors operating in transmission require that the grating itself be coated in gold. Chan and Albert have demonstrated the transmission spectrum of TFBG reflected from a cleaved fiber end-facet coated with gold for sensing [49] where the measured spectrum represents the interference between the reflection spectrum and the transmission spectrum seen reflected from the fiber end.

In this Letter, we present a simple but novel SPR device using a double-clad fiber coupler (DCFC) and a TFBG in a standard photosensitive SMF. The device efficiently measures the spectrum of the SPR-modified reflected cladding modes as well as that of the transmitted core mode.

4.3 Experimental procedure

Fig. 38 shows a schematic of our device. It consists of a DCFC fabricated by fusing and tapering two double-clad fibers (DCFs) [71], [72]. The DCF's single-mode core is excited by a SMF spliced to branch (1) and connected to a broadband source (BBS) in a wavelength range between 1525 and 1590 nm. The DCF has a single-mode core of 9 μm diameter, a lower index first cladding of 105 μm diameter and a depressed outer cladding of 125 μm diameter. The light from the broadband source passes through an in-line polarizer. A polarization controller (PC) configured as a half-wave plate is

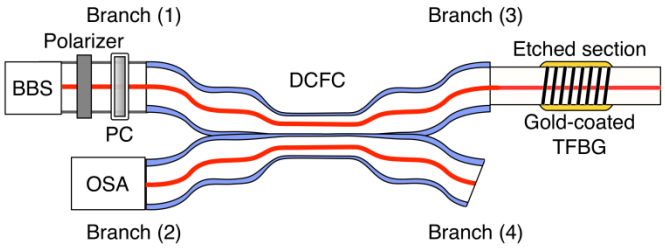

Fig. 38. Schematic diagram of the proposed SPR sensor. Light from a broad band source (BBS) is coupled to a gold-coated tilted fiber Bragg grating (TFBG) through the core of a double-clad fiber coupler (DCFC). Reflected cladding modes are collected at branch (2) of the DCFC and characterized by the optical spectrum analyzer (OSA).

used to rotate and adjust the polarization state of the light reaching the DCFC and the TFBG. The end of branch (4) was immersed in index matching oil in order to ensure that the end-facet Fresnel reflection from the transmitted TFBG spectrum does not interfere with the spectrum detected at branch (2).

A 6° TFBG with a nominally nulled core reflection centered at 1586 nm and a length of 2 cm is written into a photosensitive boron/germanium (B/Ge) doped fiber (Redfern, Eveleigh, NSW, Australia) to excite cladding modes efficiently. This fiber is etched using hydrofluoric acid to a diameter of 105 μm to match the diameter of the inner cladding of the DCF. The TFBG is imprinted in the photosensitive fiber by a commercially available 266 nm solid-state nanosecond Q-switched frequency quadrupled yttrium lithium fluoride (YLF) laser, using a scanning phase mask technique [73]. A mirror mounted on a linear translation stage scans the laser which is focused on the fiber through a 20 cm focal length cylindrical lens. In order to fabricate the tilted gratings, the phase mask itself was rotated by 6° relative to the propagation axis of the fiber [22].

A 2 nm thin film of chromium and 30 nm of gold are deposited on the 2 cm long TFBG by sputtering, rotating the fiber by 180° in two exposures. The device is characterized by collecting the back-reflected cladding modes through the inner cladding of the DCF. An OSA at branch (2) records the reflected spectrum (Fig. 38). The transmission spectrum is also characterized by connecting the OSA at the end of branch (3).

4.4 Results and Discussion

The transmission and the reflection spectra from the gold-coated TFBG immersed in air are shown in Fig. 39. The transmission spectrum consists of two bands: a weak core mode resonance at 1586 nm (nominally nulled) and a set of resonances from the cladding modes on the short wavelength side of the core resonance. Cladding mode resonances begin at a wavelength of 1584 nm and consist of relatively weak and almost invisible low-order cladding modes between 1584 and 1574 nm as well as many high-order cladding modes. The core reflection serves as a reference peak at a wavelength insensitive to the surrounding refractive index. The reflection spectrum consists of a strong core mode peak and several cladding modes. The visibility of the reflected spectrum peaks is much higher than that of the transmitted counterparts, and enables the observation of lower order cladding modes which can be used for SPR sensing.

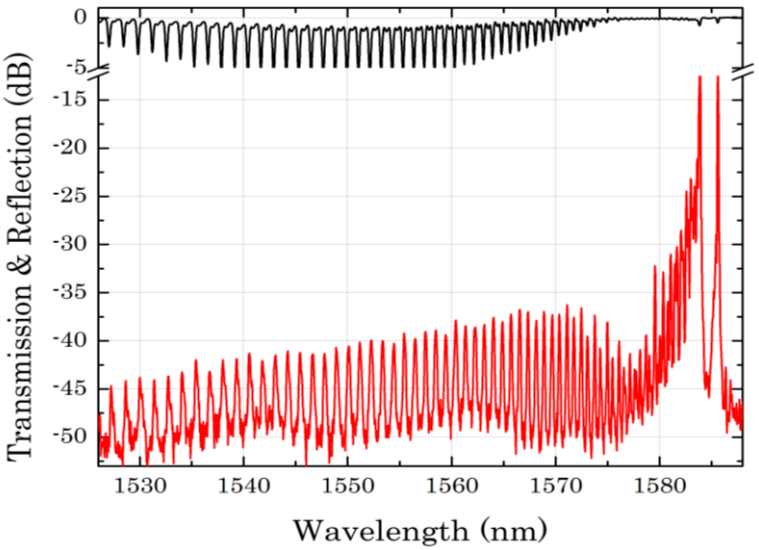

Fig. 39. Transmission of the core mode (black) and reflection of the core and cladding modes (red) spectra from the gold-coated 6° TFBG when the device is in air.

Some of the excited cladding modes couple to the SPR and are dissipated in the metal if the phase matching (PM) condition is satisfied. This happens when the effective refractive index of cladding modes is close to that of the SPR, as determined by the SRI. According to a geometrical optics picture, each cladding mode represents an optical ray striking the cladding-metal boundary at some angle of incidence. Fig. 40 shows results from a numerical simulation estimating the reflectance with respect to the incidence angle in the Kretschmann configuration using the matrix method for 4 layers including the cladding, chromium, gold, and the SRI at 1550 nm.

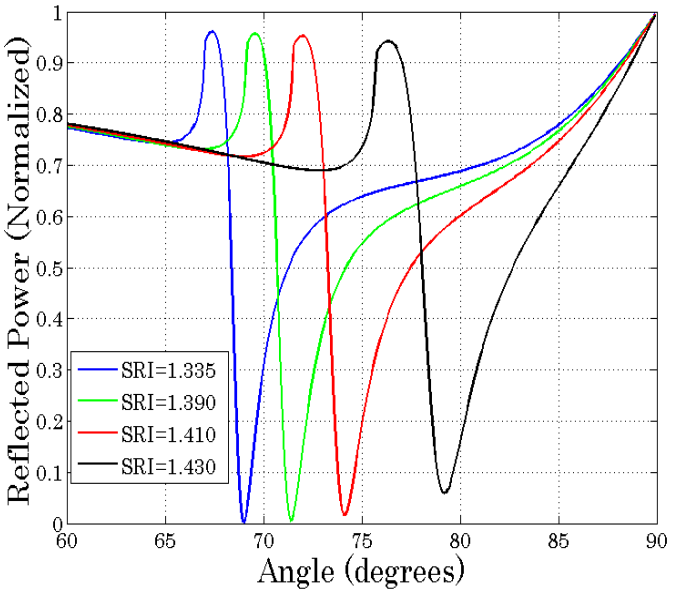

Fig. 40. The calculated reflectance with respect to the incidence angle for 4 surrounding refractive index (SRI) values at 1550 nm.

The calculated resonant angle determines the strongest coupling to the SPR and hence the SPR's existence. At the resonant angle the PM condition is satisfied [74]. In general, The PM condition can be expressed as

$$n_{cl}\sin(\theta_{cl}) = \mathrm{Re}\left(\sqrt{\frac{\varepsilon_m \times \varepsilon_d}{\varepsilon_m + \varepsilon_d}}\right) \tag{4-1}$$

where ε_m being the dielectric constant of the metal , ε_d is the dielectric constant of the sensing medium around the metal, n_{cl} is the cladding refractive index, and θ_{cl} is the angle of the cladding mode ray incident on the cladding-metal interface.

The effective refractive index of a cladding mode can be calculated from the resonant condition of the TFBG by [22]

$$n_{cl}^{eff} = \frac{\lambda_{cl} \times \cos(\theta)}{\Lambda} - n_{eff} \tag{4-2}$$

where θ is the tilt angle with respect to the plane of the propagation axis in the fiber, Λ is the grating period, and n_{eff} is the effective refractive index of the core mode at the resonant wavelength (λ_{cl}). Fig. 41. shows the calculated SPR resonance angle as a function of the SRI. The

incident angles increase as the SRI increases corresponding to steeper incident angles of the high-order cladding modes.

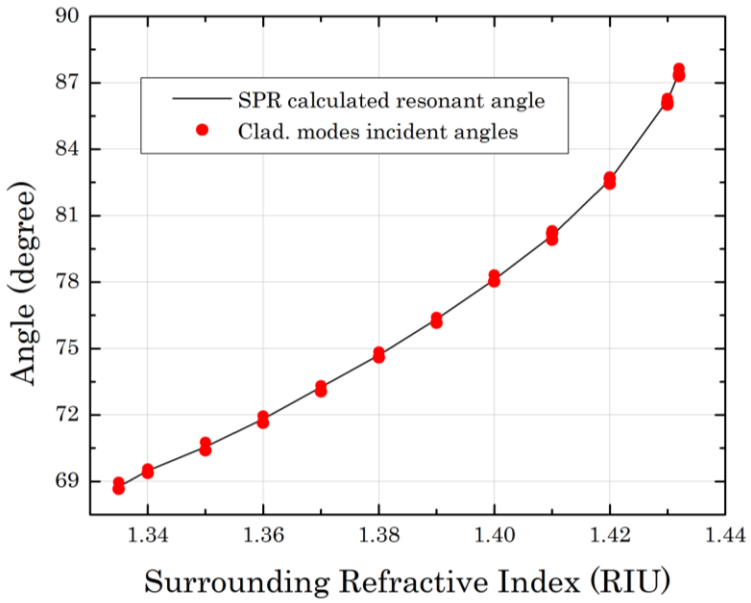

Fig. 41. Dependence of the resonant SPR and the cladding modes incident angles on the SRI for the 4 layers structure. For each SRI data point, two or more cladding modes get affected and match the PM condition.

The amplitude of the affected cladding modes decrease significantly at the PM wavelength. Fig. 42 shows the spectra obtained with the SPR-TFBG sensor with different SRI liquids. Changing the SRI tunes the SPR wavelength. The SPR shifts towards longer wavelengths as the PM condition changes with the SRI increasing. As shown in Fig. 42 , the reflection spectra provide better discrimination of the SPR with more than 8 dB of extinction ratio as well as an improved operating range at high values of the SRI, e.g. at an SRI of 1.43. On the other hand, the SPR signature is invisible in transmission because of the weak coupling to the low-order cladding modes. The FWHM of the SPR excitation signature is 4 nm maximum. A few cladding modes whose incident angles are close to the SPR resonance angle satisfy the PM condition and couple to the SPR. This makes the SPR location broader than expected. The two-step gold deposition approach which resulted in non-uniform gold deposition around the fiber makes the FWHM of the SPR wider as well, due to position dependent gold thickness [75].

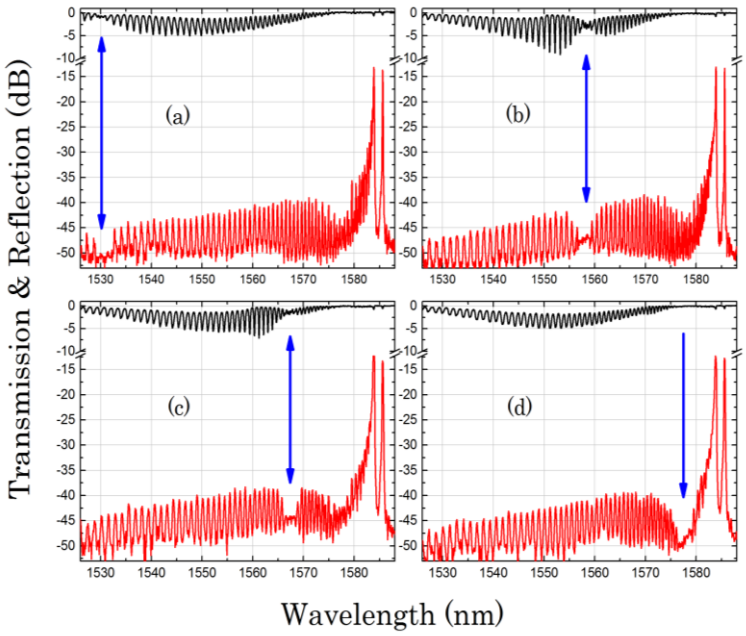

Fig. 42**.** SPR excitation and shift in transmission (black) and in reflection (red) with wavelength as a function of the surrounding refractive index (SRI) (a) SRI = 1.335 RIU (b) SRI = 1.390 RIU (c) SRI = 1.410 RIU (d) SRI = 1.430 RIU. Arrows indicates the SPR signature.

In addition to satisfying the PM condition, coupling to the SPR needs the polarization state of the cladding modes to be matched to the SPR, since only the *p*-polarisation state is allowed (SPR only couples to one polarisation only). Controlling the polarization state is therefore crucial for our sensor [76]; rotating the linearly polarised light in branch (1) by 90° relative to the grating tilt plane using a half-wave plate turns the SPR coupling from the "on" (*p*-polarised mode) to the "off" (*s*-polarised mode) state. In the case of the *p*-polarised mode, the electric fields of the cladding modes are polarized radially at the cladding interface [41].

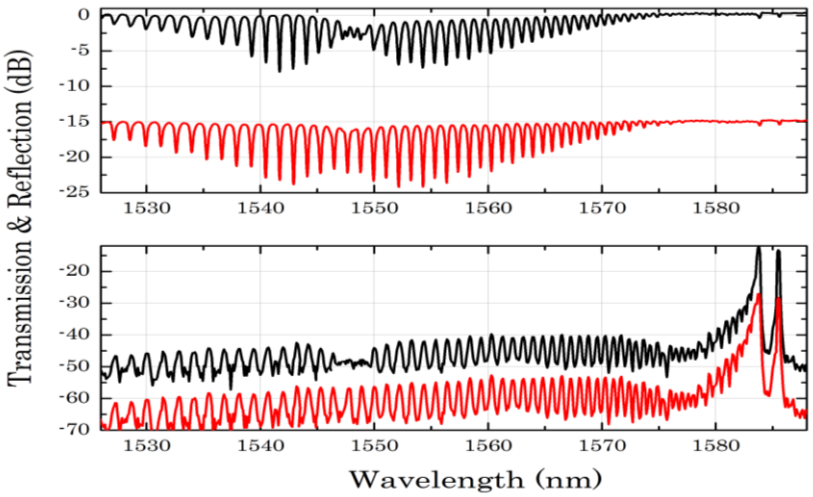

Fig. 43. Transmission (top) and reflection (bottom) spectra of two orthogonal linear states in surrounding refractive index (SRI) =1.370 to turn the SPR on (black) and off (red-offset by 15 dB).

In the case of the *s*-polarised mode, the electric fields of the cladding modes are polarized azimuthally at the cladding interface. Fig. 43 shows that TFBG-assisted excitation of the SPR in both reflection and transmission depends strongly on the state of polarization of the fundamental core mode. Several techniques have been proposed to improve the resolution and the performance of the SPR-TFBG sensor in transmission based on tracking individual cladding mode resonances and their dependence on the state of polarization (SOP) [43], [44], or using different properties such as the first Stokes parameter and the polarization dependent loss [46]. These techniques are also fully applicable to our proposed configuration and should improve the sensor's resolution.

Fig. 44 shows a linear dependence of the SPR as a function of the SRI. The slope demonstrates a sensitivity of 510.5 nm/RIU. By considering the midpoint between the two adjacent cladding resonance peaks close to the SPR envelope as the central SPR wavelength, we have ascertained that these results are repeatable with a maximum error of ± 0.035 nm/RIU. This technique helps in reducing the error of our sensor and hence improving the resolution to ≈ 6.8 x 10^{-5} RIU with the OSA used in our setup. The sensor provides a significantly wider operating range between 1.335 and 1.430 RIU using the reflection spectrum, compared to those reported in literature [24], [32], [42], [46]. By simply increasing the tilt angle, stronger coupling occurs to cladding modes of lower effective indices than 1.335. Hence increasing the dynamic range for SPR sensing.

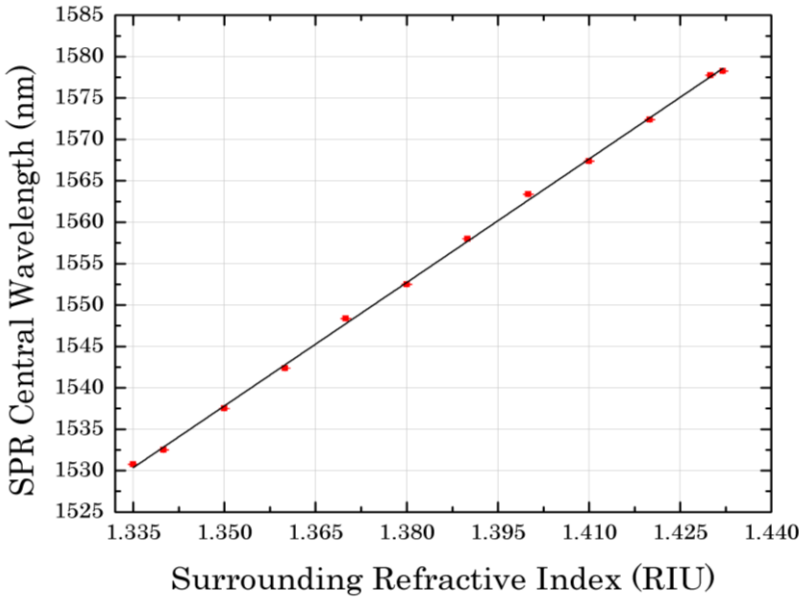

Fig. 44. Shift of the SPR wavelength as a function of the surrounding refractive index SRI.

Finally, since the cladding modes are captured and guided through the DCF, the entire device can be simplified. This can be achieved by coating any part of the DCF with gold after etching off the outer cladding completely instead of coating the TFBG itself. Only a part of the DCF region has to be etched so that the inner cladding is exposed to the SRI for sensing. This approach allows the construction of a sensor with reduced complexity since it provides a larger and more flexible sensing area along the etched and gold-coated DCF. In addition, it keeps the grating unmodified and safe. This configuration can also be adapted for development of novel multi-channel SPR fiber optic probes. Work is under way to make this improvement, and the results will be reported elsewhere.

4.5 Conclusion

In conclusion, a novel gold-coated fiber SPR sensor using cladding modes generated by a TFBG and captured by a DCFC has been experimentally demonstrated. The existence of the SPR excited in gold-coated TFBG in both the reflected guided cladding modes and its transmitted core mode have been shown. The device's response is strongly dependent on the polarization state guided core mode, turning the SPR entirely on or off. The sensor has a sensitivity of 510.5 nm/RIU, and a wide SRI operating range from 1.335 to 1.432 RIU, larger than any reported in the literature. Using the SPR-TFBG in reflection with sufficient discrimination of all

individual captured cladding modes allows the extended SRI range. The added convenience of observing both the transmitted and reflected spectra simultaneously, makes this sensor especially easy to use.

CHAPTER 5 ARTICLE 3: CONCATENATION OF SURFACE PLASMON RESONANCE SENSORS IN A SINGLE OPTICAL FIBER USING TILTED FIBER BRAGG GRATINGS

Mohamad Diaa Baiad,[1,*] and Raman Kashyap[1,2]

The Fabulas Laboratory

[1]*Department of Electrical Engineering, École Polytechnique Montréal,*

C.P. 6079, Succ. Centre-ville, Montréal H3C 3A7, QC, Canada

[2]Department of Engineering Physics, École Polytechnique Montréal,

C.P. 6079, Succ. Centre-ville, Montréal H3C 3A7, QC, Canada

Accepted for publication in Optics Letters on October 2014

OVERVIEW:

This paper demonstrates for the first time the multiplexing of a number of SPR-TFBG sensors in a single optical fiber for simultaneous multi-analysis purposes and how the characteristics of such sensors can be engineered easily using a scanning phase mask interferometer technique to write the TFBGs. This article also shows the potential of using the interferometer from PhotoNova Inc., Montreal, Canada, in writing TFBGs and in its evaluation of the product. The article results were presented at different meetings and international conferences like CIOFF 2014 (Plenary) in Havana of Cuba, and LAOP 2014 (Tutorial) in Cancun, Mexico. These results contribute to the subsequent articles in chapter 6.

The complete reference to the article:

M. D. Baiad, and R. Kashyap, " Concatenation of surface Plasmon resonance sensors in a single optical fiber using tilted fiber Bragg gratings," accepted for publication in *Opt. Letters*, Oct. Nov. 2014.

5.1 Abstract

An in-line multichannel surface Plasmon resonance (SPR) sensor scheme excited with tilted fiber Bragg gratings (TFBG) in a chromium and gold-coated fiber is demonstrated. The channels have different operating wavelengths, different TFBG tilt angles, and hence different refractive index

operating ranges. The polarization state of each channel based on the TFBG orientation can be used to switch each SPR sensor on or off as required. This system provides an operating range from 1.40 to 1.44 RIU, and a sensitivity of around 500 nm/RIU. The multiplexing in a single optical fiber of a number of TFBG-SPR sensors is demonstrated for the first time.

5.2 Introduction

Tilted fiber Bragg gratings (TFBG) couple the forward Bragg core mode to the backward propagating cladding modes which can be observed as a series of resonance dips on the short wavelength side of the transmission spectrum [22]. These modes can be excited efficiently with different tilt angles relative to the propagation axis of the fiber [22]. By simply increasing the tilt angle, stronger coupling occurs to cladding modes of relatively lower effective indices and vice versa [22]. The cladding modes excited by the TFBG incident on the cladding metal interface transfer their power to the SPR at a resonant wavelength, by evanescent field coupling [15].

A variety of schemes and devices have been proposed to exploit surface Plasmon resonance (SPR) on metal dielectric interfaces using TFBG. Chen and Caucheteur experimentally demonstrated a TFBG-SPR scheme on a single mode fiber (SMF) coated with 2.6 μm low-index polymer of Cytop and 50 nm of gold [47]. The sensor showed both, long range SPR (LRSPR) and short range SPR (SRSPR) coupled modes over the wavelength range from 1525 to 1610 nm. Their scheme achieved an experimental sensitivity of 115 nm/RIU attributed to the LRSPR coupling and 68 nm/RIU to the SRSPR when the SRI was 1.3335. The sensitivity varied based on the SRI to reach a maximum of 186 nm/RIU between 1.31 and 1.35 RIU [47].

A multi-channel single-mode fiber (SMF) SPR sensor scheme using fiber Bragg gratings (FBG) has been proposed theoretically [24]. Here, the multichannel is achieved by a sequence of FBGs of different periods where the forward propagating core mode is partially coupled to backward travelling cladding modes. The sensor provided a calculated sensitivity of 200 nm/RIU between 1.32 and 1.325 RIU [24]. However, this approach requires very strong gratings to be inscribed and should be used with apodized FBGs for a clear SP resonance signature.

Albert *et al.* [50] have demonstrated a TFBG-SPR biochemical sensor in SMF coated with 30-50 nm of gold functionalized with aptamer receptor molecules. The sensor can act as a stand-alone device or as a multi-sensor platform. They proposed a multiplexing scheme based on multi-fiber

sensing devices in which each individual fiber represented one channel of the multiplexed system [50].

We have previously proposed a TFBG-SPR sensor using reflected guided cladding modes captured by a double-clad fiber coupler, and excited on a chromium and gold-coated fiber. The device allows detection of the SPR in both the reflection and transmission spectra [59].

In this Letter, we demonstrate that concatenation of SPR sensors is easily implemented using distributed in-line TFBGs in a *single* optical fiber. This scheme allows the sensing of different analytes by positioning in-line TFBGs with different tilt angles in which the wavelength operating range, the SRI range, and the polarization sensitivity of each channel can be engineered as required.

5.3 Experimental Procedure

Fig. 45 shows a schematic of the proposed device. It consists of a super-continuum laser source (broad-band source) which was used for a wavelength range between 1500 and 1570 nm. The light from the super-continuum source passes through an in-line polarizer. A polarization controller (PC) configured as a half-wave plate is used to rotate the polarization state of the light at the TFBGs. The device detects the SPR signature in the transmitted spectrum, allowing easy comparison between the channels. The transmission spectra through the TFBGs is recorded by an optical spectrum analyzer (OSA).

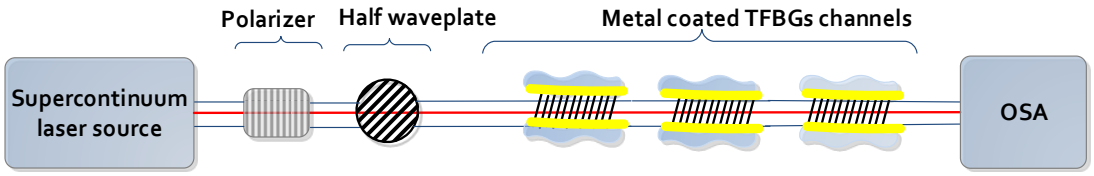

Fig. 45. Schematic diagram of the proposed in-line multiplexed SPR sensor based on three TFBGs with different tilt angles for the fiber Bragg gratings (TFBG). The output is characterized by the optical spectrum analyzer (OSA).

The sensor is made of a specially fabricated SMF in which tilted Bragg gratings have been written. The unique boron-germanium co-doped SMF has a single-mode core radius of 10.2 μm, and a cladding diameter of 145 μm [77]. The fiber has a ν-value of 1.9 at 1550nm and a core-to-cladding refractive index difference, Δn, of ~0.003 [77], and a cutoff wavelength 1.24 μm. The

benefit of using a small core-cladding index difference and large ν-value is to reduce the bandwidth of the coupled cladding modes, at the smallest tilt angles and hence the lowest polarization sensitivity of each device channel [22].

The TFBGs were written using a commercially available 213 nm Q-switched nanosecond Nd:VO_4 laser (Xiton Photonics) and a scanned phase-mask interferometer Model FBGTMI-913 from PhotoNova Inc., Montreal, Canada. The laser produces pulses of 7 ns with an energy of 10 μJ at a repetition frequency between 0.1 and 30 kHz with a maximum average power of 130 mW. The beam is about 1 mm in diameter and it has a relatively high wall-plug efficiency [70]. The grating is imprinted with the interferometer in which a UV beam is divided at a phase-mask and then recombined at the fiber by using two fold mirrors. The Bragg wavelength can be chosen independently of the UV laser wavelength by changing the mutual angle between the mirrors of the interferometer and the fiber plane [22]. A mirror on a linear translation stage was used to scan the fiber, and a 20 cm cylindrical lens is used to focus the UV light on the fiber which is held at the intersection of the beams. To fabricate tilted gratings, the fiber holder is rotated relative to the propagation axis of the fiber [22].

5.4 Results and Discussion

For our demonstration, we used three gratings in series as can be seen in Fig. 46, each with a different tilt angle for different operating wavelength bands. The central wavelength of the cladding modes is controlled by the mutual angle of the interferometer mirrors, and altering this angle allows the cladding mode coupling to move to different wavelengths. Our interferometer can be used to write gratings well below a Bragg wavelength of 600 nm.

The narrow bandwidth of the cladding modes of this fiber gives the opportunity to write the TFBGs by different techniques than the proposed one. Controlling the central wavelength of the cladding modes can be achieved easily by the tilt angle. Altering the tilt angle to larger angles allows the cladding mode coupling to move to longer wavelengths. The tilt angles can be arranged such that each subsequent grating's spectra follows the previous grating's spectra, without overlap. This also allows multiple distinct sensors to be fabricated in-line.

A second grating was written in the same fiber which has a cladding mode coupling signature different to the first TFBG, and so on. Using this construct, the signal transmitted through the

gratings from a supercontinuum source shows three distinct cladding mode spectra each with a narrow bandwidth of between 15 -25nm (See Fig. 46). We envision 20 distinct TFBGs (and hence distinct SPR sensors) may be written spanning the wavelength range from 1.24 μm, from the cut-off wavelength of the fiber, to 1700 nm, in a single optical fiber. The bandwidth of the cladding modes in this fiber is approximately 0.2 × that in SMF28 for the same tilt angle.

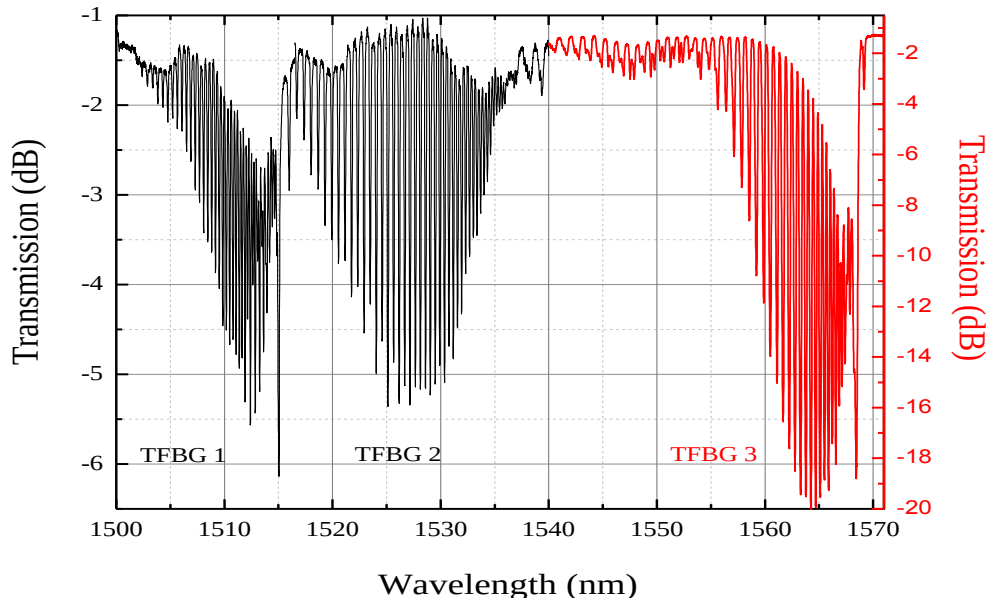

Fig. 46. Transmission of the multichannel TFBGs spectra in air from (a) the 4.5° TFBG at core Bragg wavelength of 1516 nm as channel 1(b) the 6° TFBG at core Bragg wavelength of 1539.5 nm as channel 2 (c) the 4° TFBG at core Bragg wavelength of 1569 nm as channel 3.

The transmission spectrum of each channel consists of two bands, with weak core mode resonances at 1516, 1539.5, 1569 nm, respectively, and a number of cladding modes on the short wavelength side of the core resonance. The wavelength at which the cladding mode begins can be calculated from [22]

$$\lambda_{start} = \frac{\lambda_{Bragg}}{2}\left(1 + \frac{n_{clad}}{n_{eff}}\right) \tag{5-1}$$

where λ_{start} indicates the wavelength at which the cladding mode coupling begins, n_{eff} is the effective refractive index of the core mode at the Bragg resonant wavelength (λ_{Bragg}), and n_{cl} is the cladding refractive index. Since the unique fiber has a large photosensitive core, decreasing Δn helps the cladding modes to start at a wavelength relatively closer to the Bragg core resonance and hence to lower-order cladding modes which have high effective refractive indices. This

enables the sensor to operate at higher SRIs of around 1.44 RIU as will be seen later. Also, since the TFBGs are written at different angles, the visibility of the lower and higher cladding modes is different. TFBG1 and TFBG3 excite the lower-order modes efficiently and their visibility is much higher than that of the higher-order counterparts. On the other hand, the lower-order modes of TFBG2 are relatively weak and almost invisible. The different excited cladding modes of the three channels enables the observation SPR signature at different SRIs and change the operating range of each channel based on the tilt angle. Thus the operating range of the three sensors is different and independent.

Fig. 47 shows the transmission response of the TFBGs without metal coatings to different SRI. It can be seen that for SRI of 1.41, all the higher-order modes can be discriminated.

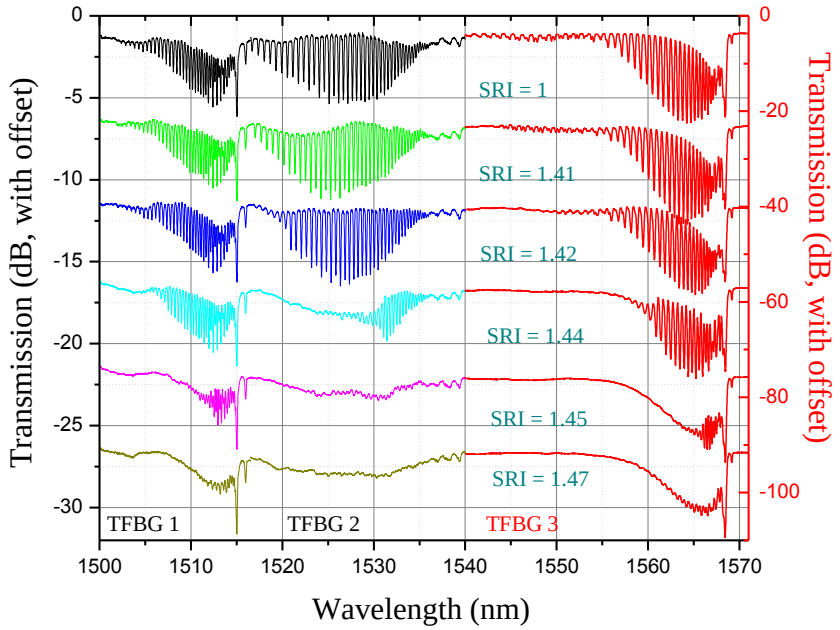

Fig. 47. The transmission spectra of three different TFBGs written with different tilt angles and at different operating wavelengths in series in response to surrounding refractive index (SRI) with no metal coatings.

Increasing the SRI affects the higher-order modes which disappear first, followed by the lower-order cladding modes until all the cladding modes disappear at an SRI of 1.45 RIU of TFBG2. As the SRI exceeds the effective refractive indices of the cladding modes, they can no longer exist as bound modes [72]. The lowest order cladding mode of TFBG1 and TFBG3 known as ghost mode, LP11 mode, is not affected since this mode is well confined to the fiber and has a

relatively low penetration depth into the SRI. The disappearing cladding modes can be easily discriminated in the three channels by increasing the SRI between 1.42 and 1.45 RIU. TFBG 1 and 3 can detect SRI up to 1.47 RIU where almost all the lower order cladding modes get affected except the ghost mode**.**

In the second manifestation of these distributed TFBG-SPR sensors, the same TFBGs were coated with 2 nm of Cr and 35 nm of gold. Their equivalent response to different SRI is shown in Fig. 48. When the effective refractive indices of the cladding modes are close to that of the SPR, as determined by the SRI, the excited cladding modes couple to the SPR and are dissipated in the metal. The change in the conditions of resonance coupling with the SRI will result in resonance shift [59]. As shown in Fig. 48, TFBG1 and TFBG3 provide better discrimination of the SPR signature and hence a different operating range at high values of the SRI, e.g. at an SRI of 1.43, and 1.44. This is, to our knowledge, the first time that a TFBG-SPR is operable at an SRI of 1.44 RIU. On the other hand, the SPR signature is invisible at these SRIs in TFBG2 because of the weak coupling to the lower-order cladding modes. For lower SRI of 1.40, 1.41, and 1.42, TFBG2 is the best channel to be used for sensing. The three sensors show a maximum SPR full width half-maximum (FWHM) spectral width of 2.5 nm.

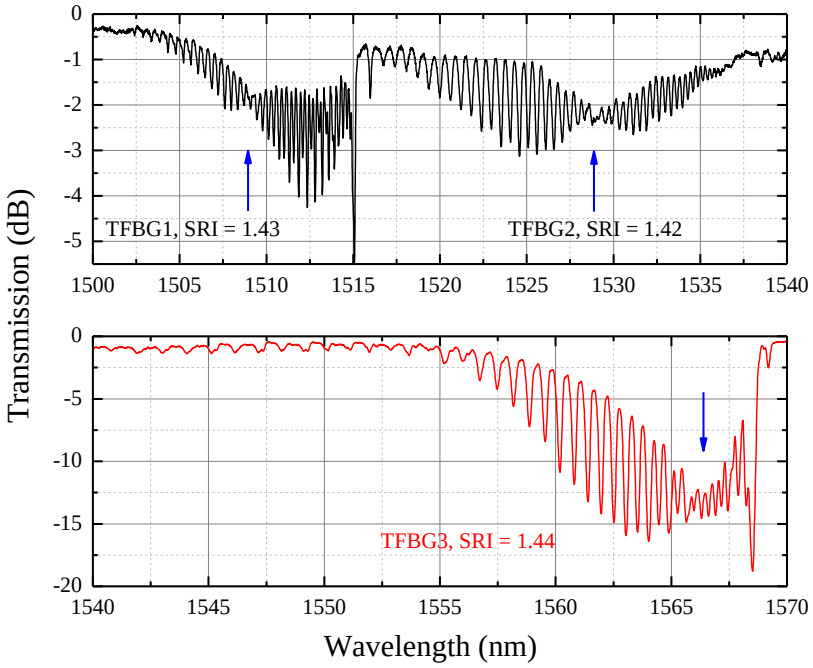

Fig. 48. SPR excitation of channels 1 and 2 (top) simutaneously in surrounding refractive index (SRI) of 1.43 and 1.42, respectively. Channel 3 (bottom) shows SPR excitation independently up to SRI of about 1.44 RIU. Arrows indicates the SPR signatures.

As was reported previously [41], [43], [44], [59], [76], coupling of the cladding modes to the SPR needs the polarization state to be matched between them and controlling the polarization state is therefore important for our sensors. These sensors may be oriented such that their polarization response is orthogonal, so that by selecting a particular polarization, only one sensor is interrogated. TFBG1 and TFBG2 are oriented to have the same polarization response and hence can excite SPRs simultaneously in SRI as can be seen in Fig. 48 (top), but TFBG3 is oriented to have an orthogonal polarization response to the others. Fig. 49 shows that in TFBG2 and TFBG3 sensors, excitation of the SPR depends strongly on the orientation and the state of polarization of the fundamental core mode. At an active SRI, rotating the linearly polarised light by 90° relative to the TFBGs plane turns the SPR coupling of a selected channel from the “on” (*s*-polarised mode), to the “off” (*p*-polarised mode) state independently.

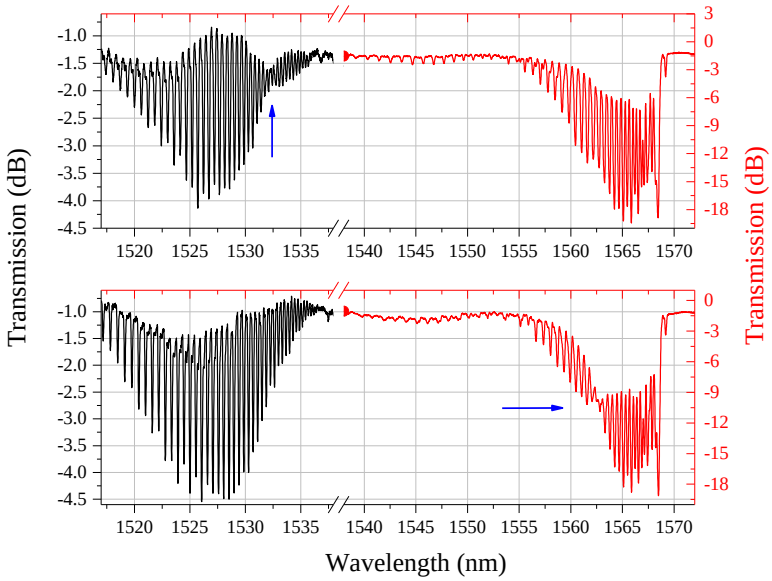

Fig. 49 Transmission spectra of two TFBG2 & 3 simutaneously with different tilt orientation at two different orthogonal linear states in SRI of 1.43 to turn the SPR of channel 2 (top) on or channel 3 (bottom) as required. Arrows indicates the SPR signature.

For the proposed concatenated TFBGs, we were able to arrange them to have an operating range of 1.42-1.44 RIU for TFBG1 and TFBG3, but maybe higher as seen in the spectra in Fig. 4. and 1.40-1.43 RIU for the TFBG2 sensor. Fig. 50 shows a linear response of the SPR as a function of the SRI. A sensitivity of ~500 nm/RIU is demonstrated for each sensor by calculating the slope. By considering the midpoint between the two adjacent cladding resonance dips close to the SPR envelope as the central SPR wavelength [59], we demonstrated a resolution of $\approx 7 \times 10^{-5}$ RIU with the OSA used in our setup, and with a maximum repeatability error of ± 0.035 nm. The SPR signature shifts towards longer wavelengths as the SRI increases.

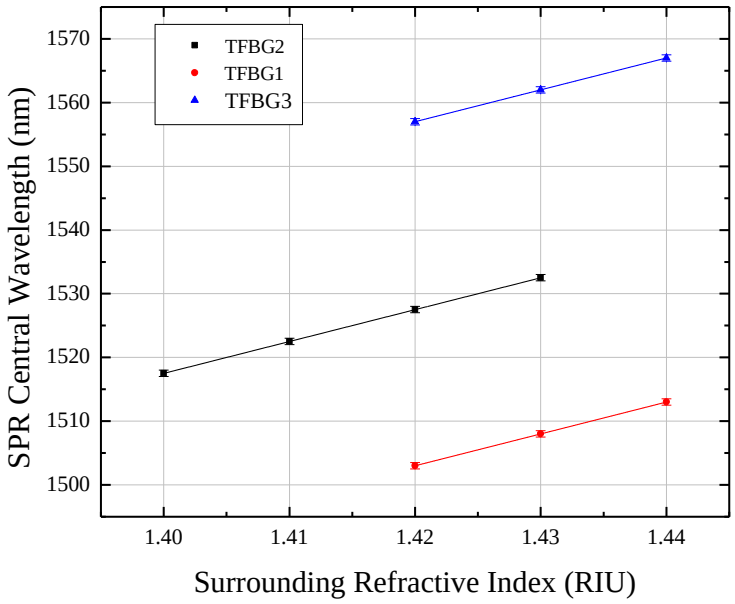

Fig. 50 Shift of the SPR wavelength as a function of the surrounding refractive index (SRI) of the three TFBGs coated with 2 nm chromium and 35 nm gold.

As shown in Fig. 50, TFBG2 provides a wider operating range, but the SPR signature is invisible at higher SRIs, i.e. at an SRI of 1.44. On the other hand, TFBG1 and TFBG3 show the SPR signature clearly at this SRI.

The operating range of the proposed sensors at SRI between 1.40 and 1.44 RIU gives the opportunity for various applications, e.g. to detect different pure petroleum products and their mixtures [59]. By simply using different fibers like the ones used in [59], stronger coupling occurs to cladding modes of lower effective indices than 1.40 RIU. Hence optimizing the dynamic range of the proposed multiplexing device for other SPR sensing applications.

5.5 Conclusion

In conclusion, this paper has shown for the first time the operation of concatenated TFBG sensors as well as concatenated SPR sensors in a single optical fiber. The channels have different TFBG tilt angles and operating wavelength providing a sensitivity of ~500 nm/RIU, and a SRI operating range from 1.40 to 1.44 RIU. By the appropriate choice of fiber and Bragg wavelengths, it is possible to multiplex more than a dozen SPR sensors in one fibre. The experimental results demonstrate a powerful scheme in which not only the SRI range and the spectral region of operation can be changed, but also the polarization sensitivity engineered for each sensor.

CHAPTER 6 ARTICLE 4: SILICON-COATED MULTI-CHANNEL SURFACE PLASMON RESONANCE SENSORS USING TILTED FIBER BRAGG GRATINGS

Mohamad Diaa Baiad,[1,*] Mathieu Gagné,[2] and Raman Kashyap[1,2]

The Fabulas Laboratory

[1]Department of Electrical Engineering, École Polytechnique Montréal, C.P. 6079, Succ. Centre-ville, Montréal H3C 3A7, QC, Canada

[2]Department of Engineering Physics, École Polytechnique Montréal, C.P. 6079, Succ. Centre-ville, Montréal H3C 3A7, QC, Canada

Submitted to Optics Letters on October 2014

OVERVIEW:

This paper shows the performance improvement of SPR-TFBG sensors using silicon coated fibers with gold and chromium. Coating the SPR-TFBG sensor with silicon for the first time shows improved sensitivity and custom-tuning of the sensor operating range. This article shows the capability of using different fibers and their advantages for SPR sensing with different Bragg gratings writing techniques, which are available in the Fabulas Laboratory at Polytechnique Montreal. The article results were presented at different meetings and international conferences like CIOFF 2014 (Plenary) in Havana of Cuba, and LAOP 2014 (Tutorial) in Cancun, Mexico. The complete reference to the article:

M. D. Baiad, M. Gagne, and R. Kashyap, " Silicon-coated multi-channel surface Plasmon resonance sensors using tilted fiber bragg gratings," In review, *Opt. Letters*, Oct. 2014.

6.1 Abstract

Experimental multi-channel surface Plasmon resonance (SPR) sensors scheme excited by a chromium, gold and silicon-coated optical fiber with a tilted fiber Bragg grating (TFBG) is presented. Different type of fibers, where each fiber represents one channel, have been used and each one shows a unique refractive index operating range. The high-index dielectric layer of silicon is used to tune the SPR refractive index operating range to a lower value. This system

provides a refractive index operating range from 1.30 to 1.435 RIU, which is the largest reported so far of such SPR-TFBG sensor to our knowledge. Adding the silicon layer improves the sensor sensitivity up to ~700 nm/RIU and shows stronger polarization dependency of such a sensor. The flexibility and the improved ease of use of the proposed scheme can be adapted to many SPR-TFBG based sensors applications.

6.2 Introduction

Recently, many schemes have been proposed for the use of surface Plasmon resonance (SPR) on gold coated optical fibers using tilted fiber Bragg gratings (TFBG) [41]. For example, a TFBG-SPR sensor has been proposed in a single mode fiber (SMF) coated with low-index polymer of Cytop and gold [47]. The sensor shows both long range SPR (LRSPR) and short range SPR (SRSPR) coupled modes over the wavelength range from 1525 to 1610 nm. The device provides a sensitivity of a maximum of 186 nm/RIU based on the SRI range of 1.31 to 1.35 RIU [47].

Different schemes have been proposed to track individual cladding mode resonances and their dependence on the state of polarization (SOP) to improve the resolution and the performance of the SPR-TFBG sensor [43], [44]. The first Stokes parameter and the polarization dependent loss (PDL) have been used experimentally to interrogate the SPR-TFBG. Such sensors show a maximum sensitivity of 673 nm/RIU between 1.31 and 1.38 RIU with a FWHM of the SPR envelope of 5 nm. Also, a TFBG-SMF has been coated with silver nanowires of 1-3 μm in length and 40-50 nm in diameter [48]. The PDL spectrum of the tilted fiber Bragg grating used to excite the cladding modes has been studied and shown to provide a sensitivity of 650 nm/RIU for a SRI range 1.330 to 1.347 RIU [48].

J. Albert proposed a multi-fiber TFBG-SPR sensing devices in SMF coated with 30-50 nm of gold attached [50]. The device provides a sensitivity of 500 nm/RIU between 1.32 and 1.42 RIU.

We previously proposed a TFBG-SPR sensor which allows the detection of SPR in the reflection spectrum using reflected guided cladding modes captured by a double-clad fiber coupler, and excited on a chromium and gold-coated fiber [59]. The sensor experimentally demonstrated a sensitivity of 510.5 nm/RIU and an operating range of 1.335 to 1.432 RIU over the wavelength range of 1525-1590 nm [59].

Also, we experimentally demonstrated a multichannel TFBG-SPR sensor scheme in a single optical fiber with chromium and gold coated fiber. The fiber used is a unique optical fiber which has a photosensitive core and narrow cladding mode bandwidth. The SRI range, the spectral region of operation, and the polarization sensitivity can be engineered for each sensor independently. The scheme shows an operating range of 1.40 to 1.44 RIU, and a sensitivity of 500 nm/RIU [78].

It was demonstrated that the sensitivity is improved up to one order of magnitude using a high-index prism SPR sensor scheme coated with silver and a top layer of 10-15 nm silicon [20]. Bhatia and Gupta demonstrated a SPR optical fiber sensor using a multi-mode fiber of 600 μm core diameter coated with metal and a thin 10 nm layer of silicon [21]. The sensor operated within a wavelength range between 600 and 900 nm and was demonstrated for a SRI between 1.333 to 1.353 RIU. The silicon layer improves the sensitivity of such a sensor and tunes the resonance wavelength [21].

In this paper, we demonstrate a powerful scheme for SPR sensor multiplexing using TFBGs in several different fibers. Each fiber shows a completely different operating range. In order to enhance the sensitivity of the sensor, we incorporated a layer of silicon on the metalized fiber for the first time of such a TFBG-SPR sensor. The silicon layer is used to tune the SRI operating range as well.

6.3 Experimental Procedure

The schematic of the proposed device is shown in Fig. 51. The single-mode core of a 50:50 standard coupler is connected to a super-continuum laser source (broadband source) in a wavelength range between 1500 and 1585 nm through branch (1). The light passes through an in-line polarizer and a polarization controller (PC) as a half-wave plate which is used to rotate the polarization state of the light reaching the TFBGs.

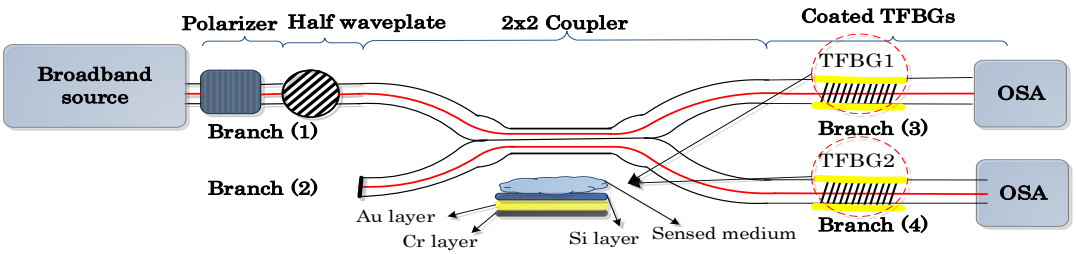

Fig. 51. Schematic diagram of the multichannel TFBG-SPR sensor. Light from a super-continuum laser source is coupled to the coated tilted fiber Bragg grating (TFBG) through a 2x2 standard coupler. Transmission spectra are characterized at branch (3) and branch (4) by the optical spectrum analyzer (OSA).

For our demonstration, we use only two branches with two TFBGs, TFBG1 of 1 cm length in branch (3) as channel 1 and TFBG2 of a 2 cm length in branch (4) as channel 2. The SMF fiber of branch (3) has a co-doped boron-germanium core [78]. This fiber has a narrower excited cladding modes bandwidth of approximately 0.2 × that of an SMF28 for the same tilt angle. It has a single-mode core radius of 10.2 μm, and a cladding diameter of 145 μm. Multiple distinct sensors with different operating wavelength can be fabricated into this branch easily as has been demonstrated recently [78]. Branch (4) has one 6° TFBG written into a different photosensitive *boron-germanium* co-doped fiber (Redfern, Eveleigh, NSW, Australia). TFBG2 has a single-mode core radius of 9.2 μm, and a cladding diameter of 125 μm. It has a broad excited cladding modes bandwidth of about 80 nm. The device is characterized by the two transmission spectra through the TFBGs which are recorded by optical spectrum analyzers (OSA) at the end of branch (3) and branch (4).

TFBG1 is written using a 213 nm Q-switched nanosecond Nd:VO_4 laser from Xiton Photonics and a scanned phase-mask interferometer (Model FBGTMI-913) from PhotoNova Inc., Montreal, Canada. By simply changing the mutual angle between the mirrors of the interferometer and the fiber plane, the Bragg wavelength can be chosen independently of the UV laser wavelength from 500 nm to >1700 nm. The fiber holder can be rotated relative to the propagation axis of the fiber in order to write TFBGs [22]. TFBG2 is written using a 266 nm solid-state nanosecond Q-switched frequency quadrupled yttrium lithium fluoride (YLF) laser, using a scanning phase mask technique [73]. In this case the TFBG was fabricated by rotating the phase mask by an angle of 6° relative to the propagation axis of the fiber [22].

6.4 Results and Discussion

The transmission spectra from the gold-coated TFBGs immersed in air are shown in Fig. 52. TFBG1 transmission spectrum consists of a weak core mode resonance at 1539.5 nm and a set of cladding resonances on the short wavelength side of the core resonance. Cladding mode resonances begin at a wavelength of 1538.5 nm and consist of relatively weak and almost invisible low-order cladding modes between 1538.5 and 1536 nm as well as many higher-order cladding modes to ~1514 nm. On the other hand, TFBG2 spectrum consists of a core mode resonance (Bragg reflection) at 1584 nm and cladding resonances from 1581 to 1510 nm.

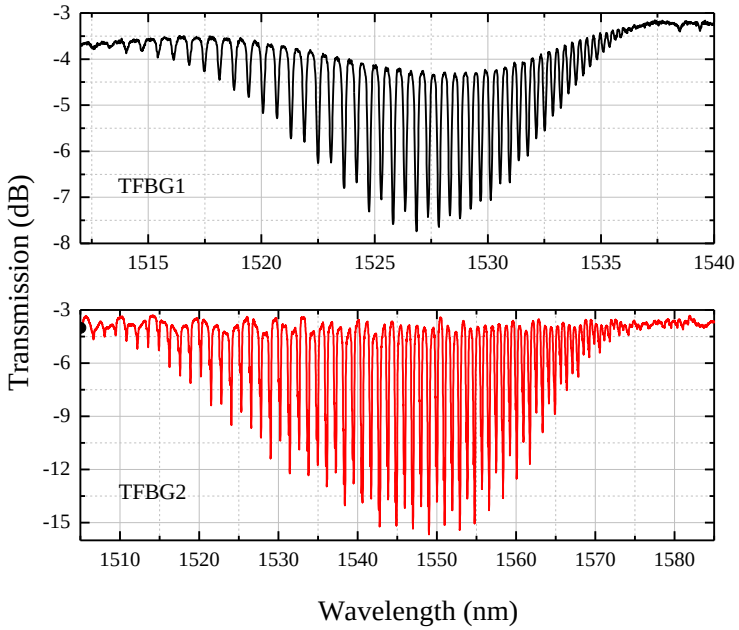

Fig. 52. Transmission spectra of the TFBGs in air from TFBG1 (top) at core Bragg wavelength of 1539.5 nm as channel 1 and TFBG2 (bottom) at core Bragg wavelength of 1584 nm as channel 2. Note that the bottom spectrum has a bandwidth almost 2× that of the top spectrum.

The two TFBGs have different operating wavelengths since the cladding bandwidth of each fiber is different and hence the refractive index operating range. The claddings bandwidth is related to the *v*-value and the core-cladding index difference of each fiber. A small core-cladding index difference and large *v*-value give the smallest cladding mode bandwidths, as well as small tilt angles and hence low polarization sensitivity of each device channel [22].

We use two different fibers and each fiber represents one channel for our demonstration, but it is possible to multiplex dozens of TFBG-SPR sensors using different types of fibers with different

characteristics. Also, multiple channels can be written in the same fiber and each has a cladding mode coupling signature different than the others as we have demonstrated recently by simply controlling the central wavelength of the cladding modes by tuning the mutual angle of the interferometer mirrors [78].

In the manifestation of these multiplexed TFBG-SPR sensors, the TFBGs were first coated with 2 nm of Cr and 35 nm of gold and then a 10 nm layer of silicon by sputtering, rotating the fiber by 180° in two exposures. In order to predict the behaviour of the proposed sensor, we use a geometrical optics picture and the Kretschmann configuration for simulation. We use the matrix method for 4 or 5 layers including the cladding, chromium, gold, with/without silicon and the SRI at 1550 nm [59], [60]. The reflection coefficient of the model for *p*-polarized light is $R=|r_p|^2$, where r_p is the amplitude reflection coefficient given by:

$$r_p = \frac{(M_{11} + M_{12} q_N) q_1 - (M_{21} + M_{22} q_N)}{(M_{11} + M_{12} q_N) q_1 + (M_{11} + M_{12} q_N)} \tag{6-1}$$

where:

$$M_d = \begin{pmatrix} \cos \beta_d & -i \sin \beta_d / q_d \\ -i q_d \sin \beta_d & \cos \beta_d \end{pmatrix} \tag{6-2}$$

$$q_d = (\varepsilon_d - n^2 \sin^2 \theta)^{1/2} \tag{6-3}$$

$$\beta_d = t_d (2\pi / \lambda)(\varepsilon_d - n^2 \sin^2 \theta)^{1/2} \tag{6-4}$$

considering M as the characteristic matrix of the proposed structure consisting of *N* number of layers and where ε_d being the dielectric constant of the layer, n its refractive index, and t_d is the thickness. The SPR resonant angle as a function of the SRI is shown in Fig. 53. The resonant angle corresponds to the localised minimum in the reflection coefficient [59].

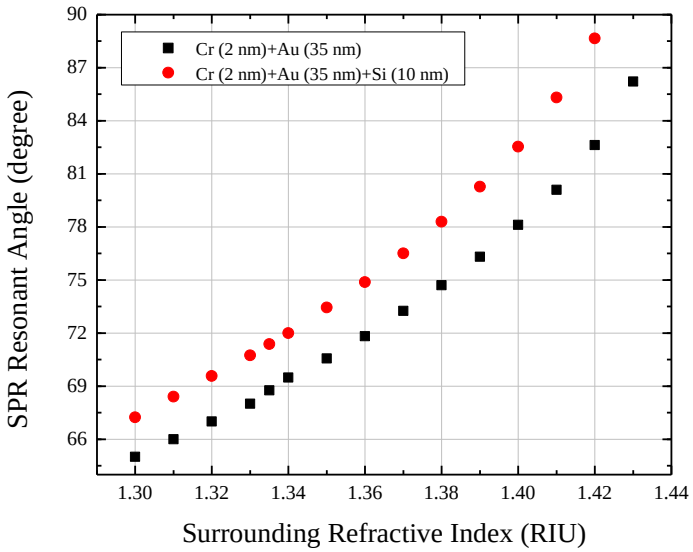

Fig. 53. Dependence of the calculated resonant SPR incident angles on the SRI for the proposed device when the TFBG is coated with 2 nm chromium, 35 nm of gold with/without 10 nm silicon layer.

It can be seen that as the SRI increases, the SPR resonant angles increase correspondingly to couple lower-order cladding modes to the SPR as the phase matching condition is satisfied with increased SRI. Fig. 53 shows that the resonant angles are shifted to higher angles by adding the 10 nm silicon layer to the metalized TFBGs. Hence, there is a shift in the central SPR resonance wavelength to longer wavelengths and a tuning in the SRI operating range of the device to a lower values.

Fig. 54 shows the response of TFBG1 to different SRI. If the effective refractive index of a cladding mode is close to that of the SPR as determined by the SRI, the cladding mode couples to the SPR and is dissipated at the resonant angle [59]. It can be seen that this channel has a SRI operating range of 1.40 to 1.435 RIU when the grating is coated with chromium and gold only. Adding the silicon layer to the metalized TFBG, shifts the operating range to a lower values between 1.385 and 1.42 RIU. This sensor shows a maximum SPR spectral width of 2.5 nm; the width has not changed by coating the channel with silicon.

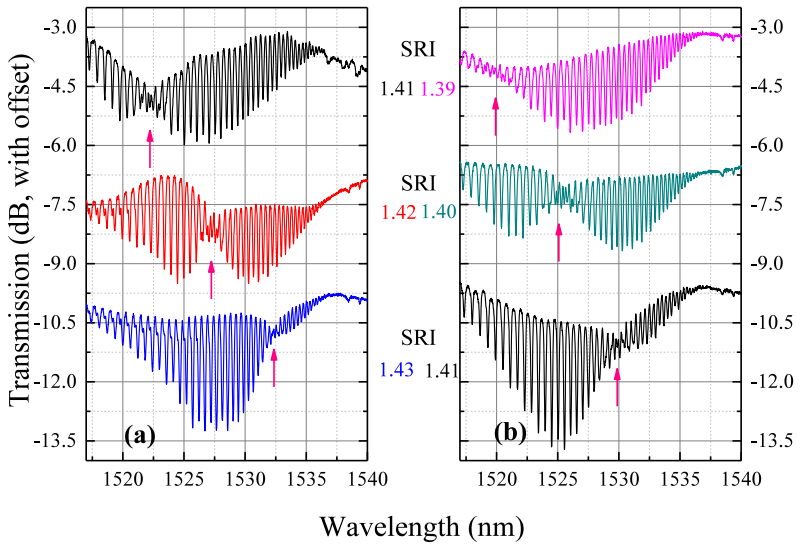

Fig. 54. SPR excitation of TFBG1 and shift with wavelength as the surrounding refractive index (SRI) increases (a) when coated with 2 nm chromium, 35 nm gold (b) when coated with 2 nm chromium, 35 nm gold, and 10 nm silicon. Arrows indicates the SPR signature.

On the other hand, the response of TFBG2 to different SRI can be seen in Fig. 55. TFBG2 has a SRI operating range between 1.31 and 1.41 RIU when the grating is coated with chromium and gold only. Adding the silicon layer to TFBG2, shifts the operating range to a lower values between 1.30 and 1.37 RIU. This fiber shows a maximum SPR spectral width of 5 nm when the TFBG is coated with chromium, gold and with/without silicon.

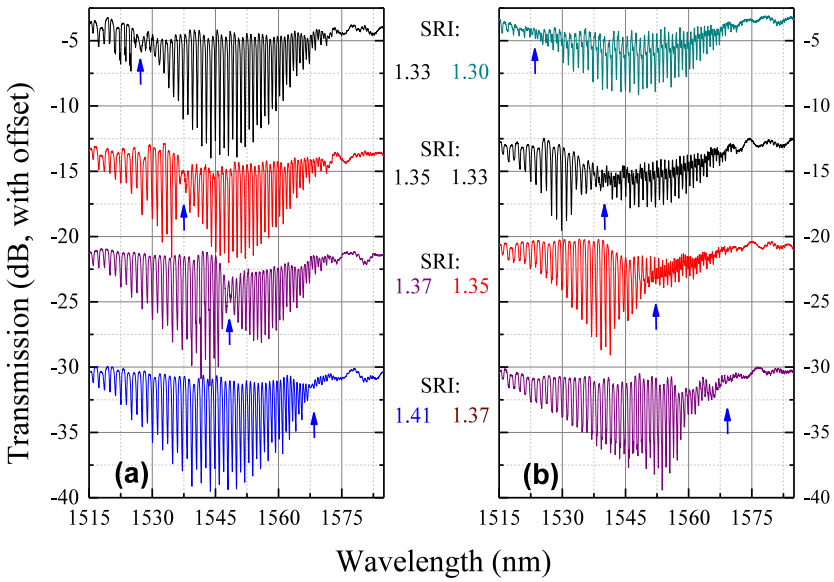

Fig. 55. Transmission spectra of TFBG2 showing the SPR excitation as the SRI increases (a) when coated with 2 nm chromium, 35 nm gold (b) when coated with 2 nm chromium, 35 nm gold, and 10 nm silicon. Arrows indicates the SPR signature.

As was reported previously [59], [76], SPR coupling is polarization sensitive where the polarization state of the cladding mode has to be matched to the SPR as a *p*-polarised mode. Our proposed scheme may be oriented such that each fiber polarization response is orthogonal, so that by selecting a particular polarization, only one sensor is interrogated and hence can excite the SPR independently. Fig. 56 shows such strong dependence of the two TFBGs when coated with silicon as well. At two different SRIs, rotating the linearly polarised light by 90° relative to the TFBGs plane turns one of the selected sensors from the “on” to the “off” state.

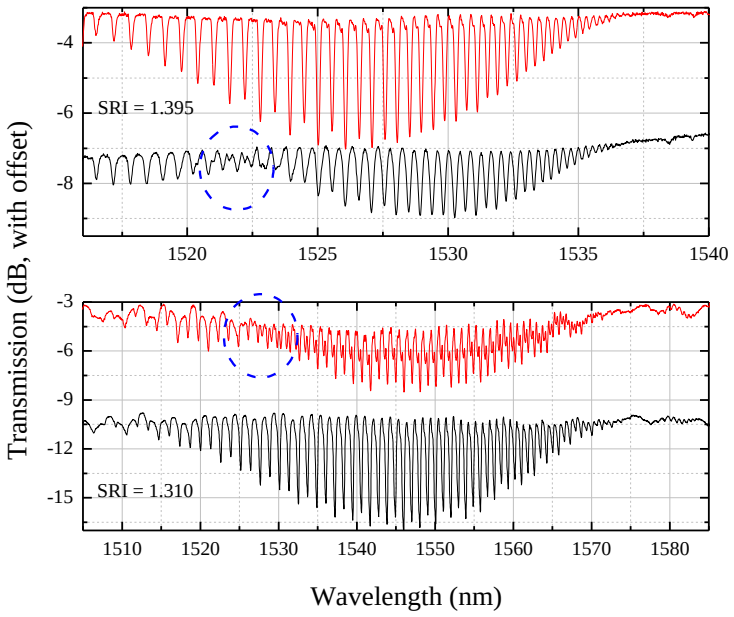

Fig. 56. Polarized transmission spectra of TFBG1 & 2 with different tilt orientation at two different orthogonal linear states (*p* & *s*-polarized states) in SRI of 1.395 and 1.310, respectively for TFBG1 & 2 coated with chromium, gold and silicon. Circles indicates the SPR signature.

A linear dependence of the SPR as a function of the SRI as can be seen in Fig. 57. for TFBG1 with/without the silicon layer. A sensitivity of ~500 nm/RIU is demonstrated for channel 1 by calculating the slope. It can be seen that the sensitivity of channel 1 remains the same at 500 nm/RIU before and after adding the silicon layer. This gives a resolution of ~ 7 x 10^{-5} RIU with the OSA used in our setup, and with a maximum repeatability error of ± 0.035 nm using the method which was reported previously [59]. Fig. 57. shows a similar linear dependence for TFBG2. The sensitivity of channel 2 before adding the silicon is close to that of channel 1 of ~509 nm/RIU. The high dielectric layer of silicon improves TFBG2's sensitivity up to ~700 nm/RIU and hence the resolution to 5 x 10^{-5} RIU. The two fibers show different responses to silicon due to their different characteristics and different diameters. TFBG2 fiber has a smaller cladding diameter than TFBG1 fiber leading to leakier cladding modes into the ambient sorrounding, stronger coupling due to the increase in the mode field overlap, and hence is more sensitive to the external index and the silicon layer. The sensitivity improvement of channel 2 is due to the increase in the interaction volume as well as the field intensity enhancement of the excitation close to the sensed medium due to the high index layer of silicon [20], [21].

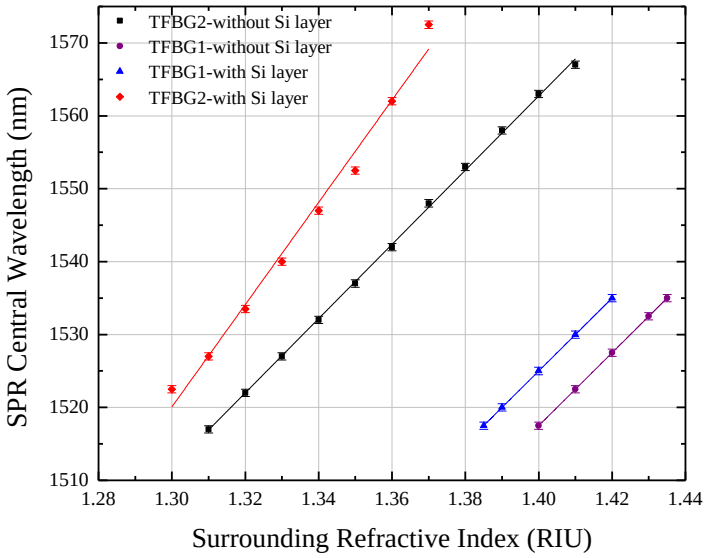

Fig. 57. SPR wavelength dependence on the surrounding refractive index (SRI) of the two used TFBGs coated with 2 nm chromium, 35 nm gold, and with/without 10 nm silicon. The straight lines are the fit to the data points.

Coating the metalized TFBG2 with silicon improves the polarization dependency of the proposed sensor compared to that coated with chromium and gold only as can be seen in Fig. 58. The cladding modes excited in pairs corresponding to *s*-mode and *p*-mode polarized light. TFBG is used to excite these pairs separately when coupled to the SPR [43], [44]. Adding the silicon layer improves the modification of the effective indices of these cladding pairs differently as can be seen in Fig. 58. It can be noted that such separation is seen to be weaker when the fiber is coated with chromium and gold only (See Fig. 58. top) whereas adding the 10 nm silicon modifies the separation of the pairs effective indices dramatically. For cladding modes at longer wavelengths than the SPR wavelength, the effective index of the *p*-polarised modes are less than the *s*-polarised ones. This happens because these *p*-polarised modes close to the SPR lose their energy to the metal which in turn lowers their effective refractive index and hence their resonant wavelengths compared to the *s*-polarised modes. The separation between each pair of modes and the amplitude is different based on the cladding mode orders [43], [44]. Such polarization dependence improvement indicates stronger localization of the *p*-polarised mode in the metalized and silicon layer and stronger sensitivity of the *p*-polarised mode to the SRI when the silicon layer is added. Adding the silicon layer shows the potential to improve the performance of the sensors which have been demonstrated previously based on tracking individual cladding mode

resonances [43], [44], or using different properties such as the first Stokes parameter and the polarization dependent loss [46] since it shows stronger polarization dependence.

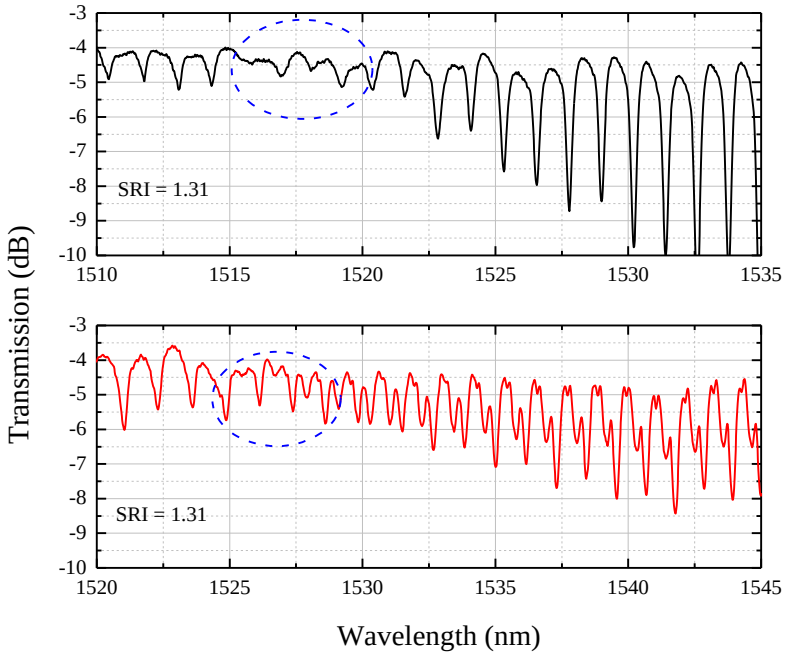

Fig. 58. Zoom on the TFBG2 SPR signatures of transmitted amplitude spectra for *p*-polarization modes in SRI of 1.31 RIU when TFBG2 is coated with chromium and gold without silicon (top) and with silicon (bottom). Circles indicates the SPR signature.

As shown in Fig. 57, TFBG1 and TFBG2 provide different operating ranges. TFBG1 has operating range efficient for high values of SRI, e.g., and can be easily extended to 1.44 RIU as we have demonstrated recently [78]. On the other hand, TFBG2 has a completely different and wider operating range which is convenient for lower SRIs, e.g. at 1.31 RIU. Such customized ranges give the opportunity for different applications varying from sensing petroleum mixtures [79] to biological applications [50], [80]. These sensors may find applications in the clinical environment. The proposed scheme can be used as a stand-alone sensor or as a multi-channel sensor.

6.5 Conclusion

A multichannel optical fiber SPR sensor scheme excited by a gold and silicon-coated fiber with TFBG is demonstrated. Different fibers of different characteristics have been used and each one shows a unique refractive index operating range. The silicon layer improves the flexibility of

such a sensor by tuning the SPR refractive index operating range to a desired value and improving the sensitivity of the system compared to previous similar techniques. The polarization state of each channel based on the TFBG orientation can be used to turn each SPR channel on or off as required. This system provides an improvement in the refractive index operating range from 1.30 to 1.435 RIU as the largest reported range so far of such sensor. It has a maximum improved sensitivity of around 700 nm/RIU and improved polarization dependence compared to other TFBG-SPR sensors. The proposed scheme is capable of simultaneous or independent multi-analyte sensing of various applications.

CHAPTER 7 GENERAL DISCUSSION

The work presented in this dissertation represents several novel schemes based on the fundamental discovery of SPR excitation using TFBGs. It demonstrate new methods to improve the SPR-TFBG performance in several aspects which can ensure the successful application of such sensors for various different applications.

Through the demonstration of the outlined objectives, this thesis represents the first experimental demonstration of the new proposed schemes and will contribute to the SPR-TFBG sensors field in the following:

- As it was mentioned in chapter 3, a novel and simple device, which is capable of capturing cladding modes efficiently including both low-order, as well as higher order cladding modes was presented. The reflection from a single FBG in a standard photosensitive SMF to couple the cladding modes into the inner cladding of a fusion spliced and diameter-matched DCF is proposed. The signal is viewed on the reflection port of a double-clad fibre coupler (DCFC). The technique described in our dissertation is a fusion tapering technique referenced in the following [71], [81], [82]. It is currently the industry standard as it produces couplers in a controlled and reproducible manner.

This scheme can capture the cladding modes with sufficient discrimination for all individual cladding modes. All earlier reported devices were not able to re-couple all involved cladding modes and this can be realised by comparing the reflection and transmission spectra [36], [38], [83]. We show that cladding modes within the wavelength band of 1500 nm and 1547 nm are captured efficiently as is evident from the matching transmission and reflection spectra. The captured reflected cladding modes can be adapted easily to SPR based sensors as was demonstrated in chapter 4. The proposed device shows the capability to measure the surrounding refractive index (SRI) with an extremely high sensitivity of between 1.37 and 1.45 RIU. It also provides a large SRI operating range from 1.30 to 1.45 RIU.

We also have shown that our device provides a unique and novel technique for measuring the SRI by tracking the disappearance of individual and clearly discriminated cladding modes showing a step of ~ 2.15×10^{-3} RIU/mode lost or a sensitivity of ≈ 465 modes lost/RIU between 1.37 and 1.45 RIU. This new method for sensing RI change is very different to other reported

ones as it affects single cladding modes which cannot be achieved by earlier work as the recaptured cladding modes are merged together and cannot be distinguished.

Also, using another technique for measuring the SRI which was reported in earlier works by measuring the reflected power over all the cladding modes, our device provides a sensitivity of total power drop by about ≈ 91% of its initial value. Earlier works have proposed devices which provides a maximum sensitivity of total power drop by about ≈ 73% of its initial value over the same RI range. Hence, using the same input power, our device shows a better sensitivity in comparison with earlier work to recapture cladding modes.

Furthermore, other reported configurations which have been used for recapturing of cladding modes with a TFBG so far provide a sensitivity over a range from 1.33 to 1.45 RIU [36], [38], [83]. On the other hand, ours provide a greater range from 1.30 to 1.45 RIU with an FBG by capturing the reflected cladding modes.

We have proved the concept and the idea of using the DCFC to recapture cladding modes with a strong FBG and its advantages over other reported configurations. We have shown that our concept can give better results than with a TFBG as reported earlier regarding the capturing of cladding modes and hence improve its dynamic range. Although we have used an FBG in our article, we have shown that our device has a better sensitivity in comparison with earlier work which used a TFBG. TFBGs can be implemented and used easily with our scheme with higher efficiency as has been shown in the subsequent article, chapter 4, for SPR sensing.

- In chapter 4, we present a simple and novel SPR sensor where the captured cladding modes in reflection by the DCFC and a TFBG in a standard photosensitive SMF has been used. The device efficiently measures the spectrum of the SPR-modified reflected cladding modes as well as that of the transmitted spectrum for comparison between the reflection and the transmission spectra. Also, the added convenience of observing both the transmitted and reflected spectra simultaneously, makes this sensor especially easy to use.

This sensor provides a significantly wider operating range between 1.335 and 1.430 RIU using the reflection spectrum, compared to those which used the transmission spectrum where operating range is between 1.335 and 1.41 RIU for the same fiber and same TFBG with worse discrimination of the cladding modes. Using the SPR-TFBG in reflection with sufficient discrimination of all individual captured cladding modes allows the extended SRI operating range

especially of the low order modes. Similar to other SPR-TFBG sensors, the device's response is strongly dependent on the polarization state, turning the SPR entirely on or off.

- As was mentioned in chapter 5, we have demonstrated a distributed SPR-TFBG sensors scheme in a single optical fiber for the first time. We demonstrated that concatenation of three SPR sensors is easily implemented using distributed in-line TFBGs in a single optical fiber. This scheme allows the sensing of different analytes by positioning in-line TFBGs with different tilt angles in which the wavelength operating range, the SRI range, and the polarization sensitivity of each channel can be engineered as required. Using different TFBGs with different tilt angles give the opportunity to control the operating range of each sensor. Also, since the TFBGs are written at different angles, the visibility of the lower and higher cladding modes is different and can be controlled easily. The different excited cladding modes of the three channels enable the observation SPR signature at different SRIs and change the operating range of each channel based on the tilt angle. Thus the operating range of the three sensors is different and independent.

The fiber which has been used in this article has relatively narrow cladding mode bandwidths of 15-25 nm which means it is possible to multiplex more than 20 channels in the same fiber between the cut-off wavelength of this fiber at 1240 nm and 1700 nm. Furthermore, by the appropriate choice of other fiber and Bragg wavelengths, it is possible to multiplex more than a dozen SPR sensors in one fibre where the wavelength and the operating range is customized. By using this powerful scheme, not only the SRI range and the spectral region of operation can be changed, but also the polarization sensitivity can be engineered for each sensor based on the orientation of the TFBGs.

The technique described in this article to imprint the TFBGs is the scanning phase mask interferometer technique. It is a flexible, easy-to-use technique and can be used to write TFBGs well below 600 nm. It is currently the industry standard as it produces Bragg gratings in a controlled and reproducible manner with low repeatability error.

- Chapter 6 presented an improvement of the SPR-TFBG sensors by coating the metalized TFBG with high dielectric layer of silicon where the sensitivity has been improved from 509 nm/RIU to 700 nm/RIU. The silicon layer is used to tune the SRI operating range as well. Hence, the silicon layer improves the flexibility of such a sensor by tuning the SPR refractive index operating range to a desired value and improving the sensitivity of the system compared to previous similar

techniques. The article demonstrated multi-channel SPR sensors using TFBGs in several different fibers where each one shows a different operating range. Similar to the scheme presented in chapter 5, the polarization state of each channel based on the TFBG orientation can be used to turn each SPR channel on or off as required, but using the silicon layer shows improved polarization dependency compared to other TFBG-SPR sensors where such dependency can improve the previously proposed schemes based on the polarization prosperities of such sensors and on tracking individual cladding mode. The proposed scheme is capable of simultaneous or independent multi-analyte sensing of various applications and can act as stand-alone sensor or multi-channel scheme. This system provides an improvement in the refractive index operating range from 1.30 to 1.435 RIU as the largest reported range so far of such sensor.

Also, a new method has been proposed in chapter 4 which helps to reduce the error of locating the SPR signature and hence improves the resolution. Such a method is repeatable with a maximum error of ± 0.035 nm/RIU. Some of the excited cladding modes couple to the SPR and are dissipated in the metal. Thus, the amplitude of these affected cladding modes is reduced significantly and locating the exact SPR position becomes more difficult. By using the proposed method, two adjacent cladding resonance dips with clear discrimination closest to the SPR signature are determined and then the midpoint between them is calculated. The repeatability error of such a calculation is significantly reduced and thus enhances the stability of the proposed schemes. The proposed schemes based on TFBGs design can be adapted to many different types of evanescent wave based sensors rather than SPR sensing, e.g. bend, temperature, and other refractive index based sensors. The temperature cross-sensitivity of these different TFBGs evanescent wave based sensors can be avoided by considering relative wavelength shifts instead of absolute spectral measurements [41] and noting that all cladding modes in the fibers tested have similar temperature sensitivities. Hence, these TFBG based sensors can be considered as temperature insensitive. The relative cladding modes shifts are less than ±12 pm within a temperature range from -9.4 to 69.5°C [91].

Nevertheless, the three proposed schemes of SPR-TFBG sensors allow excitation of cladding modes with clear improvement for each one. The schemes are combinable, for example the concatenation of SPR sensors in a single fiber can be coated with silicon to improve the sensitivity and tune the dynamic range and the scheme proposed in chapter 4 as well. Also, both

schemes in chapter 5 and 6 can be characterized in reflection to get better discrimination of the cladding modes and improve the dynamic range as was mentioned in chapter 4.

Despite the advantages of the proposed SPR-TFBG sensors, they impose limits. Some of the limitations which can be associated with them and should be overcome are that:

- Although the sensitivity is improved considerably to around 700 nm/RIU, the identification of the SPR-modified cladding resonances and the centre of the SPR signature can be an issue. The minimum proposed cladding bandwidth contain at least 20 separate cladding modes which make it difficult to distinguish the SPR signature of SPR-TFBG sensors compared with optical fiber SPR sensors with no gratings. Such methods could be obtained using different fibers with have less cladding bandwidth and less cladding modes or merged cladding bandwidth which make the discrimination much easier, but decreases the operating may range as well.

- Metal and silicon coatings are an issue too. Since the optical fiber is cylindrical, obtaining a uniform coating is somehow difficult. The coating depositions are achieved by sputtering, rotating the fiber by 180° in two exposures on the cylindrical optical fiber. So the thickness varies from zero to a maximum value of the desired thickness and this also makes the SPR envelope a little wider due to the position dependent coating thickness. In our configurations, each cladding mode has an incident angle and there is a wide range of angles. Therefore, a couple of guided cladding modes which have incident angles close to the SPR resonance angle are affected and this makes the SPR envelope a little wider. To solve this issue, coating the fiber in several steps and rotations is an option. Also, using a motor which rotate the fiber continuously during the deposition inside the chamber of the sputtering machine can make the coating uniform, but complicate the process.

- The variation between metal and silicon coatings of different SPR-TFBG samples can have some consequences on the reproducibility and mass production issues. The SPR envelope is directly related to the metal thickness. It narrows as the gold thickness increases. The FWHM of SPR dip directly relates to the sum of internal and radiation damping ($\Gamma_{rad} + \Gamma_i$). The FWHM of the SPR envelope depends strongly on radiation damping (Γ_{rad}) whereas internal damping (Γ_i) remains constant when the gold thickness is varied [15]. At optimal SPR resonance which has maximum depth (i.e., zero reflection for the Kretschmann configuration), internal damping is equal to radiation damping ($\Gamma_r = \Gamma_i$). If the metal thickness is less than optimal, radiation damping

increases ($\Gamma_{rad} > \Gamma_i$) and the FWHM of SPR dip becomes wider ($> 2 \times \Gamma_i$). On the other hand, the sum of internal and radiation damping decreases with metal thickness.

As it was mentioned previously, we characterize each sample thickness by a contour measuring system to ensure that the thickness difference is minimized. The maximum thickness error was ± 3 nm which could have a consequence in the case of mass production on the repeatability of such sensors.

- The deterioration of metal and silicon layers and the reuse of the proposed sensors can be an issue too. In our configurations, we use chromium as an adhesion layer which makes the gold layer adhere and helps it to last, but we realize that the silicon layer deposited above the gold deteriorates after 20 to 25 experiments. Thus, it is recommended to explore the ways to make the silicon layer more stable and reusable for longer. Also, exploration of other high-index dielectric coatings is an option too to improve the stability of such sensors.

- Although polarization dependence of SPR-TFBG sensors provides an opportunity to tune the SPR coupling on or off and in the proposed schemes of chapter 5 and 6, each channel response can be controlled based on the TFBG orientation, it also makes the fiber sensitive to fiber bends and movement. The fiber should be kept straight and stable in order to maintain the same polarization during the experiment. This can be an issue for in-field applications.

CHAPTER 8 CONCLUSION AND FUTURE WORK

This thesis has explored several novel schemes for the use of TFBG-SPR excitation for the sensing of surrounding refractive index (SRI). Four schemes have been introduced, demonstrated, and optimized experimentally. To facilitate the measurement of SRI, cladding modes are measured in reflection using a novel scheme based on the DCFC with high discrimination of all the captured cladding modes. This way both the transmission and reflection SPR signatures can be compared. The reflected cladding modes can precisely determine the SRI, as the dynamic range is large. The FBG alone shows a distinct form of operation with a very clear signature for the SRI. The reflected spectrum has been used for SPR sensing too. The scheme localises the SRI signature to a few cladding modes excited with TFBG and captured in reflection with the DCFC. The scheme based on the reflection spectrum improves the dynamic range of such a sensor and shows better discrimination of the SPR signature compared with the previous techniques which use the transmission spectrum only. The cladding bandwidth of this TFBG-SPR sensor is wide. Therefore, in order to design multiplexed TFBG-SPR sensors in a single optical fiber, a special optical fiber was used. The three cascaded TFBG-SPR sensors written into this fiber has a narrow bandwidth each. By using such fiber, it is possible to multiplex more than a dozen SPR sensors in one fibre using the same concept and same grating imprinting technique. Also, the powerful scheme allows the control of the SRI range, the spectral region of operation, and the polarization response of each channel independently.

In order to improve the sensitivity of the TFBG-SPR sensors, a silicon-coated the metalized optical fiber SPR sensors has been demonstrated. The fibers which have been used have different wavelength bandwidths and different characteristics. Each one shows a unique refractive index operating range. The silicon layer has been used also to tune the SPR refractive index operating range to a lower value as required. This system provides an improvement in the refractive index operating range as the largest reported range so far of such sensor. It has a maximum sensitivity of around 700 nm/RIU and improved polarization dependence compared to other TFBG-SPR sensors. A sensitivity improvement of ≈40 % has been demonstrated by silicon coating compared to the one without silicon-coating.

The new configurations being proposed allow better detection and discrimination of the SPR signature, improved sensitivity, and wider operating range. The fabrication of the proposed

schemes are simple and easy-to-use. Overall, the proposed configurations show a higher performance than previous work.

8.1 Direction for future work

There are several directions for future research which can be recommended to incorporate the objectives for efficiency enhancement of these schemes. It is a rich area for exploitation. The recommendations are presented below:

- The TFBGs length which has been used in this thesis varies between 1 and 2 cm. The separation between each TFBG of the cascaded TFBGs is 3 cm. Such separation can be customized as required. It is recommended to explore the effect of using shorter TFBGs on the schemes and the applications. This will lead to smaller and compact devices, will reduce the volume of the sensed medium, and will address the issue of cost and ease of manufacturing for numerous application in sensing systems.

- The concatenation of SPR sensors using TFBGs in a single optical fiber can be achieved by using different fibers to write the TFBGs at shorter wavelengths in the visible or near-infrared region by simply controlling by the mutual angle of the interferometer mirrors, and altering this angle allows the cladding mode coupling to move to different wavelengths. The PhotoNova Inc. interferometer has been already tested to write gratings well below a Bragg wavelength of 600 nm in a single mode fiber. This will lead to a more flexible device with more distinct SPR channels and will give the opportunity to compare between the parameters of the channels at the visible and at the telecommunication wavelength which has not been reported yet.

- It is recommended to explore different high-index dielectric other than silicon like graphene in order to obtain higher sensitivity and better performance, and also, to explore their stability during long term usage. Different high-index dielectric layer thicknesses can be explored to optimize the maximum sensitivity. Although this has been reported previously for different SPR optical fiber sensors, it has not been explored in details for SPR-TFBG sensors.

- Other metal coatings can be explored too for such SPR-TFBG sensors or even a combination of different metals in order to optimize the parameters of the sensors and the SPR excitation. This area is still not explored for these type of sensors. Also, there is a need to develop a complete

theoretical model for understanding the behaviour of SPR-TFBG sensor with such different metals and different high-index dielectric layers.

- It is recommended to improve the uniformity of metal and dielectric coatings to obtain narrower SPR signature and hence improve the figure of merit of the sensor.

- The schemes proposed in this dissertation show better performance and have high contribution to the field, but there is still a need to define a specific application to test these schemes and characterize their improvements to the field. Such applications can be the detection of different mixtures or pure petroleum, or bio-sensing applications via different immobilization chemistries, e.g. antibody based recognition to detect broad range of antigens, or aptamer based recognition to bind with thrombin by forming a G-quadruplex structure which is governed by electrostatic and hydrophobic interactions.

REFERENCES

[1] M. Zourob and A. Lakhtakia, *Optical Guided-Wave Chemical and Biosensors I*. Springer, 2010.

[2] J. Homola, *Surface plasmon resonance based sensors*. Springer, 2006.

[3] X. D. Hoa, "Guided immobilization of bioreceptors on nano-gratings for enhanced surface plasmon resonance biosensing," McGill University, 2009.

[4] R. W. Wood, "On a Remarkable Case of Uneven Distribution of Light in a Diffraction Grating Spectrum," *Proc. Phys. Soc. London*, vol. 18, no. 1, p. 269, 1902.

[5] E. Kretschmann and H. Raether, "Radiative decay of nonradiative surface plasmons excited by light," *Z. Naturforsch. A*, vol. 23, p. 2135, 1968.

[6] Jiří and Homola, "Optical fiber sensor based on surface plasmon excitation," *Sensors Actuators B Chem.*, vol. 29, no. 1–3, pp. 401–405, 1995.

[7] J. H. and R. Slavik, "Fiber-optic sensor based on surface plasmon resonance," *Electron. Lett.*, vol. 32, pp. 480–482, 1996.

[8] R. Slavík, J. Homola, J. Čtyroký, and E. Brynda, "Novel spectral fiber optic sensor based on surface plasmon resonance," *Sensors Actuators B Chem.*, vol. 74, no. 1–3, pp. 106–111, 2001.

[9] I. Abdulhalim, M. Zourob, and A. Lakhtakia, "Surface Plasmon Resonance for Biosensing: A Mini-Review," *Electromagnetics*, vol. 28, no. 3, pp. 214–242, 2008.

[10] J. Homola, S. S. Yee, and G. Gauglitz, "Surface plasmon resonance sensors: review," *Sensors Actuators B Chem.*, vol. 54, no. 1–2, pp. 3–15, 1999.

[11] R. Kashyap and G. Nemova, "Surface Plasmon Resonance-Based Fiber and Planar Waveguide Sensors," *J. Sensors*, vol. 2009, pp. 1–10, 2009.

[12] D. Monzón-Hernández, J. Villatoro, D. Talavera, and D. Luna-Moreno, "Optical-Fiber Surface-Plasmon Resonance Sensor with Multiple Resonance Peaks," *Appl. Opt.*, vol. 43, no. 6, pp. 1216–1220, 2004.

[13] A. K. Sharma, R. Jha, and B. D. Gupta, "Fiber-Optic Sensors Based on Surface Plasmon Resonance: A Comprehensive Review," *Sensors Journal, IEEE*, vol. 7, no. 8, pp. 1118–1129, 2007.

[14] J. Homola, I. Koudela, and S. S. Yee, “Surface plasmon resonance sensors based on diffraction gratings and prism couplers: sensitivity comparison,” *Sensors Actuators B Chem.*, vol. 54, no. 1–2, pp. 16–24, 1999.

[15] H. Raether, *Surface plasmons on smooth and rough surfaces and on gratings*, no. v. 111. Springer, 1988.

[16] J. H. and R. Slavik, R. Slavík, J. Homola, J. Čtyroký, and E. Brynda, “Fiber-optic sensor based on surface plasmon resonance,” *Electron. Lett.*, vol. 32, no. 1–3, pp. 480–482, 1996.

[17] L. De Maria, M. Martinelli, and G. Vegetti, “Fiber-optic sensor based on surface plasmon interrogation,” *Sensors Actuators B Chem.*, vol. 12, no. 3, pp. 221–223, 1993.

[18] R. Slavik, J. Homola, J. Ctyroky, and E. Brynda, “Novel spectral fiber optic sensor based on surface plasmon resonance,” *Sensors Actuators B Chem.*, vol. 74, no. 1–3, pp. 106–111, Apr. 2001.

[19] A. Lahav, M. Auslender, I. Abdulhalim, R. Verma, B. D. Gupta, and R. Jha, “Sensitivity enhancement of a surface plasmon resonance based biomolecules sensor using graphene and silicon layers,” *Sensors Actuators B Chem.*, vol. 33, no. 1, pp. 623–631, Nov. 2008.

[20] A. Lahav, M. Auslender, and I. Abdulhalim, “Sensitivity enhancement of guided-wave surface-plasmon resonance sensors,” *Opt. Lett.*, vol. 33, no. 21, pp. 2539–2541, Nov. 2008.

[21] P. Bhatia and B. D. Gupta, “Surface-plasmon-resonance-based fiber-optic refractive index sensor: sensitivity enhancement,” *Appl. Opt.*, vol. 50, no. 14, pp. 2032–2036, 2011.

[22] R. Kashyap, *Fiber Bragg Gratings*. Academic Press, 2009.

[23] J. ČtyrokÝ, F. Abdelmalek, W. Ecke, and K. Usbeck, “Modelling of the surface plasmon resonance waveguide sensor with Bragg grating,” *Opt. Quantum Electron.*, vol. 31, no. 9, pp. 927–941, 1999.

[24] B. Špačková, M. Piliarik, P. Kvasnička, C. Themistos, M. Rajarajan, and J. Homola, “Novel concept of multi-channel fiber optic surface plasmon resonance sensor,” *Sensors Actuators B Chem.*, vol. 139, no. 1, pp. 199–203, 2009.

[25] M. D. Baiad, S. M. Tripathi, A. Kumar, G. Nenova, and R. Kashyap, “Integrated optical bio-sensor based on pure surface plasmon-polariton excited by a waveguide grating,” in *Fibre and Optical Passive Components (WFOPC), 2011 7th Workshop on*, 2011, pp. 1–5.

[26] G. Nemova and R. Kashyap, “Fiber-Bragg-grating-assisted surface plasmon-polariton sensor,” *Opt. Lett.*, vol. 31, no. 14, pp. 2118–2120, 2006.

[27] G. Nemova and R. Kashyap, “Theoretical model of a planar waveguide refractive index sensor assisted by a corrugated long period metal grating,” *Opt. Commun.*, vol. 281, no. 6, pp. 1522–1528, 2008.

[28] G. Nemova and R. Kashyap, “Theoretical model of a planar integrated refractive index sensor based on surface plasmon-polariton excitation,” *Opt. Commun.*, vol. 275, no. 1, pp. 76–82, 2007.

[29] M. D. Baiad, S. M. Tripathi, A. Kumar, and R. Kashyap, “Pure surface plasmon-polariton optical sensor using an H-cross-section fiber and Bragg gratings,” in *Proc. SPIE 8412, Photonics North*, 2012, p. 84120J.

[30] S. M. Tripathi, A. Kumar, E. Marin, and J.-P. Meunier, “Side-Polished Optical Fiber Grating-Based Refractive Index Sensors Utilizing the Pure Surface Plasmon Polariton,” *Light. Technol. J.*, vol. 26, no. 13, pp. 1980–1985, 2008.

[31] G. Nemova and R. Kashyap, “A Compact Integrated Planar-Waveguide Refractive-Index Sensor Based on a Corrugated Metal Grating,” *Light. Technol. J.*, vol. 25, no. 8, pp. 2244–2250, 2007.

[32] Y. Y. Shevchenko and J. Albert, “Plasmon resonances in gold-coated tilted fiber Bragg gratings,” *Opt. Lett.*, vol. 32, no. 3, pp. 211–213, 2007.

[33] O. V Ivanov, S. A. Nikitov, and Y. V Gulyaev, “Cladding modes of optical fibers: properties and applications,” *Physics-Uspekhi*, vol. 49, no. 2, p. 167, 2006.

[34] R. Kashyap, *Fiber Bragg gratings*. Academic Press, 1999.

[35] T. Guo, A. Ivanov, C. Chen, and J. Albert, “Temperature-independent tilted fiber grating vibration sensor based on cladding-core recoupling,” *Opt. Lett.*, vol. 33, no. 9, pp. 1004–1006, 2008.

[36] T. Guo, H.-Y. Tam, P. A. Krug, and J. Albert, “Reflective tilted fiber Bragg grating refractometer based on strong cladding to core recoupling,” *Opt. Express*, vol. 17, no. 7, pp. 5736–5742, Mar. 2009.

[37] T. Guo, L. Shao, H.-Y. Tam, P. A. Krug, and J. Albert, “Tilted fiber grating accelerometer incorporating an abrupt biconical taper for cladding to core recoupling,” *Opt. Express*, vol. 17, no. 23, pp. 20651–20660, Nov. 2009.

[38] Y. Hibino, “Cladding-Mode-Recoupling-Based Tilted Fiber Bragg Grating Sensor With a Core-Diameter-Mismatched Fiber Section,” *Photonics Journal, IEEE*, vol. 2, no. 2. pp. 152–157, 2010.

[39] M. Han, F. Guo, and Y. Lu, “Optical fiber refractometer based on cladding-mode Bragg grating,” *Opt. Lett.*, vol. 35, no. 3, pp. 399–401, 2010.

[40] A.-P. Zhang, X.-M. Tao, W.-H. Chung, B.-O. Guan, and H.-Y. Tam, "Cladding-mode-assisted recouplings in concatenated long-period and fiber Bragg gratings," *Opt. Lett.*, vol. 27, no. 14, pp. 1214–1216, 2002.

[41] J. Albert, L.-Y. Shao, and C. Caucheteur, "Tilted fiber Bragg grating sensors," *Laser Photon. Rev.*, vol. 7, no. 1, pp. 83–108, 2013.

[42] C. Holmes, K. R. Daly, I. J. G. Sparrow, J. C. Gates, G. D'Alessandro, and P. G. R. Smith, "Excitation of Surface Plasmons Using Tilted Planar-Waveguide Bragg Gratings," *Photonics Journal, IEEE*, vol. 3, no. 5, pp. 777–788, 2011.

[43] C. Caucheteur, V. Voisin, P. Megret, and J. Albert, "Polarization dependency of surface plasmon resonance based tilted fiber Bragg gratings refractometers," *Proc. SPIE*, vol. 8421. p. 84214U–84214U–4, 2012.

[44] C. Caucheteur, V. Voisin, and J. Albert, "Polarized spectral combs probe optical fiber surface plasmons," *Opt. Express*, vol. 21, no. 3, pp. 3055–3066, 2013.

[45] J. Caucheteur, C. and Chen, C. and Voisin, V. and Berini, P. and Albert, "A thin metal sheath lifts the EH to HE degeneracy in the cladding mode refractometric sensitivity of optical fiber sensors," *Appl. Phys. Lett.*, vol. 99, no. 041118, 2011.

[46] C. Caucheteur, Y. Shevchenko, L.-Y. Shao, M. Wuilpart, and J. Albert, "High resolution interrogation of tilted fiber grating SPR sensors from polarization properties measurement," *Opt. Express*, vol. 19, no. 2, pp. 1656–1664, Jan. 2011.

[47] C. Chen, C. Caucheteur, V. Voisin, J. Albert, and P. Berini, "Long-range surface plasmons on gold-coated single-mode fibres," *J. Opt. Soc. Am. B*, 2014.

[48] J.-M. Renoirt, M. Debliquy, J. Albert, A. Ianoul, and C. Caucheteur, "Surface Plasmon Resonances in Oriented Silver Nanowire Coatings on Optical Fibers," *J. Phys. Chem. C*, vol. 118, no. 20, pp. 11035–11042, 2014.

[49] C.-F. Chan, C. Chen, A. Jafari, A. Laronche, D. J. Thomson, and J. Albert, "Optical fiber refractometer using narrowband cladding-mode resonance shifts," *Appl. Opt.*, vol. 46, no. 7, pp. 1142–1149, Mar. 2007.

[50] J. Albert, S. Lepinay, C. Caucheteur, and M. C. DeRosa, "High resolution grating-assisted surface plasmon resonance fiber optic aptasensor," *Methods*, vol. 63, no. 3, pp. 239–254, 2013.

[51] M. L. Brongersma and P. G. Kik, *Surface plasmon nanophotonics*, no. v. 131. Springer, 2007.

[52] P. B. Johnson and R. W. Christy, "Optical Constants of the Noble Metals," *Phys. Rev. B*, vol. 6, no. 12, p. 4370 LP – 4379, Dec. 1972.

[53] V. M. Shalaev and S. Kawata, *Nanophotonics with surface plasmons*. Elsevier, 2007.

[54] R. Slavík, J. Homola, and J. Čtyroký, "Single-mode optical fiber surface plasmon resonance sensor," *Sensors Actuators B Chem.*, vol. 54, no. 1–2, pp. 74–79, Jan. 1999.

[55] J. Čtyroky´, J. Homola, and M. Skalsky´, "Modelling of surface plasmon resonance waveguide sensor by complex mode expansion and propagation method," *Opt. Quantum Electron.*, vol. 29, no. 2, pp. 301–311, 1997.

[56] R. B. Dyott, *Elliptical fiber waveguides*. Artech House, 1995.

[57] A. Kumar and A. K. A. K. Ghatak, *Polarization of Light with Applications in Optical Fibers*. SPIE, 2011.

[58] A. Kumar and R. K. Varshney, "Propagation characteristics of highly elliptical core optical waveguides: a perturbation approach," *Opt. Quantum Electron.*, vol. 16, no. 4, pp. 349–354, 1984.

[59] M. D. Baiad, M. Gagné, W.-J. Madore, E. De Montigny, N. Godbout, C. Boudoux, and R. Kashyap, "Surface plasmon resonance sensor interrogation with a double-clad fiber coupler and cladding modes excited by a tilted fiber Bragg grating," *Opt. Lett.*, vol. 38, no. 22, pp. 4911–4914, Nov. 2013.

[60] R. Verma, B. D. Gupta, and R. Jha, "Sensitivity enhancement of a surface plasmon resonance based biomolecules sensor using graphene and silicon layers," *Sensors Actuators B Chem.*, vol. 160, no. 1, pp. 623–631, 2011.

[61] W. W. Morey, G. Meltz, and W. H. Glenn, "Holographically generated gratings in optical fibers," *Opt. Photon. News*, vol. 1, no. 7, pp. 14–16, Jul. 1990.

[62] K. O. Hill, B. Malo, K. A. Vineberg, F. Bilodeau, D. C. Johnson, and I. Skinner, "Efficient mode conversion in telecommunication fibre using externally written gratings," *Electronics Letters*, vol. 26, no. 16. pp. 1270–1272, 1990.

[63] J. M. Lerner, J. Flamand, J. P. Laude, G. Passereau, and A. Thevenon, "Diffraction Gratings Ruled And Holographic - A Review," 1981, vol. 0240, pp. 82–89.

[64] J. Martin, J. Lauzon, S. Thibault, and F. Ouellette, "Novel Writing Technique of Long and Highly Reflective In-fiber Bragg Gratings and Investigation of the Linearly Chirped Component," in *Conference on Optical Fiber Communication*, 1994, vol. 4, p. PD29.

[65] T. Erdogan, "Fiber grating spectra," *Lightwave Technology, Journal of*, vol. 15, no. 8. pp. 1277–1294, 1997.

[66] M. Gagné, "Fabrication holographique de réseaux de bragg par interférométrie à phase variable de type pousser/tirer," Polytechnique Montreal, 2009.

[67] K. Zhou, L. Zhang, X. Chen, and I. Bennion, “Low Thermal Sensitivity Grating Devices Based on Ex-45° Tilting Structure Capable of Forward-Propagating Cladding Modes Coupling,” *Lightwave Technology, Journal of*, vol. 24, no. 12. pp. 5087–5094, 2006.

[68] L. Dong, B. Ortega, and L. Reekie, “Coupling characteristics of cladding modes in tilted optical fiber Bragg gratings,” *Appl. Opt.*, vol. 37, no. 22, pp. 5099–5105, 1998.

[69] M. Gagné and R. Kashyap, “New nanosecond Q-switched 213 and 224-nm lasers for fiber Bragg grating writing in hydrogen-free optical fibers,” in *Spie*, 2012, pp. 8243–41.

[70] M. Gagné and R. Kashyap, “New nanosecond Q-switched Nd:VO4 laser fifth harmonic for fast hydrogen-free fiber Bragg gratings fabrication,” *Opt. Commun.*, vol. 283, no. 24, pp. 5028–5032, 2010.

[71] S. Lemire-Renaud, M. Rivard, M. Strupler, D. Morneau, F. Verpillat, X. Daxhelet, N. Godbout, and C. Boudoux, “Double-clad fiber coupler for endoscopy,” *Opt. Express*, vol. 18, no. 10, pp. 9755–9764, 2010.

[72] M. D. Baiad, M. Gagné, S. Lemire-Renaud, E. De Montigny, W.-J. Madore, N. Godbout, C. Boudoux, and R. Kashyap, “Capturing reflected cladding modes from a fiber Bragg grating with a double-clad fiber coupler,” *Opt. Express*, vol. 21, no. 6, pp. 6873–6879, Mar. 2013.

[73] M. Gagné and R. Kashyap, “New nanosecond Q-switched 213 and 224nm lasers for fiber Bragg grating inscription in hydrogen-free fibers,” pp. 824314–824316, 2012.

[74] R. C. Jorgenson and S. S. Yee, “A fiber-optic chemical sensor based on surface plasmon resonance,” *Sensors Actuators B Chem.*, vol. 12, no. 3, pp. 213–220, 1993.

[75] R. K. V. and B. D. G. S. Singh, “Surface plasmon resonance based fiber optic sensor with symmetric and asymmetric metallic coatings: a comparative study,” *Sensors & Transducers*, vol. 100, no. 1, pp. 116–124, 2009.

[76] Y. Shevchenko, C. Chen, M. A. Dakka, and J. Albert, “Polarization-selective grating excitation of plasmons in cylindrical optical fibers,” *Opt. Lett.*, vol. 35, no. 5, pp. 637–639, Mar. 2010.

[77] M. J. Holmes, R. Kashyap, R. Wyatt, and R. P. Smith, “Development of radiation-mode filters for WDM,” *Multiwavelength Optical Networks: Devices, Systems and Network Implementations (Ref. No. 1998/296), IEE Colloquium on*. pp. 10/1–10/5, 1998.

[78] M. D. Baiad and R. Kashyap, “Concatenation of surface Plasmon resonance sensors in a single optical fiber using tilted fiber Bragg gratings,” *Opt. Lett.*, 2014.

[79] D. Li, X. Zhang, R. Zhu, P. Wu, H. Yu, and K. Xu, “A Method to Detect the Mixed Petrol Interface by Refractive Index Measurement With a Fiber-Optic SPR Sensor,” *Sensors Journal, IEEE*, vol. 14, no. 10. pp. 3701–3707, 2014.

[80] Y. Shevchenko, T. J. Francis, D. A. D. Blair, R. Walsh, M. C. DeRosa, and J. Albert, “In Situ Biosensing with a Surface Plasmon Resonance Fiber Grating Aptasensor,” *Anal. Chem.*, vol. 83, no. 18, pp. 7027–7034, 2011.

[81] T. A. Birks and Y. W. Li, “The shape of fiber tapers,” *Lightwave Technology, Journal of*, vol. 10, no. 4. pp. 432–438, 1992.

[82] S. Lemire-Renaud, M. Strupler, F. Benboujja, N. Godbout, and C. Boudoux, “Double-clad fiber with a tapered end for confocal endomicroscopy,” *Biomed. Opt. Express*, vol. 2, no. 11, pp. 2961–2972, Nov. 2011.

[83] T. Guo, L. Shao, H.-Y. Tam, P. A. Krug, J. Albert, A. Ivanov, and C. Chen, “Temperature-independent tilted fiber grating vibration sensor based on cladding-core recoupling,” *Opt. Express*, vol. 33, no. 23, pp. 1004–1006, Nov. 2008.

[84] K. O. Hill, Y. Fujii, D. C. Johnson, and B. S. Kawasaki, “Photosensitivity in optical fiber waveguides: Application to reflection filter fabrication,” *Appl. Phys. Lett.*, vol. 32, no. 10, 1978.

[85] A. Othonos, “Fiber Bragg gratings,” *Rev. Sci. Instrum.*, vol. 68, no. 12, 1997.

[86] N. Groothoff and J. Canning, “Enhanced type IIA gratings for high-temperature operation,” *Opt. Lett.*, vol. 29, no. 20, pp. 2360–2362, Oct. 2004.

[87] A. Othonos, “Fiber Bragg gratings,” *Rev. Sci. Instrum.*, vol. 68, no. 12, 1997.

[88] A. I. Gusarov, F. Berghmans, A. F. Fernandez, O. Deparis, Y. Defosse, D. Starodubov, M. Decreton, P. Megret, and M. Bondel, “Behavior of fibre Bragg gratings under high total dose gamma radiation,” *Nuclear Science, IEEE Transactions on*, vol. 47, no. 3. pp. 688–692, 2000.

[89] J. Albert, Y. Hibino, M. Kawachi, B. Malo, F. Bilodeau, D. C. Johnson, and K. O. Hill, “Photosensitivity in Ge-doped silica optical waveguides and fibers with 193-nm light from an ArF excimer laser,” *Opt. Lett.*, vol. 19, no. 6, pp. 387–389, Mar. 1994.

[90] D. L. Williams, “Novel method of producing all fibre photoinduced chirped gratings,” *Electron. Lett.*, vol. 30, no. 12, pp. 996–998(2), Jun. 1994.

[91] Chen, C.; Albert, J., "Strain-optic coefficients of individual cladding modes of single mode fibre: theory and experiment," *Electronics Letters* , vol.42, no.18, pp.1027,1028, Aug. 31 2006

APPENDIX A: PHOTOSENSITIVITY

Hill *et al.* [84] in 1978 was the first to discover photosensitivity in germanium-doped silica fiber at the Communication Research Center in Canada. His discovery was during an experiment to study the nonlinear effects in a specially designed optical fiber by a visible light from an Argon laser [85]. Photosensitivity refers to the permanent change in the refractive index of glass induced by exposure to light radiation [22]. When glass is exposed to high intensity UV laser, the refractive index can be increased or decreased through changes happens in the glass structure [66]. A model, called the Kramers-Kronig relation, to explain the change in the index of refraction has been introduced by relating it to the absorption changes. It proposed the breaking of the GeO glass defect resulting in a GeE' center with the release of an electron [22], [85]:

$$\Delta n(\lambda) = \frac{1}{(2\pi)^2} \sum_i \int_{\lambda_2}^{\lambda_1} \frac{\left(\Delta \alpha_i(\lambda') \cdot \lambda^2\right)}{\left(\lambda^2 - \lambda'^2\right)} d\lambda' \qquad \text{(A-1)}$$

The refractive index has a real part and an imaginary part related to absorption, which in general neglected for its relatively low importance. According to equation (2-1), a source of photo-induced change in the absorption $\Delta \alpha_i$ at $\lambda_1 \le \lambda' \le \lambda_2$ will change the refractive index at wavelength λ . During the UV exposure of the glass, a change in the imaginary part of the refractive index in the UV will cause a change in the real part of the index in the infrared range. Various mechanisms for glass defects structure have been proposed over the years. These defects are usually called color centers and are caused by the fiber drawing process and ionizing radiation. These are a single photon absorption from defects between germanium and silica, Ge-Si, bonds created during the manufacturing process of the optical fiber. These bonds has an absorption band at 240 nm. Under the exposure of UV light, a bleaching of this absorption band occur and new defects like Ge (*n*), and GeE' (previously known as Ge (0)) are created and hence the evolution of new absorption bands, inducing a change in the refractive index. This type of photosensitivity is referred as "Type I" [22].

The following model describes the fiber which have been used in this dissertation. The proposed model is the stress relief. The fiber core is usually under tension due to the difference in the

thermal expansion of the core and the cladding. The tension reduces the refractive index through the stress-optic effect and the stress relief increases the refractive index as well. This stress between the core and the cladding relaxed by UV irradiation (photovicious annealing). This relief can be amplified by the presence of dopants such as boron or a high concentration of germanium in the core. It is associated with a negative index change of 10^{-3} in highly stressed fiber [22]. Also, the stress relief is dominated by a two-photon processes [66]. This type of photosensitivity is known as "Type IIA". The fiber which have been used in this dissertation are boron-doped fibers and hence the gratings are Type IIA gratings. A Bragg grating with index change of this type is more resistant to high temperatures than Type I grating [86].

As was mentioned previously, the photosensitivity of a glass can be enhanced by the addition of dopants like boron. On the other hand, hydrogenation can dramatically increase the photosensitivity of an optical fiber whose photosensitivity is low. Hydrogenation is achieved by diffusing hydrogen molecules into fiber cores at high pressures and temperatures. The fiber is placed in a high pressure reactor of hydrogen for a long period like two weeks until the fiber becomes saturated with hydrogen, the hydrogen relatively easily penetrating the glass structure. The fiber then becomes exceptionally sensitive over a wide band of UV radiation, the refractive index modulation can change up to the order of 0.01. OH^- absorbing species and UV bleachable germanium oxygen deficiency centers are formed by hydrogenation which are responsible for the enhanced photosensitivity [85]. This is known as photosensitivity of "type 1H" gratings. The drawback of the hydrogenation process is that the fiber becomes a slightly fragile [88]. The hydrogen also diffuses out of the optical fiber at room temperature, requiring storage the fiber at low temperatures at a refrigerator.

Several UV laser sources may be used for inducing refractive index changes and for fabricating Bragg gratings in optical fibers [22]. They can be categorized into low spatial coherence sources and spatially coherent sources. The excimer lasers as low spatial coherence sources such as ArF (193 nm) and KrF (248) nm are also commonly used in writing of Bragg gratings [89]. They are pulsed lasers of very high power. These lasers are commonly unstable and having a lower quality beam. The argon laser at 244 nm as high coherent source has several advantages [90]. This is a continuous wave (CW) source with high beam quality, a relatively expensive laser, a low energy efficiency and requires periodic replacement of components. Solid-state lasers such as Nd:YAG (266 nm), Nd:YLF (262 nm), and $Nd:VO_4$ (213 nm) are reliable lasers. These lasers offer

significant advantages such as being easy to use, very compact, having a relative high efficiency and high beam quality [69].

APPENDIX B : COUPLED MODE THEORY

The coupled mode theory (CMT) is used to describe the propagation of electromagnetic waves in a perturbed layered and non-magnetic medium with a permittivity distribution $\varepsilon(r) = \varepsilon_0 n^2(r)$. We describe the main aspects of this method and derive the equations of Bragg gratings based on this method [22]. The Maxwell's equations are given as was mentioned in chapter 1, section 1.1, by

$$\begin{aligned} &\nabla \cdot \vec{D} = 0, \quad \nabla \cdot \vec{B} = 0, \\ &\nabla \times \vec{H} = \frac{\partial \vec{D}}{\partial t}, \quad \nabla \times \vec{E} = -\frac{\partial \vec{B}}{\partial t}, \end{aligned} \tag{B-1}$$

using the relation, $\vec{D} = \varepsilon_0 \vec{E} + \vec{P}$, and taking the curl of last equation ,

$$\begin{aligned} &\nabla^2 \vec{E} = \mu_0 \varepsilon_0 \frac{\partial^2 \vec{E}}{\partial t^2} + \mu_0 \frac{\partial^2 \vec{P}}{\partial t^2}, \text{ with } \vec{P} = \vec{P}_{unpert} + \vec{P}_{pert} \\ &\Rightarrow \nabla^2 \vec{E} = \mu_0 \varepsilon \frac{\partial^2 \vec{E}}{\partial t^2} + \mu_0 \frac{\partial^2 \vec{P}_{pert}}{\partial t^2}; \end{aligned} \tag{B-2}$$

where $\vec{P}$ represents the polarization vector; $\vec{P}_{unpert}\left(\vec{r}, t\right)$ is the polarization vector in the absence of any perturbation and the $\vec{P}_{pert}$ is the induced polarization vector due to the perturbation. Ignoring the possibility of coupling to the continuum of radiation mode we expand the total field in the perturbed structure as a superposition of fields due to only the participating two guide modes of the unperturbed structure, we may write one of the net electric field component for co-propagating modes as,

$$E = \frac{1}{2}\left(A_1(z)\psi_1(x,y)e^{i(\omega t - \beta_1 z)} + A_2(z)\psi_2(x,y)e^{i(\omega t - \beta_2 z)} \right) + c.c. \tag{B-3}$$

for counter propagating modes the field component can be written as,

$$E = \frac{1}{2}\left(A_1(z)\psi_1(x,y)e^{i(\omega t-\beta_1 z)} + A_2(z)\psi_2(x,y)e^{i(\omega t+\beta_2 z)} \right) + c.c. \tag{B-4}$$

where, β_1 and β_2 are the propagation constants of the modes, and $A_1(z)$ and $A_2(z)$ are their corresponding amplitudes, ψ_1 and ψ_2 denote the orthogonal fields, respectively.

Substituting equation (B-3) in equation (B-2) and considering that in the presence of the weak perturbation, the variation in the mode amplitude is very slow which satisfies the condition,

$$\left|\frac{d^2A_k}{dz^2}\right| << \left|\beta_k \frac{dA_k}{dz}\right| \tag{B-5}$$

where, subscript *k* denotes mode number, we get,

$$-i\beta_1\frac{dA_1}{dz}\psi_1 e^{i(\omega t-\beta_1 z)} - i\beta_2\frac{dA_2}{dz}\psi_2 e^{i(\omega t-\beta_2 z)} + c.c. = \mu_0\frac{d^2P_{pert}}{dt^2} \tag{B-6}$$

where, P_{pert} represents the corresponding component of $\vec{P}_{pert}$. Multiplying both side of equation (B-6) with ψ_1^* and integrating over the entire cross section, and utilizing the orthonormality of modes (*i.e.* $\int_{-\infty}^{+\infty}\int_{-\infty}^{+\infty}\psi_n^*(x,y)\psi_m(x,y)\,dxdy = N_n\delta_{n,m}$) we get,

$$-2i\omega\mu_0\frac{dA_1}{dz}e^{i(\omega t-\beta_1 z)} + c.c. = \int_{-\infty}^{+\infty}\int_{-\infty}^{+\infty}\mu_0\frac{d^2P_{pert}}{dt^2}\psi_1^* dxdy \tag{B-7}$$

This equation describes the variation in the field amplitude of the first mode while it propagates through the periodic medium (alon the direction *z*). To solve this equation we need to get the value of P_{pert} first, which can be obtained as follows,

In a periodic medium, where the dielectric constant varies periodically along the direction of propagation (*z*), the total polarization can be defined in terms of the perturbed permittivity $\Delta\varepsilon(z)$ and the total field *E* through the relation,

$$P = (\varepsilon - \varepsilon_0)E + \Delta\varepsilon(z)E = (\varepsilon - \varepsilon_0)E + \varepsilon_0\Delta n^2 E = P_{unpert} + P_{pert} \tag{B-8}$$

As the perturbation is weak we can write,

$$P_{pert} = \varepsilon_0 2n\delta n(z) E \tag{B-9}$$

Now, taking the periodic refractive index modulation of the form,

$$\Delta n(z) = \overline{\Delta n}\left\{1 + \nu \sin\left(\frac{2\pi}{\Lambda} z\right)\right\} \tag{B-10}$$

where, $\overline{\Delta n}$ is the average refractive index change over a single period of the grating in the grating region, ν is the visibility of the fringes, and Λ is the grating period. The amplitude of the ac part of the refractive index variation Δn is thus, $\Delta n = \overline{\Delta n}\,\nu$.

Using equation (B-3), equation (B-9) and equation (B-10) in equation (B-7), we get the coupled equation of the form

$$\frac{dA_1}{dz} = -i\kappa_{11} A_1 - i\kappa_{ac}^{*} A_2 e^{i\Delta\beta z} \tag{B-11}$$

where, $\Delta\beta$ is the phase mismatch given by:

$$\Delta\beta = \beta_1 - \beta_2 + \frac{2\pi}{\Lambda} \tag{B-12}$$

Similarly for the second mode we get:

$$\frac{dA_2}{dz} = -i\kappa_{22} A_2 - i\kappa_{ac}^{*} A_1 e^{-i\Delta\beta z} \tag{B-13}$$

with κ_{dc} and κ_{ac} being the self-coupling (dc coupling) and mutual coupling (ac coupling) coefficient defined as,

$$\kappa_{dc} = n\omega\varepsilon_0 \int_{-\infty}^{+\infty}\int_{-\infty}^{+\infty} \overline{\Delta n}\,\psi_k \psi_k^{*} dx dy \tag{B-14}$$

and,

$$\kappa_{ac} = n\omega\varepsilon_0 \int_{-\infty}^{+\infty}\int_{-\infty}^{+\infty} \frac{\Delta n}{2}\,\psi_k \psi_l^{*} dx dy \tag{B-15}$$

Equations (B-11) and (B-13) are coupled equation s containing the field amplitudes of both modes. In order to have an identical relation for the evolution of both modes we use a simple transformation by substituting,

$$A_1 = \mathrm{R}\ exp\left(-i\frac{\kappa_{12} + \kappa_{21} - \Delta\beta}{2} z \right) \tag{B-16}$$

and

$$A_2 = \mathrm{S}\ exp\left(-i\frac{\kappa_{12} + \kappa_{21} + \Delta\beta}{2} z \right) \tag{B-17}$$

in both equations (A-11) and (A-13). After rearranging the terms, the coupled equations are reduced to,

$$\begin{aligned} \frac{dR}{dz} &= -i\kappa S - i\delta R \\ \frac{dS}{dz} &= -i\kappa R + i\delta S \end{aligned} \tag{B-18}$$

where, $\kappa = \kappa_{ac}$ and $\delta = \frac{1}{2}[\kappa_{11} - \kappa_{22} + \Delta\beta]$. Using equation (B-18) itself on the right hand side, we get,

$$\begin{aligned} \frac{d^2R}{dz^2} &= -\left(\kappa^2 + \delta^2\right) R \\ \frac{d^2S}{dz^2} &= -\left(\kappa^2 + \delta^2\right) S \end{aligned} \tag{B-19}$$

Finally, imposing the boundary condition that all the power is initially launched to the first mode,

$$\begin{aligned} R\left(z = 0, \delta\right) &= 1 \\ S\left(z = 0, \delta\right) &= 0 \end{aligned} \tag{B-20}$$

the solutions of equation (B-20) are obtained,

$$R\left(z=L,\delta\right)=\cos\left(\alpha L\right)-i\frac{\delta}{\alpha}\sin\left(\alpha L\right)$$
$$S\left(z=L,\delta\right)=-i\frac{\kappa}{\alpha}\sin\left(\alpha L\right) \tag{B-21}$$

where, $\alpha=\sqrt{\kappa^2+\delta^2}$. Thus the transmitted power through mode 1 and 2 are,

$$\left|R\right|^2=\cos^2\left(\alpha L\right)+\frac{\delta^2}{\alpha^2}\sin^2\left(\alpha L\right)$$
$$\left|S\right|^2=\frac{\kappa^2}{\alpha^2}\sin^2\left(\alpha L\right) \tag{B-22}$$

Similarly, for counter propagating modes, the reflection coefficient can be given by:

$$\rho=\frac{S\left(z=0\right)}{R\left(z=0\right)}=\frac{-\kappa\sinh\left(\alpha L\right)}{\delta\sinh\left(\alpha L\right)-i\alpha\cosh\left(\alpha L\right)} \tag{B-23}$$

with, $\delta=\kappa_{11}+\frac{\Delta\beta}{2}$ and $\alpha=\sqrt{\kappa_{ac}^2-\delta^2}$. The reflectivity is therefore:

$$\mathrm{R}\quad=\left|\rho\right|^2=\frac{\left|\kappa\right|^2\sinh^2\left(\alpha L\right)}{\left|\kappa\right|^2\cosh\left(\alpha L\right)-\delta^2} \tag{B-24}$$

Hence, the transmitted power is T = 1-R.

APPENDIX C: LIST OF PUBLICATION RELATED TO THE DISSERTATION

Journals

1. M. D. Baiad, M. Gagne, and R. Kashyap, " Silicon-coated multi-channel surface Plasmon resonance sensors using tilted fiber bragg gratings," submitted to *Opt. Letters,* Oct. 2014.

2. M. D. Baiad, and R. Kashyap, " Concatenation of surface Plasmon resonance sensors in a single optical fiber using tilted fiber Bragg gratings," accepted for publication in *Opt. Letters*, Oct. 2014.

3. E. Filho, M. D. Baiad, M. Gagné, and R. Kashyap, "Fiber Bragg gratings characterization and modeling for low-temperature measurement," submitted to *Opt. Express,* Sept. 2014.

4. G. Lin, M. D. Baiad, M. Gagne, W. Liu, and R. Kashyap, "Harnessing the fiber fuse for sensing applications," Opt. Express 22, 8962-8969 (2014).

5. M. D. Baiad, M. Gagné, E. De Montigny, W.-J. Madore, N. Godbout, C. Boudoux, and R. Kashyap, "SPR sensor interrogation with a double-clad fiber coupler and cladding modes excited by tilted fiber Bragg grating," *Opt. Letters*, vol. 38, no. 22, November. 2013. (SPOTLIGHT ON OPTICS)

6. M. D. Baiad, M. Gagné, S. Lemire-Renaud, E. De Montigny, W.-J. Madore, N. Godbout, C. Boudoux, and R. Kashyap, "Capturing reflected cladding modes from a fiber Bragg grating with a double-clad fiber coupler," *Opt. Express*, vol. 21, no. 6, pp. 6873–6879, Mar. 2013.

Conferences

1. TUTORIAL: M. D. Baiad, M. Gagné, and R. Kashyap, "Distributed tilted fiber Bragg grating and surface plasmon Polariton **sensors**," submitted to LAOP, Cancun, Mexico, November 2014.

2. PLENARY: M. D. Baiad, M. Gagné, and R. Kashyap, «Multiplexed fibre optic surface Plasmon sensors," submitted to CIOFF, Havana, Cuba, Oct. 2014.

3. G.-R. Lin, M. D. Baiad, M. Gagne, W.-F. Liu, and R. Kashyap, "A novel refractive index sensor based on an induced micro-structure fiber," *Proc. SPIE*, vol. 9157. pp. 915773–915774, 2014. (WON THE BEST STUDENT POSTER AWARD)

4. M. D. Baiad, D. Das, V. Lambin-Iezzi and R. Kashyap, "Multi-channel surface Plasmon sensor using a unique H-cross-section optical fiber," Proc. SPIE 8938, Photonics West 2014. (Abstract accepted).

5. M. D. Baiad, M. Gagné, E. de Montigny, W.-J. Madore, N. Godbout, C. Boudoux, and R. Kashyap, "Optical fibre Bragg grating cladding mode sensors," *Proc. SPIE*, vol. 8794. p. 87941H–87941H–4, 2013.

6. M. D. Baiad, M. Gagne, E. De Montigny, W. J. Madore, N. Godbout, C. Boudoux, and R. Kashyap, "High-efficiency, double-clad fiber coupler, cladding mode sensor using a tilted fiber Bragg grating," OptoElectronics and Communications Conference held jointly with 2013 International Conference on Photonics in Switching (OECC/PS), 2013 18th. pp. 1–2, 2013.

7. M. D. Baiad, S. M. Tripathi, A. Kumar, and R. Kashyap, "Pure surface plasmon-polariton optical sensor using an H-cross-section fiber and Bragg gratings," in *Proc. SPIE 8412, Photonics North*, 2012, p. 84120J. (WON THE BEST STUDENT POSTER AWARD)

8. M. D. Baiad, S. M. Tripathi, A. Kumar, G. Nenova, and R. Kashyap, "Integrated optical bio-sensor based on pure surface plasmon-polariton excited by a waveguide grating," in *Fibre and Optical Passive Components (WFOPC), 2011 7th Workshop on*, 2011, pp. 1–5

List of Related Scholarships and Awards

- MITACS ELEVATE Industrial Postdoctoral Fellowship
- NSERC-CREATE Training Program in Integrated Sensor System Fellowship Award
- NSERC-CREATE Training Program in Integrated Sensor System Travel Funding Award

- Best Student Poster Award, 23rd International Conference on Optical Fiber Sensors OFS23, June 2-6 2014, Santander, Spain
- Best Student Poster Award, Photonics North International Conference, June 6-8 2012, Montreal, Canada